2014

Tissue Engineering Scaffold Fabrication and Processing Techniques to Improve Cellular Infiltration

Casey Grey
Virginia Commonwealth University

TISSUE ENGINEERING SCAFFOLD FABRICATION AND PROCESSING TECHNIQUES TO IMPROVE CELLULAR INFILTRATION

A dissertation submitted in partial fulfillment of the requirements for the degree of Doctor of Philosophy in Biomedical Engineering at Virginia Commonwealth University

By

CASEY PAUL GREY

B.S. Virginia Military Institute, 2007

M.S. Virginia Commonwealth University, 2012

Director: DAVID SIMPSON, PH.D.

Associate Professor, Department of Anatomy and Neurobiology

Virginia Commonwealth University

Richmond, Virginia

December, 2014

Acknowledgements

Interestingly enough, this is the very last section I'm writing for my dissertation and, without a doubt, it's giving me the most trouble. The help that I've received getting to this point is nothing short of incredible and I apologize if I don't adequately convey my appreciation. My girlfriend, Kelly, is the reason I went to, succeeded in, and finished graduate school. My friends and family supported me financially, emotionally, and even academically (my dad is recognized in one of my publications and my friend Kendall is the reason I collaborated with Dr. Simon). Great friends who were always good for a "Tubular Tuesday" beer at Joes, kickball, or maybe even a game of risk (though not necessarily finishing it) helped me get away from school and (mostly) keep my sanity. Finally, my PI, Dr. David Simpson. Dr. Simpson is, as those who know him will attest, an unconventional whirlwind of enthusiasm, and I'm incredibly grateful for that. His energy, creativity, and spirit are amazing and I truly can't thank him enough for his guidance throughout my graduate career.

All in all, I lucked out, plain and simple. To all who helped in this, thank you so, so much.

TABLE OF CONTENTS

Abstract

TISSUE ENGINEERING SCAFFOLD FABRICATION AND PROCESSING TECHNIQUES TO IMPROVE ELECTROSPINNING

By: Casey Paul Grey, M.S.

A dissertation submitted in partial fulfillment of the requirements for the degree of Doctor of Philosophy in Biomedical Engineering at Virginia Commonwealth University.

Virginia Commonwealth University, 2014.

Major Director. David G. Simpson, PhD, Department of Anatomy/Neurobiology

Electrospinning is a technique used to generate scaffolds composed of nano- to micron-sized fibers for use in tissue engineering. This technology possesses several key weaknesses that prevent it from adoption into the clinical treatment regime. One major weakness is the lack of porosity exhibited in most electrospun scaffolds, preventing cellular infiltration and thus hosts tissue integration. Another weakness seen in the field is the inability to physically cut electrospun scaffolds in the frontal plane for subsequent microscopic analysis (current electrospun scaffold analysis is limited to sectioning in the cross-sectional plane). Given this it

becomes extremely difficult to associate spatial scaffold dynamics with a specific cellular response. In an effort to address these issues the research presented here will discuss modifications to electrospinning technology, cryosectioning technology, and our understanding of cellular infiltration mechanisms into electrospun scaffolds. Of note, the hypothesis of a potentially significant passive phase of cellular infiltration will be discussed as well as modifications to cell culture protocols aimed at establishing multiple passive infiltration phases during prolonged culture to encourage deep cellular infiltration.

CHAPTER 1

Introduction: A Brief Review of Common Tissue Engineering Scaffold Manufacturing Techniques

Preface: In this chapter I briefly describe the role of tissue engineering in medicine, that is, to replace or direct the regeneration of diseased, damaged, or otherwise non-functional tissues. Additionally, I describe different fabrication methods used to produce scaffolds that are designed to support directed regeneration.

A Brief Review of Common Tissue Engineering Scaffold Manufacturing Techniques

Casey P. Grey[1]

[1]Department of Biomedical Engineering

1.1 INTRODUCTION

Advancements in regenerative medicine are pioneered in tissue engineering research labs throughout the world. These efforts are both inspired and demanded by the needs of people suffering from conditions that can benefit from regenerative therapy, which is estimated to be as high as 1 in 3 in the United States.[1] Tissue engineering is a field dedicated to understanding biological systems with the translational goal of either replacing entire systems when they fail or guiding them back toward a path of normal functionality when they stray.

The field of tissue engineering specifically focuses on developing tissue analogs that support a directed cellular response with the goal of eventually regenerating lost or damaged tissues and organs.[2-4] This effort typically involves constructing an "empty shell" scaffold consisting of a natural, synthetic, or a combination of a natural and synthetic materials fabricated into a scaffold that mimics the target extracellular matrix (ECM). Ideally, when the correct cells are seeded onto the scaffold the scaffold itself directs cellular migration, proliferation, and differentiation such that it transitions from being an acellular construct to a populated, yet non-functional construct (where the cells have occupied the scaffold but have not yet formed a tissue-like material) to finally a "living scaffold," or functional tissue analog, that can perform an intended physiological function (e.g. blood vessel). The ultimate end-goal of regenerative medicine, to restore normal tissue function, is typically visualized through implantation of a biodegradable scaffold that is gradually replaced with native components as healthy tissue occupies the implantation site. In this way the scaffold serves its intended function, i.e. it provides a platform to transplant donor cells and/or supports the infiltration of targeted cells and directs the

maturation of the construct into functional tissue, after which the scaffold degrades away so that normal physiological function is not impeded by non-physiological tissue components (e.g. non-degradable polymer).[5-11]

1.2 FABRICATION OF TISSUE ENGINEERING SCAFFOLDS

Tissue engineering strategies typically produce scaffolds that are inadequate for clinical use because they fall into either one of two categories; they either possess the mechanical strength required to withstand the physiological loads seen in vivo but lack the appropriate microenvironment to induce the desired cellular response (e.g. scaffold infiltration and occupation) or they possess a microenvironment that induces a good cellular response but lacks the mechanical strength to survive in vivo implantation. The common goal in tissue engineering labs, ours included, is to explore advancements in scaffold manufacturing techniques in order to find the middle ground where a scaffold possesses both the necessary strength to withstand some physiological loading while maintaining the ability to induce a targeted cellular response. An excellent overview of an "ideal" tissue engineering scaffold is provided by Chan and Leong.[7] They state that the ideal tissue engineering scaffold should possess the requisite architecture suited to encourage full infiltration and occupation of target tissues, promoting both the ingrowth of tissue and the necessary vascular support networks. Going with this is the idea that the scaffold must be biocompatible and cytocompatible, that is, cells must readily grow on and attach to the scaffold and stay a physiologically healthy state (e.g. the cells don't die, become cancerous, etc). Additionally scaffolds should contain no cytotoxic or immunogenic byproducts that could impair the progress of tissue recovery and function, rather the scaffold should be positively bioactive through the incorporation of factors (e.g. growth factors such as fibroblast growth factor, or FGF) that encourage targeted tissue-scaffold integration. Finally, the scaffold should possess very similar intrinsic structural and mechanical properties as the target tissue in order to provide some immediate support and to limit the mechanical stresses applied to

infiltrating cells after implantation as this could propagate an undesirable inflammatory wound healing response.[7]

Autologous Grafts

Autologous grafts are tissue grafts that come directly from the patient.[12] These have several advantages over exogenously fabricated tissue engineering scaffolds including, and arguably most importantly, the compositional elements and structural characteristics of natural extracellular matrix paired with a low potential for immunogenicity.[3,9,13-15] In practice autologous grafts are often considered the "gold standard" graft for tissue repair.[16-19] While not all autologous grafts are taken from identical tissues (e.g. nerve tissue to replace a nerve defect) [20,21], as long as the inherent characteristics of the extracellular matrix are similar or otherwise adaptable the autologous graft appears, in many cases, to support and direct a good regenerative response. For example, Ezzell reported the use of pig intestinal grafts for use in vascular, ligament, and bladder applications.[22] Pape reported a 90% success rate using autologous bone taken from the iliac crest of patients to bridge tibial gaps.[11] These experiments reveal the enticing potential of tissue plasticity, a concept that fundamentally underlies the tissue engineering paradigm.

With all of the benefits of autologous grafts one may wonder why the "gold standard" treatment isn't the obvious initial treatment for tissue regeneration. One answer lies in the main weakness of autologous grafts; the simple fact that the donor is also the recipient and has a limited supply of applicable tissue. Isolating tissue for transplantation results in donor site morbidity (e.g. the

donor tissue is no longer serving its original function) and the recovery trauma from tissue harvesting surgery can outweigh the benefits of the graft.[9,23]

Allogenic grafts circumvent the donor site morbidity issue (at least from the recipient patient's perspective) by utilizing donor tissue from another person.[24] This tissue can be cadaveric in nature [25] or it can originate from a donor willing to sacrifice tissue (e.g. kidney donor). While scaffold processing protocols for allogenic acellular grafts are rigorous, the potential for an immunological response and the attendant risk of inflammation and rejection is very real, conditions which clearly represent potentially catastrophic events that can lead to the loss of the graft or worse. Chemical processing and detergent washes can effectively remove resident cells from an allogenic scaffold, minimizing the immunogenic response, however, this processing also tends to remove many of the growth factors that are bound to matrix constituents.[26] These soluble factors can provide critical support for tissue development and are typically retained when an autologous graft is employed for regenerative therapy. Perhaps the principle advantage of the decellularized allogenic graft is the lack of donor site morbidity in a scaffold that is a mimic or essentially a replica of the extracellular matrix of the target tissue.[4,25] Despite processing there also is always a risk of disease transmission when an allogenic graft is used to reconstruct tissue.[27]

Hydrogels

A hydrogel has two component characteristics: the "gel" part of hydrogel refers to the polymer structure which consists of physically or chemically crosslinked hydrophilic polymers while the

"hydro" part of hydrogel refers to capacity of these materials to absorb and hold water.[28] When placed in an aqueous environment the strongly hydrophilic nature of polymer backbone structure causes the gel to swell as it absorbs and holds water. The extent of absorption can raise the water content of a hydrogel from 20% to up to 99% (as determined by weight).[29] Because the water content is so high hydrogels are typically very biocompatible.[30] When implanted a hydrogel expands due to water influx from the physiological environment. Soluble bioactive components, often incorporated by design (e.g. hydrogels as drug delivery vehicles), are released as a consequence of the hydration process by cell mediated events, enzymatic events or, in some cases, in the presence of an external signal such as an electrical current applied to conductive hydrogels.[31] These properties make hydrogels prime candidates in drug delivery applications.[32,33] Additionally, the incorporation of bioactive factors into the hydrogel structure allows for the extended release of targeted pharmaceuticals.

The materials that make up the polymer network of a hydrogel can be natural (e.g. collagen), synthetic (e.g. poly DL-lactic acid-co-glycolic acid, called PLGA), or combinations of natural and synthetic polymers.[34] To form a coherent structure the separate polymer fibers are cross-linked together either physically or chemically.[30] Physical crosslinking can involve chain entanglement, hydrogen bonding, ionic interactions, and strong van der Waals interactions and is typically characterized as being a weaker and reversible bond. Chemical crosslinking involves covalently bonding the polymers together in a strong and irreversible reaction.[30] While physical crosslinking processes yield structurally much weaker hydrogels, they remain the most utilized approach in the fabrication of hydrogels because of the excellent biocompatibility in the

resulting structure.[30] Physical crosslinking does not utilize chemical crosslinking agents which may damage cells, alter the activity and availability of growth factors, and may cause inflammation. As a result physical crosslinking methods are perceived to fare better in applications with sensitive physiological components. An example of physical crosslinking is introducing alginate droplets into a calcium solution. The calcium solution induces the rapid ionic gelation of the alginate droplets which can be used to encapsulate growth factors and/or cells.[35] Despite their excellent biocompatibility, the weak bonds formed through physical crosslinking are often ill-suited for tissue engineering applications that involve physiological loading or significant scaffold handling. In these cases the better approach is hydrogel formation through chemical crosslinking. In an effort to make the ideal hydrogel that is both biocompatible and structurally sound, new research efforts have involved incorporating both physical and chemical crosslinking in a balanced and complementary approach. This process typically involves the initial extrusion of a hydrogel precursor that possesses adequate physical crosslinking characteristics to maintain its extruded shape followed by a secondary treatment that initiates the permanent covalent bonds characteristic of chemical crosslinking. This dual process has the potential to produce strong and biocompatible hydrogels as long as the physical crosslinking reaction is strong enough to maintain the initial shape and the application of chemical crosslinking agents can be metered to levels that are in the biocompatible range. Research and development of hydrogels remains an active avenue of investigation.[35]

Traditionally the application of hydrogels in tissue engineering has been in cases where high mechanical strength is not a priority and where there are no strict geometrical requirements on the implanted scaffold. Specifically, hydrogels have excelled in drug delivery

applications.[32,33] However, creating a hydrogel with the mechanical strength to withstand physiological load-bearing applications is a major challenge. Additionally, due to their propensity to swell in an aqueous environment and due to natural physiological environmental variations, designing a hydrogel to fit specific geometrical requirements is likewise very challenging. While they tend to lack in mechanical strength, hydrogels possess excellent porosity, biocompatibility, and potentially useful expansion properties (e.g. the ability to expand once implanted or after the application of a specific stimulus such as heat or an electrical signal) which is why they remain such an active topic of tissue engineering research.

3D Printing

A weakness of nearly all tissue engineering scaffold manufacturing techniques is that they lack fine control over the scaffold architecture.[36] What this means is that, while most conventional scaffold fabrication techniques do offer control over some general structural characteristics such as porosity, mean fiber size, etc, they do not placement of specific structural elements. Three-dimensional (3D) printing techniques, however, involve creating a scaffold through the layer-by-layer deposition of a curable polymer.[37] This technique not only allows, but requires that the location of each structural component of the scaffold be defined. This is most often accomplished through the generation of 3D computer models that represent the desired scaffold. Once the model is generated it is automatically broken up into z-stacks by the software and sent to the 3D printer (Figure 1.1). For example, if the curing height of the extruded polymer is 1mm (a gel-like polymer solution is extruded by the printing orifice, this refers to the height of the extruded polymer once it cures), a 1cm tall scaffold would be digitally sliced

through the z-axis into 10 separate 1mm-tall sections. Each z-stack is sent individually to the 3D printer which "draws" the stack by extruding the polymer onto a substrate. After the completion of each successive z-stack, the printer orifice translates a specific distance in the z-direction (in this example the printer orifice would translate 1 mm) and begin extruding the next z-stack segment. At the end of the process the 3D printer will have extruded 10 individual sections that, if the polymer curing properties and the printing timing are adequately controlled, will adhere together to form a coherent three-dimensional scaffold.[37]

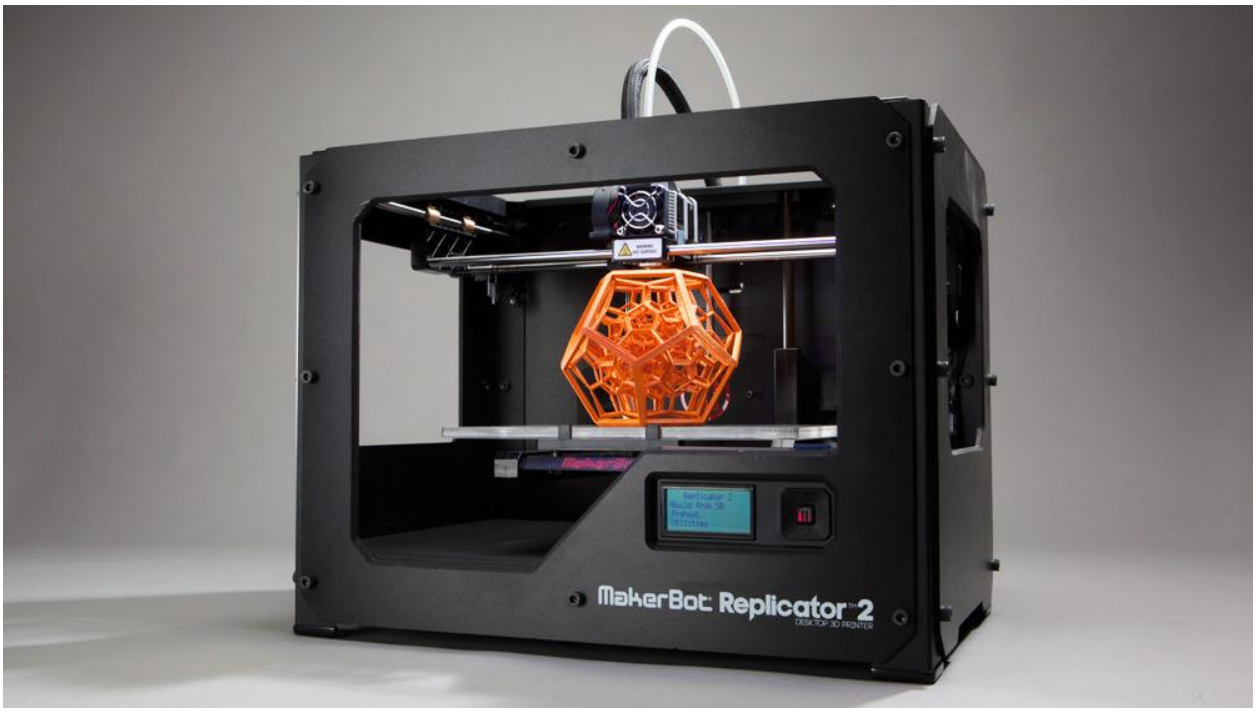

Figure 1.1. A commercially available 3D printer (http://3dprinterplans.info/tag/makerbot-replicator-2/)

3D printing technology has been used in bone regeneration [38], culturing cardiac cells [39,40], and for the creation of vascular and nerve grafts.[41] In addition to fabricating scaffolds, 3-D

printing technology also has the potential to create "copies" of tissues from medical images of patients (e.g. from MRI images).[42] This gives clinicians a useful tool in assessing treatment strategies such as a particular surgical approach or possible procedural risks on a patient by patient basis.[43] The main drawback of this technology is its inability to produce structural elements comparable in size to the structural elements of natural extracellular matrix. Scaffolds printed with the 3D printing technology available prior to 2010 were limited to structural components that span a few hundred microns, far greater in size than native tissue matrix components (Figure 1.2).[42,44] Currently the method can be used to produce far smaller structural elements, however, consistently printing a sub-micron sized component in a defined pattern has not been consistently achieved for many compositional elements.[44,45]

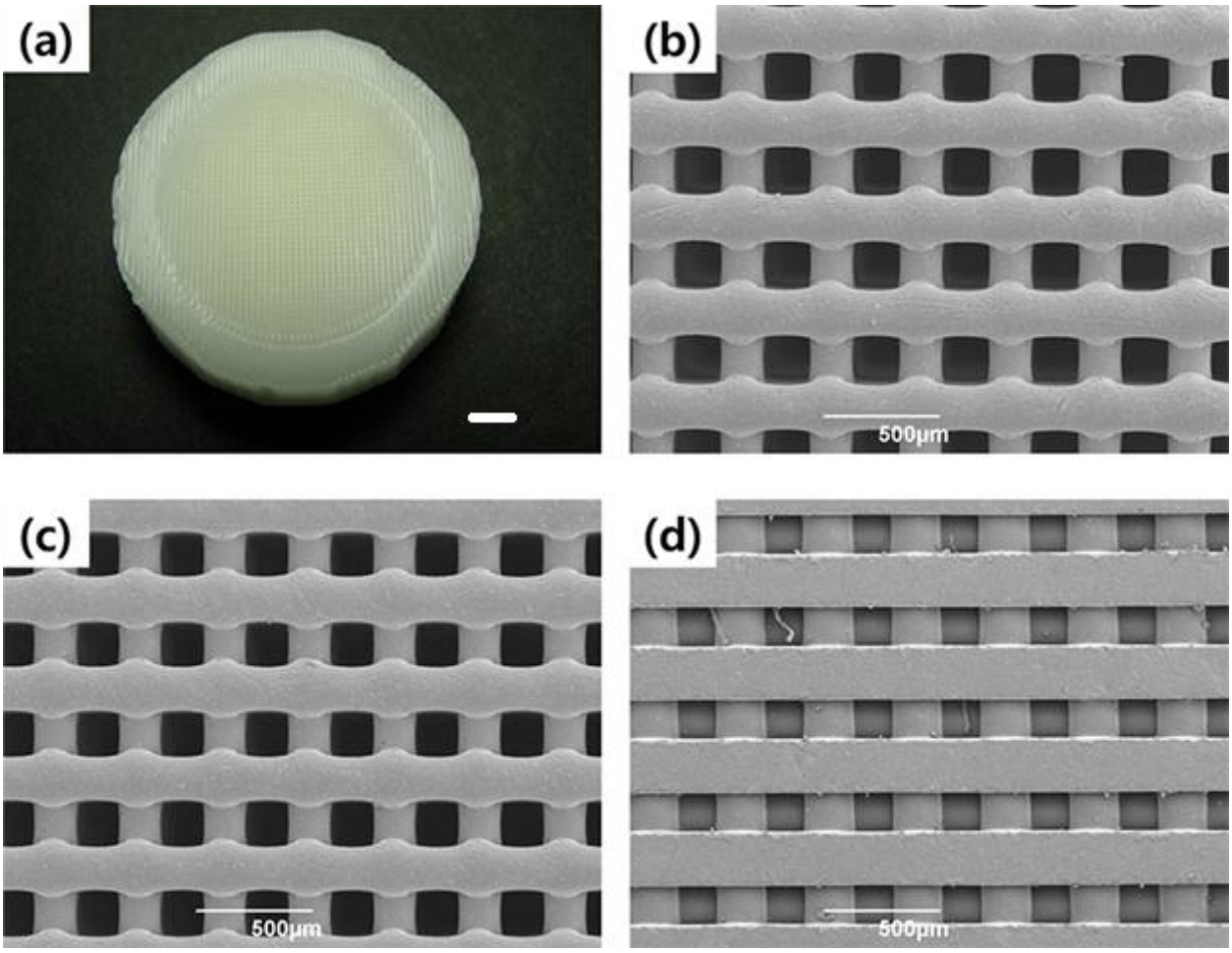

Figure 1.2. *Jung et. al. show examples of 3D printing scaffolds.* A) whole scaffold, scale = 2mm, B-D) SEM images of different scaffold fabrications [46]. Note the precise control over scaffold architecture exhibited in 3D scaffolds.

As with all new technology another major limitation of 3D printing is the cost feasibility of the technique. Applying Moore's Law to 3D printing predicts that these cost issues will be addressed with time (3D printing is a computer based technique after all).[47] Once the technical limitations are addressed and 3D printing technology evolves sufficiently to produce sizeable constructs composed of precisely arranged micron sized elements this technique may revolutionize the design and fabrication of tissue engineering scaffolds.[45]

Electrospun Scaffolds

Electrospinning is a technique used to produce scaffolds composed of nano-to-micron diameter sized fibers, similar in size to fibers found in the extracellular matrix of native tissues.[5,9,14,48-50] These fibers of physiologically relevant size can be formed from a broad spectrum of materials, from natural (e.g. collagen, elastin) to synthetic (e.g. PCL, PLLA, PEG) with the former possessing more natural biomarkers for cell surface attachment and the latter possessing more easily optimized mechanical properties. [51] The process is in many ways is more versatile than the techniques classically used to make hydrogels; resulting in the ability to vary the mechanical and biological properties of a scaffold in an unprecedented manner over a wide range of characteristics.

General Electrospinning Setup

In the typical electrospinning setup an electrospinning solution is contained in a syringe and is charged by connecting a power source to a blunted needle placed at the outlet of the syringe. The charged solution is then extruded via syringe driver at a predetermined rate toward the oppositely charged (or grounded) target.

At low source voltages (<15kV) the electrospinning solution simply drips out of the syringe and onto the ground. Increasing the source voltage initiates the electrohydrodynamic phenomenon known as a Taylor cone where the balance between the electrostatic repulsion of the solution and the hydrodynamic attraction (predominantly surface tension) becomes slightly skewed towards electrostatic repulsion and a thin fluid jet flows from a stable "cone." At this point the

electrospinning jet is said to be "initiated" and fibers can be collected at the target to begin the production of a scaffold.

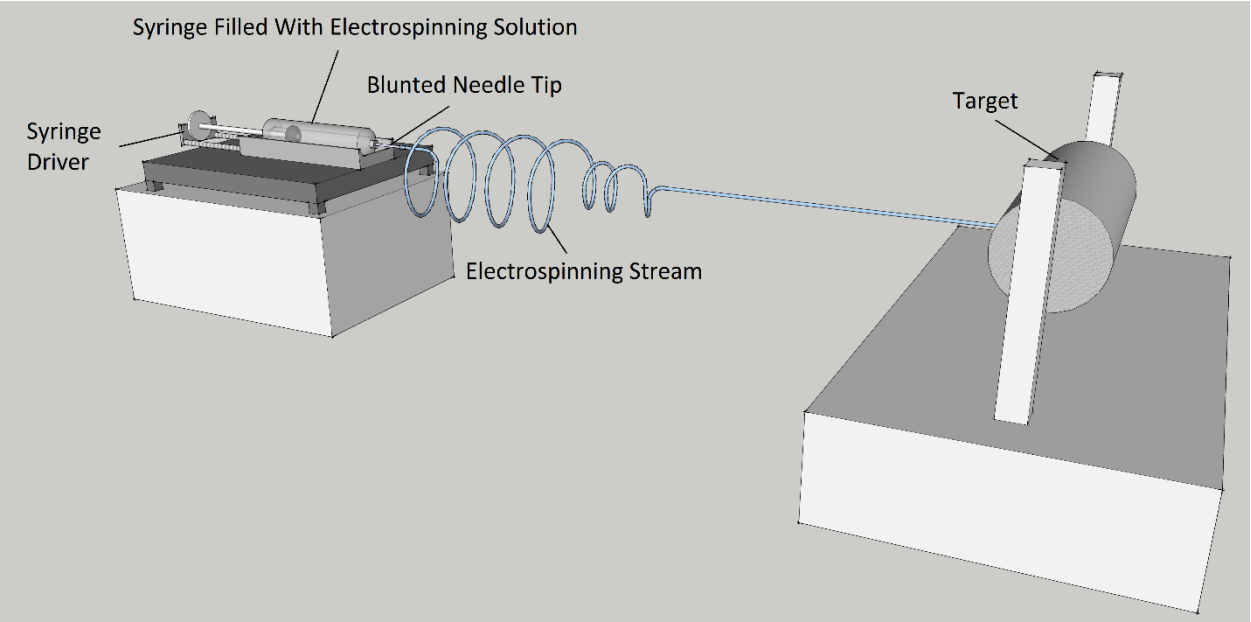

Figure 1.3. *A typical electrospinning setup. The syringe is filled with a polymer solution that is then charged as it exits the needle tip. The balance between solution surface tension and electrostatic repulsion becomes skewed such that a Taylor cone forms, from which a jet of polymer streams from the needle tip towards the target. During flight the polymer stream dries into a fiber and is then deposited on the target.*

Bending Instabilities and Fiber Drying

Once the electrospinning jet has been initiated a charged stream of fluid is sent towards the target. The extreme charge characteristics of the stream as a result of like charge repulsion induce bending instabilities that lead to the characteristic "whipping" action seen in electrospinning (see FIGURE 1 where the electrospinning stream appears to form a wide helix).[52,53] The whipping phenomenon has been modeled as a system of connected

viscoelastic dumbbells (beads on either end connected by a spring) where each bead represents a point charge and is connected to adjacent beads via a similar elastic connection, preventing their separation.[54] The static charge profile of each bead reacting with the static profile of its neighbor (like-charges repelling each other) propagates the lateral motion of the stream. This turns out to be advantageous; as the fluid stream evaporates the charge repulsion concentrates and causes the jet to whip back and forth resulting in the transition of the completely liquid stream into a much thinner solid fiber. The distance required for this transition is important – an insufficient electrospinning gap between the source and the target results in a "wet" deposition due to the incomplete evaporation of the solvent. The presence of the solvent at the target can result in mild solvent welding (if the gap is just slightly insufficient) or, in extreme cases (target right next to source) the resulting scaffold can be melted into a nearly solid mass. While overestimating the electrospinning gap theoretically solves all solvent welding problems, too large of a gap tends to result in poor fiber targeting and inadequate deposition (collection or recovery) rates. It's worth mentioning that, without the whipping motion, the electrospinning gap would have to be much wider to accommodate adequate solvent evaporation and, since targeting becomes more challenging over larger gaps, the entire process would be much more difficult to perform.

The electrospinning target

The characteristics of the electrospinning target play an important role in the design and fabrication of a scaffold for a particular application. While the source solutions determine the nature of fiber composition and size, the shape of the affects gross scaffold structure as well as

fiber alignment, orientation, and density (which determines porosity). Gross scaffold architectural characteristics play a role in the regenerative process. For example scaffolds directed at promoting dermal regeneration are usually composed of random elements, scaffolds for the fabrication of blood vessels are hollow cylinders fabricated with radically aligned fibers and scaffolds for nerve engineering are composed of solid cylinders containing linear arrays of fibers oriented along the long axis of the construct.[55,56]

The simplest target architecture to deposit fibers on is a flat plate. Because the plate is stationary and the charge density on it is, for the most part, homogenous (there are some minor charge concentrations at any sharp bend in the plate, e.g. the sides, which can simply be cut out from the end product) the resulting scaffold consists of evenly-dispersed fibers with random orientation. As fibers begin to accumulate on the surface, that portion of the surface becomes partially insulated and subsequent fibers are "directed" (by the ground charge on the plate) to accumulate in adjacent areas. In the same manner fibers may be deposited onto a rotating mandrel with very slow rotational velocities, producing a tubular scaffold consisting of the randomly oriented fibers (as long as the rotational velocity is slow it does not noticeably affect fiber alignment).[9] The whipping of the fiber jet is sufficiently chaotic to result in fibers becoming deposited in a more or less random fashion (even at very low rotation velocities some degree of anisotropy is often present in these scaffolds, it is negligible and varies with fiber diameter, this anisotropy is usually only evident under material testing conditions). For other applications it may be necessary to produce a sheet of fibers aligned predominantly in one direct (e.g. for a tendon graft). In order to accommodate this structural requirement the electrospinning target must be modified to produce aligned fibers. Achieving aligned fibers in an electrospun scaffold is

possible through the use of high rotational velocities on the target mandrel. In this setup, the electrospun fibers are oriented in the direction of mandrel rotation. A similar architecture can be achieved by confining the whipping motion of the charged electrospinning jet along a narrowly defined region with an electric field, however, the use of a rotating mandrel is typically easier to employee. Another electrospinning setup that achieves aligned fibrous scaffolds was pioneered by Jha, et. al. where two individual point targets are used to collect fibers between them.[23] In this way a solid cylinder of highly aligned fibers is formed. Table 1.1 details some examples of how various architectural features of the target can be exploited to modulate the gross structural properties of an electrospun scaffold.

Electrospun Scaffold Characteristics	**Example Electrospinning Target Architectures**
Randomly Oriented Mat	Flat Plate Rotating Mandrel (Low Rotational Velocity)
Aligned Mat	Rotating Mandrel (High Rotational Velocity)
Aligned Cylinder	Dual Pole Targets (2-5 cm spacing)*
Heterogeneous Fiber Porosity	Perforated Mandrel (Low Rotational Velocity)

Table 1.1. Desired electrospun scaffold characteristics and example electrospinning target architectures required to achieve the specified properties. *Fibers collect between the poles resulting in highly aligned fiber arrays for nerve reconstruction.

The versatility of electrospinning to support the use of a wide range of polymer and natural solutions, source and target designs, and fiber-modifying perturbations allows for the creation of extremely diverse products. This versatility enables researchers to tailor their electrospinning parameters to produce scaffolds meeting specific design criteria. Practical examples of this include two-pole electrospun scaffolds to induce peripheral nerve regeneration in a rodent model,[23] air impedance electrospinning to induce localized cellular infiltration,[5] and the incorporation of natural polymers into scaffolds to better mimic the properties of natural ECM.[48,57]

1.3 SUMMARY

Regenerative medicine encompasses all tissues simply because all tissues can be injured and thus require adequate regeneration in order to restore tissue function. Several specific tissues, such as skin, bone, and blood vessel are some of the most commonly researched targets for tissue regeneration. Tissues, in general, are targeted for several reasons: 1) clinically it is found that the tissue is often compromised and exhibits poor natural regeneration, 2) the tissue is easy to regenerate and thus the study of this particular tissue's regenerative characteristics might provide insight into how more complex tissues regenerate, 3) development of a scaffold manufacturing technique provides a means to reasonably approximate the healthy tissue structure (often the ECM), and importantly 4) there is adequate commercial demand for more effective scaffolds resulting in investment funds for specific research. Whether it stems from scientific curiosity, humanitarian goals, the desire for peer recognition, or even the desire for monetary gain, the fields of tissue engineering and regenerative medicine have continued to expand. There will be an estimated $853 million of NIH funding allotted to regenerative medicine research for both 2014 and 2015.[58] The future of medicine is an interdisciplinary and collaborative field that focuses equally on providing top-notch treatment as well as researching new and innovative approaches to medical problems.

CHAPTER 2

Cellular Responses in Wound Healing and Tissue Regeneration

Preface: The intricacies of the myriad physiological events that take place during wound healing are certainly appreciated in their complexity but still poorly understood. While the major theme of this dissertation deals with cellular interactions with man-made extracellular matrix analogues (a small subset of wound healing), having some understanding of both upstream and downstream events in the wound healing process helps to guide specialized research in the field. With that in mind, this chapter focuses on reviewing the general principles of wound healing so that a working knowledge can be obtained.

Cellular Responses in Wound Healing and Tissue Regeneration

Casey P. Grey[1] and David G. Simpson[2]

[1]Department of Biomedical Engineering and [2]Department of Anatomy and Neurobiology

2.1 INTRODUCTION

The most basic goal of tissue engineering is to restore lost tissue function. It is therefore important to understand what normal tissue function means and how it is different from a wide range of pathological tissue states. A tissue can be thought of as a collection of cells that function together to perform a specific task.[59] A "healthy" tissue state is a potentially misleading term because, at any given time, a fraction of the base tissue components (the cells) are either dying or actively being destroyed.[60,61] This targeted cell death is a critical part of tissue maintenance and is present as a small, controlled portion of the tissue mass. All tissues exist in a dynamic state in which the balance of chemical and physical signals as well as the general ability of its cells to respond to those signals relegates tissue status and function. In general a healthy tissue is seen as one that successfully performs its intended physiological task while maintaining a functional homeostasis. Clinically, while tissue homeostasis is important, cases of pathology in tissues typically present themselves as a loss of tissue function, pain associated with tissue function, or a combination of the two. It is important to remember that tissue dysfunction is a result of an improper physiological environment (e.g. changes in chemical or physical cues, chemical or physical insult, or impaired cellular function) and that understanding the tissue environment helps guide regenerative therapies.[62-64]

2.2 MAJOR TISSUE COMPONENTS

Cells and ECM Material

Cells are the fundamental currency of living organisms.[59] In complex organisms, one or more types of cells grouped together to perform a specific function or functions are called a tissue.[60] A complete organism is simply a collection of tissues that functions as a unified system that is directed at prolonging existence (either directly by maintaining a homeostatic internal environment or in a more abstract sense i.e. procreating to improve the odds of long-term genetic survival).

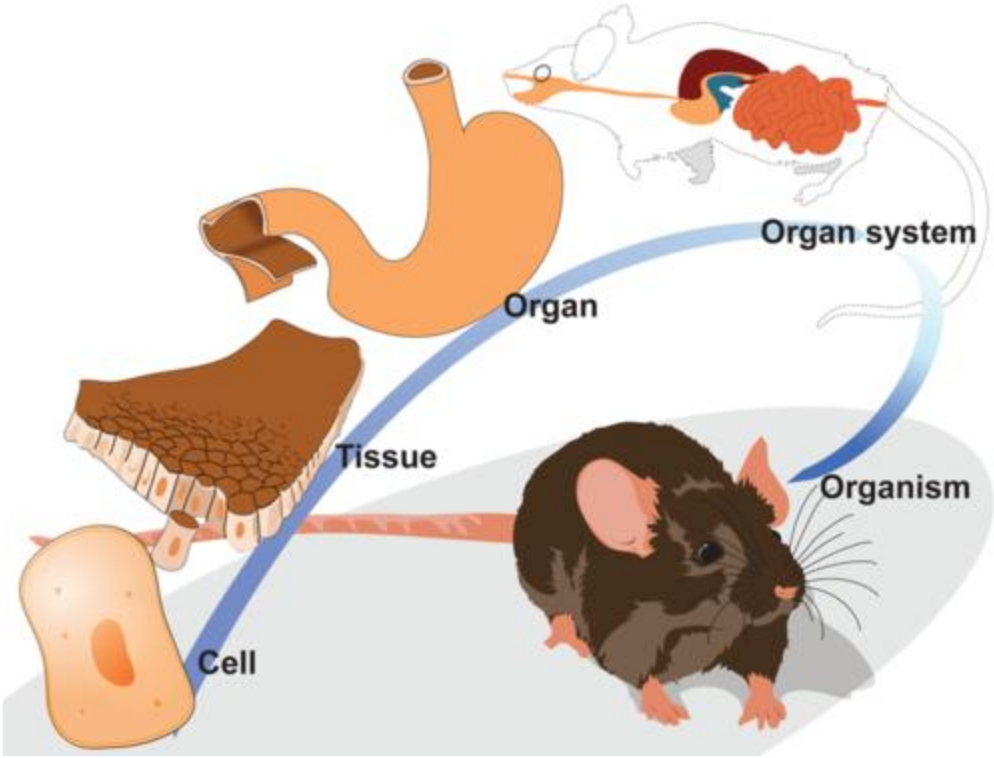

Figure 2.1. *Levels of physiological organization in a mammal.[65]*

The cells that make up an organism can be thought of as workers maintaining a vessel (the non-cellular portion of the body, i.e. the extracellular matrix). These workers have specific tasks (e.g. differentiated cells perform specific functions) that they perform at a basal level (this can range from very active, such as immune cells monitoring the body for foreign insult, or passive such as fibroblasts existing in an almost dormant state as they passively monitor local mechanical and chemical signals) and, if environmental conditions change, the cells respond accordingly. For example, in response to environmental cues and conditions (e.g. serum calcium and bone-promoting hormones, such as bone morphogenetic proteins) osteoblasts may deposit a protein and mineral matrix (mainly collagen and hydroxyapatite) which helps create and maintain the skeletal system.[66] There are over 200 specific types of cells in the human body, including epithelial cells, striated and smooth muscle myocytes (muscle cells), fibroblasts, neurons, stem cells and macrophages and a variety of other circulating blood cells. In general wound healing is a cooperative effort that takes place across a spectrum of different cell types.

Wound healing is a complicated phenomenon to study. Not only do different tissues respond differently to insult and treatment, but identical tissues in different patients respond differently as well.[67-69] Skin is commonly injured and consequently represents one of the most well studied tissues with respect to the wound healing response.[70] Additionally, skin tissue is also easily accessible (e.g. in a rodent model it is much easier to replicate a 6 mm diameter skin lesion than, say, a 6 mm cardiac infarct) and its regeneration can be monitored with little or no direct manipulation because of its superficial location. Different tissues certainly diverge from skin in certain aspects of their wound response, however, they generally share critical recovery milestones (e.g. debridement, targeted cellular infiltration, and revascularization).[63,64] Rather

than controlling the entire wound recovery cascade, many treatment strategies (for all tissues) involve instigating or otherwise encouraging the timely initiation of major wound healing events and then allowing the resulting cascade of poorly understood minor events to take place naturally.[71] Again, the superficial nature of skin makes it possible to observe critical events and critical time points in the wound healing process with the goal of understanding which events need to be carefully monitored and extrapolating this knowledge to different tissues. The superficial and predictable nature of the healing response in skin also makes it possible to observe the process in humans using non-invasive methods.[72]

2.3 CUTANEOUS WOUND HEALING

The cellular compartment of skin is largely occupied by epithelial cells. Epithelial cells that comprise this compartment are the biological interfaces between tissue and non-tissue substance throughout the body.[59] These cells are found on the surface of the skin, blood vessel linings, and the linings of hollow internal organs. This barrier tissue is responsible for the transport and diffusion of beneficial materials throughout the body as well as preventing unwanted materials from penetrating into the body where they can do harm.[59,61] With respect to wound recovery, epithelial tissue is a major focus of research because of its tendency to be replaced by fibrous scar tissue (connective tissue) in more severe adult injuries. When this happens the affected area no longer exhibits epithelial tissue-like properties which can lead to chronic wound-induced tissue dysfunction.[73]

Wounds to the skin that take up a small amount of surface area typically heal quickly, especially when the injury is superficial in nature, because the cells are in close contact with one another. Loss of contact induces cell migration and proliferation, leading to the closures of the wound. Scar tissue is limited and as such the barriers for cell migration are few.[74] Small wounds typically close within a week but, depending on the extent and depth of tissue involved, they can require over a year to fully mature as they regain their original tissue properties. In contrast wounds that involve large surface areas take much longer to undergo healing. Because the tissue loss is large these wounds require dressings or scaffolds to encourage the healing process. Much effort is spent in strategically keeping the wound bed moist because cells cannot easily infiltrate a dry, scarred-over wound bed.[63,74]

It is likely that the actual wound healing process takes place as a spectrum of events rather than easily discernible separate events. Nevertheless it is convenient to conceptualize wound healing through several stages.[59] In a large surface area wound, the first stage of wound healing is hemostasis, or stopping the loss of blood from compromised blood vessels. In response to an injury that physically tears, ruptures, or otherwise compromises a blood vessel, circulating platelets initially adhere to the injured location because of the newly exposed sub-endothelial matrix which contains receptors that bind platelets. The adhesion of the platelets to the injured vessel activates platelet integrins which in turn triggers a physical and chemical change inside the platelets promoting spreading and aggregation, ultimately resulting in a clot.[63,75] The aggregation of large numbers of platelets also facilitates the release of soluble factors, such as platelet derived growth factor (PDGF), that aid in wound healing. The clotting cascade following an injury creates a temporary patchwork of platelets embedded inside a fibrin meshwork.[63,76] This serves the purpose of both stopping the bleed and providing a quick temporary matrix whereby the next stages of healing can take place.[63]

The next stage following hemostasis is a transient inflammatory phase that is associated with improved perfusion (via vasodilation and local angiogenesis) and the activation and migration of a wide range of cells into the wound. Circulating neutrophils are one of the first cell types to infiltrate a wound in a process involving chemical and physical signals expressed by the vascular endothelium at the site of compromised blood vessels. The primary focus of neutrophils is to combat the large initial influx of bacteria characteristic of most wounds. Additionally the cells may release cytokines and growth factors that are known to be released in the early stages of

wound healing, such as those that encourage macrophage and fibroblast infiltration.[77,78] Examples of growth factors released by various cell types at the injury site are epidermal growth factor (EGF), transforming growth factor alpha (TGF-α), and heparin binding epidermal growth factor (HB-EGF). These growth factors are all associated with improved wound closure and increased cell motility into the wound.[79]

The macrophages, in the presence of inflammatory signals (common in most wound beds), become "activated."[80] In this process the macrophages adopt a phagocytic and pro-inflammatory role to rid the wound of harmful bacteria and materials. In normal wound healing the macrophages also engulf any residual neutrophils, dramatically reducing their population in the maturing wound.[63,80] Eventually the wound healing process transitions from the inflammatory stage to a more proliferative stage. This next stage involves infiltration by fibroblasts which begin to express receptors that bind fibrin, fibrinogen, and vitronectin (factors enriched after the initial stages of wound healing at an injury site) in order to facilitate migration into the wound. Once in the wound, fibroblasts synthesize and deposit new extracellular matrix material (collagen, proteoglycans, and fibronectin) within the developing interstitium, participate in the regeneration of matrix components needed for the development of larger caliber blood vessels, and help provide a framework to support the infiltration of other cell types.[63] Through the release of fibroblast growth factor (FGF) and vascular endothelial growth factor (VEGF), fibroblasts, and likely other infiltrating cells, induce angiogenesis in the wound bed to support the metabolic demand of recovering tissues.[63] Fibroblasts also differentiate into myofibroblasts which are strongly contractile and promote wound closure through wound contracture. At the end stages of tissue recovery, the mechanical forces in the wound

environment diminish triggering activated fibroblasts back into their normal quiescent phase while any differentiated myofibroblasts normally undergo apoptosis as fibroblast to myofibroblast differentiation is believed to be terminal.[63,81,82] In both embryonic and adult wound regeneration the wound contracts, however, embryonic contraction does not appear to require fibroblast to myofibroblast differentiation.[83,84] Research indicates that embryonic expression of the TGF-β3 isoform is high and the expression of the TGF-β1 isoform is nearly nonexistent in embryonic tissues, the opposite is true in adult tissues where TGF-β1 is strongly expressed and TGF-β3 is essentially absent. The TGF-β1 isoform is known to induce fibroblast to myofibroblast differentiation and the increased expression of collagen.

In adult tissues the wound healing response in a serious injury usually results in varying degrees of scarring, a non-functional analog of dermis composed of large scale bundles of collagen. In part this is a consequence of the increased expression of collagen in response to pro inflammatory signals such as TGF-β1 . Conversely in embryonic tissues, wound healing, even in serious and extensive injuries, can result in near complete regeneration of the lost skin. The outcome of the healing response in these tissues is not solely determined by profile of TGF-β isoforms that are present, however this signaling difference appears to explain the lack of fibroblast to myofibroblast differentiation in embryonic healing.[81,85,86] In theory this leads to less wound contraction and less aberrant collagen deposition. Clearly, the increased potential for the requirement of stem cell populations into the embryonic wound must also play a role in the reconstitution of normal skin in developing tissues.

The source of final cells for infiltration and regeneration appear to also play a role in dictating outcomes in healing wounds. For example, an active area of research concerns determining how healing might be modulated if a larger or smaller proportion of the fibroblasts that infiltrate an injury arise from circulating fibrocytes (precursors to fibroblasts) versus resident fibroblasts (those that pre-exist adjacent tissue domains that migrate into an injury) . Fibrocytes are less differentiated than resident fibroblasts and may provide benefits to the regeneration process as a result (i.e. more stem cell like). In general the more source cells (those cells with the capacity to take on the proper cell form for regeneration) the better the recovery. For example if a cutaneous injury does not compromise existing hair stumps the residual hair stumps have been shown to contribute a significant portion of the regenerated cell population.[87] Additionally, any injuries that remove the hair bulbs that reside in the dermis result in wounds that do not regenerate hair. This is thought to occur because the wound is infiltrated with deep dermal fibroblasts rather than those existing in the superficial layers. Further, either the deep dermal fibroblasts lose the ability to regenerate superficial dermal layers or the nature of the injury (which must be severe) creates an environment in which the fibroblasts prioritize wound closure at the expense of normal superficial tissue functionality.[88]

Cutaneous wound healing in wet or moist environment has been shown to be significantly faster than wound healing in a dry environment. This is thought to occur because cells naturally migrate over moist surfaces much faster than dry surfaces. Additionally, it's possible that growth factors and other chemical or ionic signals important in wound healing are conserved in moist environments whereas in dry environments they are wicked to the dry surface and lose

their functionality.[74,89,90] Transient hypoxia in the wound bed paired with simultaneous increases in carbon dioxide and decreases in pH creates an ideal environment for fibroblast infiltration and activation. This localized hypoxia also aids in angiogenesis of the wound. Generally a more acidic pH in the wound bed is associated with increased antibacterial activity and better wound healing.[74]

2.4 CONCLUSIONS

The goal of tissue engineering is to move beyond simple passive approach to wound care (just preventing further damage) towards a more active scaffold or dressing that actively encourages a pro-healing environment (e.g. moist, slightly acidic, bacteria free, etc). While this chapter focused mainly on cutaneous wounds, we can extrapolate some general lessons learned from this easily observable tissue to those tissues that are deeper and more difficult to observe on a day by day basis (e.g. nerve, blood vessel).[70,72] It should be noted that, while we learn more about specific reactions in the wound healing process, care must be taken when applying chemical factors positively associated with healing to a wound. For example, plasmin is an enzyme involved in the breakdown of the provisional fibrin matrix in wounds. Its function is central to wound repair because it facilitates the development of the secondary, permanent extracellular matrix and the infiltration of the wound with targeted cells. Despite the positive effects plasmin has on wound recovery, misregulation of plasmin (or numerous other factors) has been associated with chronic wounds, that is, wounds that don't heal through primary wound recovery mechanisms, rather they exhibit prolonged levels of inflammation and poor healing.[91] If treatment is not carefully monitored and controlled it's easily possible to skew the correct chemical balance in a wound.[92,93] It is very evident that a basic understanding of the wound healing process is critical for tissue engineering researchers.

CHAPTER 3

Creating Scaffolds Exhibiting Smooth Mechanical Gradients

Preface: The following manuscript has been published in Biomaterials. It describes the creation of multi-layered electrospun scaffolds that exhibit controllable layer transitions rather than abrupt laminations. With this technology we hope to develop scaffolds that can direct the cellular response to regenerate multi-layered tissues without risking delamination and scaffold failure in process. Additionally, the transition layer may aid to direct infiltrating cells towards a particular phenotype as they infiltrate into the target layer and, acting as a mechanical primer, may aid in the overall regenerative response. By addressing a known weakness exhibited by multi-layered scaffolds, that is, delamination, this manuscript represents the first step in our journey to create clinically relevant tissue engineering scaffolds.

Gradient Fiber Electrospinning of Layered Scaffolds using Controlled Transitions in Fiber Diameter

Casey P. Grey[1], Scott Newton[2],

Gary L. Bowlin[1], Thomas Haas[1], and David G. Simpson[2]

[1]Department of Biomedical Engineering and [2]Department of Anatomy and Neurobiology

Corresponding Author:

David G Simpson, Ph.D.

Department of Anatomy and Neurobiology

Virginia Commonwealth University

Richmond, VA 23298

dgsimpso@vcu.edu

ABSTRACT

We characterize layered, delamination resistant, tissue engineering scaffolds produced by gradient electrospinning using computational fluid dynamics, measurements of fiber diameter with respect to dynamic changes in polymer concentration, SEM analysis, and materials testing. Gradient electrospinning delivers a continuously variable concentration of polymer to the electrospinning jet, resulting in scaffolds that exhibit controlled transitions in fiber diameter across the Z-axis. This makes it possible to produce scaffolds that exhibit very different fiber sizes and material properties on opposing surfaces while eliminating the boundary layers that lead to delamination failures. In materials testing bi-layered laminated electrospun scaffolds (layer 1 = <250 nm, layer 2 = 1000 nm diameter polycaprolactone fibers) exhibit ductile properties and undergo multiphasic failure. In contrast, scaffolds, produced by gradient electrospinning fabricated with fibers of this type on opposing surfaces fracture and fail as unified, and mechanically integrated, structures. Gradient electrospinning also eliminates the anisotropic strain properties observed in scaffolds composed of highly aligned fibers. In burst testing, scaffolds composed of aligned fibers produced using gradient electrospinning exhibit superior material properties with respect to scaffolds composed of random or aligned fibers produced from a single polymer concentration or as bi-layered, laminated structures.

3.1 INTRODUCTION

The extracellular matrix (ECM) and cellular elements of hollow organs and other select tissues, notably, blood vessels, cartilage, and skin, are arranged into layers. The structural and living elements of these layered tissues are mechanically integrated with one another in order to withstand the stresses and strains routinely encountered during normal physiological function. For example, the prototypical artery is classically described to have three distinct layers, each with unique material properties [94,95]; the tunica intima, tunica media, and the tunica adventitia. The actual structure and functional attributes of each layer are far more complex [96] and difficult to capture in a tissue engineered material. The innermost layer, the tunica intima, is composed of a single cellular layer of endothelium resting on, and separated from, the deeper structures by a basement membrane. An internal elastic lamina may be present. The tunica media contains varying layers of smooth muscle cells with an ECM rich in proteoglycans, reticular fibers, and fibrils of Type I collagen. The smooth muscle cells are organized in two principal patterns; the bulk of these fusiform cells are positioned in a radial fashion around the lumen of the vessel and a secondary population is distributed in a spiral pattern along the length of the artery. The tunica adventitia contains larger diameter fibers of collagen, elastic fibers, scattered fibroblasts, nerves, and lymphatics.

While each layer of the prototypical blood vessel exhibits unique structural and material properties, each layer is also mechanically integrated with the adjacent layer, allowing the tissue to function as a unified structure. The transmission of mechanical stresses across the boundary layers that inherently exist where materials of different mechanical properties intersect is critical.

Without true integration, mechanical stresses are concentrated at the interface of the layers, increasing the risk of delamination failure (separation of the layers at the boundary interface). Integration allows these mechanical stresses to be transmitted across the boundary and dissipated into the next layer of material. Arguably, one of the most important factors in the future success of tissue engineered materials is the development of scaffolds designed to mimic the architecture and function of the native target tissue [97,98]. While this is conceptually and theoretically possible, attempts to recapitulate the specific structural elements and functional properties present in an organ using tissue engineering has been largely unsuccessful.

Electrospinning has been, and continues to be, explored as a processing strategy for the production of physiologically relevant tissue engineering scaffolds [99-101]. This adaptable technology can selectively process a variety of native [48,57,102], synthetic [14,103], and blends of native and synthetic [104,105] polymers into nano-to-micron scale diameter fibers that mimic the dimensions of native ECM constituents. First generation vascular constructs produced by electrospinning were composed of uniform fibers that were selected and/or engineered to withstand physiological mechanical loads [106]. Second generation designs exhibit different fiber types that have been deposited into specific layers in order to more closely mimic the structure of the native vessel [50]. Electrospinning makes it relatively easy to produce constructs with a tunica intima-like layer composed of very small diameter fibers that is overcoated with larger diameter fibers to form a composite tunica media/tunica adventitia [17]. The fine fibers of the inner layer provide adhesion sites for cells along the luminal surface while the larger diameter fibers are intended to lend mechanical stability to the engineered construct. Unfortunately, this direct approach, and related methods designed to entangle fibers of different

compositions [17,50,107], produce a laminated structure with boundary layers. From a structural standpoint this type of construct can be fabricated to resemble the architecture of the native ECM. From a functional standpoint, when this simple type of construct is subjected to mechanical loading, stress is concentrated at the interface of the layers and the device can be expected to undergo multiphasic delamination failure [17].

A central challenge in tissue engineering is to create scaffolds that mimic the mechanical and functional characteristics of the target tissue [98]. One clear strategy to reducing the risk of delamination in multi-layered constructs is to modulate the transitional properties of the boundary domains. To our knowledge the production of a continuous fiber gradient in an electrospun scaffold as a strategy to reduce the impact of the boundary layers that inherently exist in any composite material has not been examined with any great detail. Limited experimentation directed at developing functionally graded tissue-engineering scaffolds containing nano-particle gradients have been reported [108,109]. These studies concentrated on evaluating the distribution of the nano-particles across the Z-axis of the electrospun tissue engineering scaffold with respect to conditions that could be used to increase the overall tensile strength of the resulting constructs.

In the present study we describe and characterize the process of gradient fiber electrospinning. This technique makes it possible to produce layered electrospun scaffolds that exhibit a gradual and continuous transition in average fiber diameter across the Z-axis. These transitions reduce the concentration of stress that typically occurs at the boundary of different fiber types. We prototype gradient electrospinning using two different scaffold designs. The first prototype

scaffold (designated “22-gauge”) has one face composed of electrospun polycaprolactone (PCL) fibers with an average cross sectional diameter of 0.17 +/- S.D. 0.09 µm. Average fiber size increases across the Z-axis in this type of scaffold and reaches an average cross sectional diameter of 0.78 +/- S.D. 0.89 µm on the opposite face. The fibers of the second prototype scaffold (“18-gauge”) are similar and range from 0.24 +/- S.D. 0.12 µm on one surface up to 0.89 +/- S.D. 0.96 µm on the other surface. The total overall average fiber diameter, as a population, that is present in the 18-gauge scaffold is larger and it exhibits a steeper “fiber gradient” across the Z-axis than the 22-gauge prototype. These architectural features confer unique material properties to these constructs. The characteristics of scaffolds produced by gradient fiber electrospinning were evaluated against both pure fiber scaffolds (controls) and those produced as laminated structures using: computational fluid dynamics (fluid modeling), output polymer concentration with respect to time (experimental mixing characteristics), output fiber diameter with respect to time (experimental electrospinning characteristics), mechanical testing (tensile/burst, overall scaffold failure properties), and SEM (scanning electron microscope) analysis of scaffolds before, during, and after mechanical testing (failure modes).

3.2 MATERIALS AND METHODS

Computational Fluid Dynamics (CFD)

All computer drawings and meshes developed using Gambit (Version 2.4). Fluid-models were analyzed in Fluent (Version 12.0) using 1,000 iterations or until convergence was achieved, graphical representations prepared in Tecplot. Gradient electrospinning was modeled using a 3 mL plastic BD syringe (ID = 0.876 cm) as a reservoir. The intermediate disk contained a central port sized to the equivalent of a 22-gauge (ID = 0.413 mm) or an 18-gauge (ID = 0.838 mm) needle segment. The high concentration polycaprolactone (65,000 M.W.) solution (top reservoir) was modeled at 200 mg/mL with a viscosity of $1.11x10^7$ kg/m*s and a density of 958 kg/m^3; the low concentration PCL solution (bottom solution) was modeled at 100 mg/mL with a viscosity of $4.6x10^6$ kg/m*s and a density of 951 kg/m^3. Electrospinning outlet was an 18-gauge needle. The model incorporated a mass flow rate of 8 mL/hr. False colors represent the magnitude of fluid velocity, measured in mm/s.

Electrospinning

All reagents were obtained from Sigma unless noted. Polycaprolactone (PCL: 65,000 M.W.) was suspended and electrospun from trifluoroethanol (TFE; 100 or 200 mg/mL). Electrospinning syringes were capped with an 18-gauge blunt-tipped needle and installed into a syringe pump (Fisher Scientific), solutions delivered at 8 mL/hr into a static electric field (18kV, Spellmen). All spinning took place across a 20 cm gap onto a grounded cylindrical metal target (length = 11.75 cm, diameter = 6.33 mm) designed to rotate and translate laterally (4 cm/s over a 12 cm distance) to promote an even coating of polymer. Scaffolds were collected at either 700 rpm

(random) or 7,000 rpm (aligned). Laminated scaffolds were produced by sequentially spinning 100 mg/mL PCL onto the target, this layer was overcoated with a second, separate layer of fibers spun from 200 mg/mL PCL.

Gradient electrospinning

In conventional electrospinning fiber size is positively correlated with increasing polymer concentration [14,110]. By engineering a polymer concentration gradient within the electrospinning reservoir it is theoretically possible to deliver a continuously variable gradient of polymer at the electrospinning jet, in turn, resulting in the production of a gradient of fiber sizes. Traditional methods have attempted to achieve this by entangling different electrospinning jets [111] or mixing different solutions at the orifice of the electrospinning needle(s), however, these strategies lead to inconsistent results, the partitioning of the different polymer streams, and/or scaffolds composed of two interwoven fiber types (not a fiber gradient). We used a single reservoir that contained two separate compartments interconnected by a port designed to control the extent of mixing that takes place between the solutions at a position distal to the electrospinning jet.

Two-chambered electrospinning reservoirs were prepared by placing 1.5 mL of 100 mg/mL PCL into a 3 ml syringe (Figure 3.2). The intermediate disk ("mixing port"), created by piercing the rubber cap of a syringe plunger with an indwelling, 5 mm segment of either a 22-gauge or an 18-gauge needle. This intermediate disk is then positioned on top of the 100 mg/mL PCL solution. Next the syringe is filled with 1.5 mL of 200 mg/mL PCL. The plunger is then installed into the syringe. At the onset of electrospinning, the mixing port remains stationary until the primary

syringe plunger comes into contact with it, at which point it is driven down the length of the syringe. By remaining stationary the mixing port allows the controlled mixing of solutions, thus creating the smooth gradient of polymer (and thus fibers). Engineering the mixing port to move in synchrony with the primary plunger results in a scaffold that appears, and behaves in material testing, like a laminated structure (*i.e.* the moving intermediate port produces an abrupt change in polymer concentration and fiber diameter during spinning).

Instantaneous PCL concentration

Solutions were delivered at a rate of 8 mL/hr into a weighing dish from the electrospinning reservoirs in the absence of an electric field. Fixed volumes of the dispensed PCL solutions were collected at set intervals of time, the solvent was allowed to evaporate, and the sample dry weight was determined and used to extrapolate the instantaneous PCL concentration. For example, if samples were collected at 2-min intervals for 10 min with a flow rate of 8 mL/hr, 5 samples would be collected, each containing 0.267 mL of fluid. By dividing the PCL dry weight by 0.267 mL the instantaneous PCL concentration at each time point can be determined.

Fiber diameter analysis

Electrospun samples were collected for 2-min at 2-min intervals during gradient electrospinning. A Zeiss EVO 50 Scanning Electron Microscope (SEM) was used to image samples. Representative images were captured at 1500x at a resolution of 1024 x 768. Images were overlaid with a uniform half-grid mask and only the fibers that crossed the designated lines were measured. All images were calibrated and imported into ImageJ for fiber diameter analysis [14].

Tensile Testing

A MTS Bionix Tensile Test System (50 N load cell) was used for mechanical testing at a strain rate of 10 mm/min. All scaffolds were prepared from a constant volume of 3.5 mL. Scaffolds were soaked in ethanol (5 min), removed from the mandrel, dried overnight, cut lengthwise, and unrolled. "Dog bone" shaped samples were punched from the scaffolds (ODC Tooling and Molding Sharp-Edge Die: 6.2 x 18.6 mm) along the axis of mandrel rotation ("parallel") and 90 degrees to the axis of rotation ("perpendicular"). A Mitutoyo Absolute caliper was used to determine sample thickness.

Burst Testing

Burst strength testing was completed using a device designed in accordance with section 8.3.3.3 of ANSI/AAMI VP20:1994 [50]. Scaffolds were soaked in ethanol (<5 min), removed from the mandrel, and dried overnight. Intact tubes, 2–3 cm in length, were fitted over 1.5 mm diameter nipples attached to the device, and secured with 2-0 silk suture. Air was introduced into the system (5–10 mmHg/s) until the tubes burst, at which point the peak pressure was recorded. We only consider apparent hoop stress to compare and contrast our constructs in burst testing (Equation 1). We acknowledge that differences in resistance to axial deformation surely exist between scaffolds, however, the extent of axial strain did not begin to approach the limits of failure as determine by tensile testing therefore its contribution to scaffold failure was assumed to be minimal in this study.

$$\sigma_\theta = \frac{Pr}{t}$$

Equation 1. Apparent hoop stress

Where P = burst pressure, r = radius of the construct and t = the wall thickness.

Statistics

All data sets were analyzed in Sigma Plot and screened using ANOVA. The Holm-Sidak method was used for pairwise comparisons. P values as provided. Graphical depictions represent +/- the standard error unless otherwise noted.

3.3 RESULTS

Control conditions

Scaffolds produced from 100 mg/mL control PCL solutions were composed of fibers with an average cross sectional diameter of 0.21 +/- S.D. 0.09 µm (Figure 3.1A). These fibers were interspersed with beads, indicating that we were spinning near the lower limits of polymer concentration necessary to produce fibers. A surprising degree of apparent fiber alignment could be achieved when these scaffolds were collected at 7,000 RPM (Figure 3.1C). Fibers less than about 0.8-1.0 microns in diameter are typically difficult to align in conventional electrospinning systems [110], the beads present in our samples appear to add the momentum necessary to cause some degree of fiber alignment. Scaffolds produced from the 200 mg/mL solutions were composed of fibers with an average cross-sectional diameter of 1.02 +/- S.D. 0.90 µm (Figure 3.1B). As expected, the fibers of these scaffolds exhibited a considerable degree of alignment when collected at 7,000 RPM (Figure 3.1D).

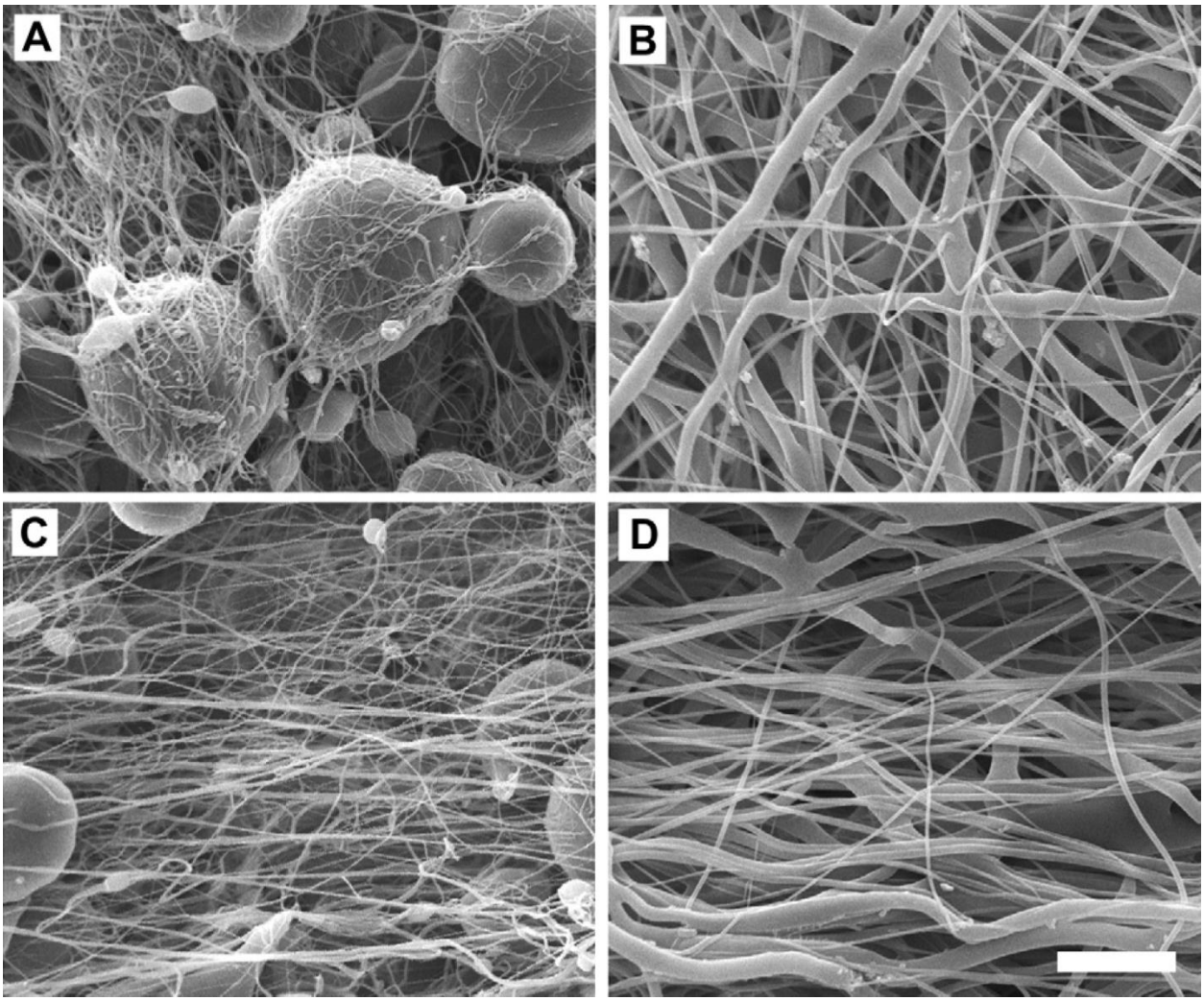

Figure 3.1. *Control conditions. Random electrospun scaffolds (700 RPM) produced with* ***(A)*** *100 mg/mL PCL and* ***(B)*** *200 mg/mL PCL and aligned electrospun scaffolds (7000 RPM) produced with* ***(C)*** *100 mg/mL PCL and* ***(D)*** *200 mg/mL PCL. Bar = 10 µm. Note the small diameter fibers exhibited in scaffolds fabricated with low PCL concentrations (A,C) compared to scaffolds fabricated with high PCL concentrations (B,D).*

CFD modeling

Our approach to producing a continuous and variable concentration gradient of polymer is outlined in Figure 3.2. This CFD model depicts the magnitude of the theoretical fluid velocities

(in mm/s) that result in our gradient fiber electrospinning system using either a 22-gauge (Figure 3.2A, B) or an 18-gauge mixing port (Figure 3.2C,D). The simulations indicate that the fluid velocities in and around the mixing ports are substantially elevated above that of the bulk solution, a condition that should result in varying degrees of polymer mixing in these domains. While the models are similar, it should be noted that the fluid velocities do vary between the systems. This can be demonstrated by overlaying the domains occupied by the 22 and 18-gauge mixing ports and running a difference filter across the images (Figure 3.2E). The CFD model predicts that fluid velocities are higher in the vicinity of the intermediate disk in the 22-gauge system with respect to the same domains in the 18-gauge system, this increased velocity should translate into more mixing and a more gradual concentration gradient in the 22-gauge system. If the CFD model, overall, has validity several measurable characteristics should be detectable, including the formation of a concentration gradient at the output needle of the electrospinning system as a function of time, commensurate changes in fiber diameter as the concentration gradient develops, and distinct scaffold mechanical properties compared to scaffolds produced with no gradient.

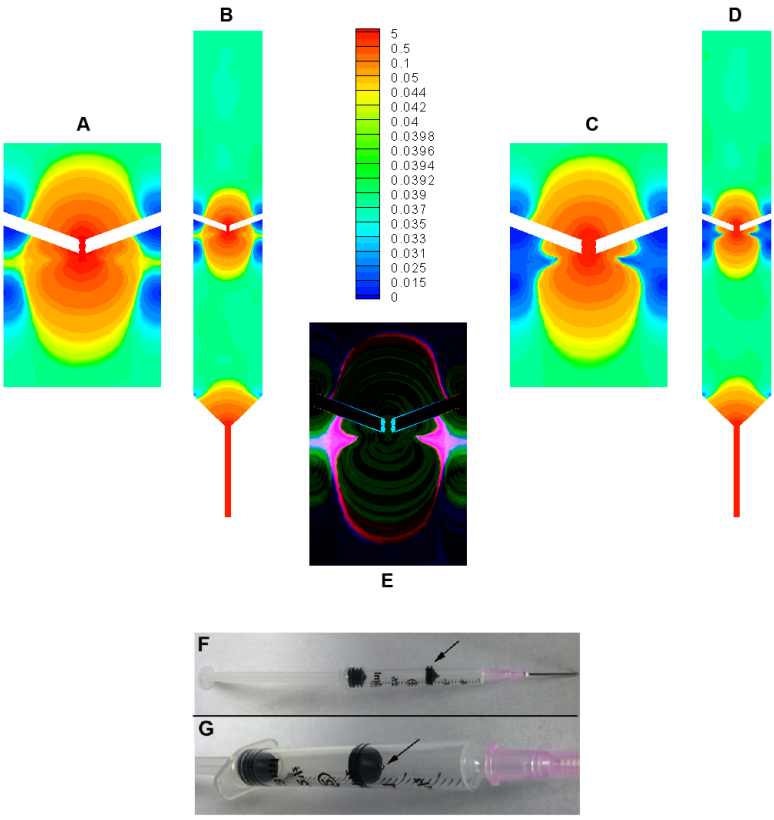

Figure 3.2. CFD. *Fluid model simulations of gradient fiber electrospinning using a 22 or 18-gauge intermediate channel predicted that a substantial increase in fluid velocity (measured in mm/s) occurs at the channel, around the channel, and at the syringe outlet with respect to the bulk solution. This gradient in fluid velocity can be expected to result in controlled mixing between the two fluids, mainly occurring in the vicinity of the intermediate channel.* ***(A)*** *Complete 22-gauge gradient fiber electrospinning* ***(B)*** *detail of intermediate channel.* ***(C)*** *Complete 18-gauge gradient fiber electrospinning* ***(D)*** *detail of intermediate channel.* ***(E)****. Detail of intermediate channel overlay with a difference filter where black represents shared pixel values, false colors indicate areas where the CFD model for fluid velocity diverges in the different port configurations. Extrapolating from these models suggests that a 22-gauge system will have higher velocities and more mixing in domains subjacent to the port.* ***(F)*** *Gradient*

electrospinning syringe, arrow=intermediate plunger with indwelling 18-gauge needle segment as a mixing port. ***(G)*** *Gradient electrospinning syringe, arrow=detail of indwelling 18-gauge needle.*

Instantaneous PCL concentration

To verify that a concentration gradient develops as predicted by CFD we collected PCL solutions as a function of time during a "simulated" (no electric field) electrospinning experiment. In these experiments the extrapolated PCL concentration gradient that developed with the 22-gauge port system (Figure 3.3A) was more gradual (as judged by regression analysis for instantaneous polymer concentration vs. time, not shown) than the gradient developed with the 18-gauge port system (Figure 3.3B).

Fiber diameter analysis

The formation of a continuously variable polymer gradient at the electrospinning jet as a function of time should result in the production of fibers that vary in cross-sectional diameter as a function of the electrospinning interval. In experiments to test this hypothesis the average fiber diameter produced with either port configuration matched that observed in the 100 mg/mL control solutions during the onset of spinning, subsequently, average fiber diameter increased as a function of run time. In the 22-gauge system, the first three "fiber" fractions collected at 2, 4 and 6 minutes yielded fibers that were size matched to the fibers present in scaffolds spun from 100 mg/ml control solutions. From 8 minutes to 16 minutes the fibers produced by the 22-gauge system were intermediate, and different, from the 100 mg and 200 mg controls ($P<0.05$). After 18 minutes the fibers produced with this setup approached and overlapped the range of fiber

diameters present in the 200 mg/mL control scaffold. Overall, the scaffold produced from the 22-gauge system had fibers that were 0.17 +/- S.D. 0.09 µm on one face that ranged up to 0.78 +/- S.D. 0.89 µm on the other face (Figure 3.3C and Figure 3.4).

The 18-gauge mixing system exhibited a steeper concentration gradient that was correlated with a steeper "fiber" gradient than the fiber gradient produced with the 22-gauge system. The first two "fiber" fractions produced using the 18-gauge mixing port and collected at 2 and 4 minutes yielded fibers that were size matched to the fibers produced from the 100 mg/ml control solutions. Over the interval of 6 minutes to 8 minutes the 18-gauge system produced fibers that were intermediate, and different from, the 100 mg and 200 mg controls ($P<0.05$). By 10 minutes fibers produced from the 18-gauge mixing port approximated the fibers present in the 200 mg/mL control scaffolds. Overall, the 18-gauge port system resulted in the production of a scaffold composed of fibers that ranged from 0.24 +/- S.D. 0.12 µm on one face to 0.89 +/- S.D. 0.96 µm on the other face (Figure 3.3D, Figure 3.5 and for cross sectional images 7A random, 7B aligned).

In summary, each port system produced a similar population of fibers; however, the 18-gauge system produced a population that was skewed towards the production of larger diameters at earlier time points in the electrospinning interval. The average cross sectional diameter for all fibers in all fractions produced by the 22-gauge system was less ($P<0.001$) than the overall cross sectional diameter for all fibers in all fractions produced by the 18-gauge system (22-gauge fibers: 0.56 +/- S.D. 0.73 µm, median diameter of 0.29 µm vs. 18-gauge: 0.65 +/- S.D. 0.77 µm, median diameter of 0.35 µm). Consistent with this data, the slope of the regression curve

(average fiber diameter vs. electrospinning interval) generated for the 18-gauge system was steeper and reached a maximal fiber diameter value sooner than the 22-gauge system (not shown).

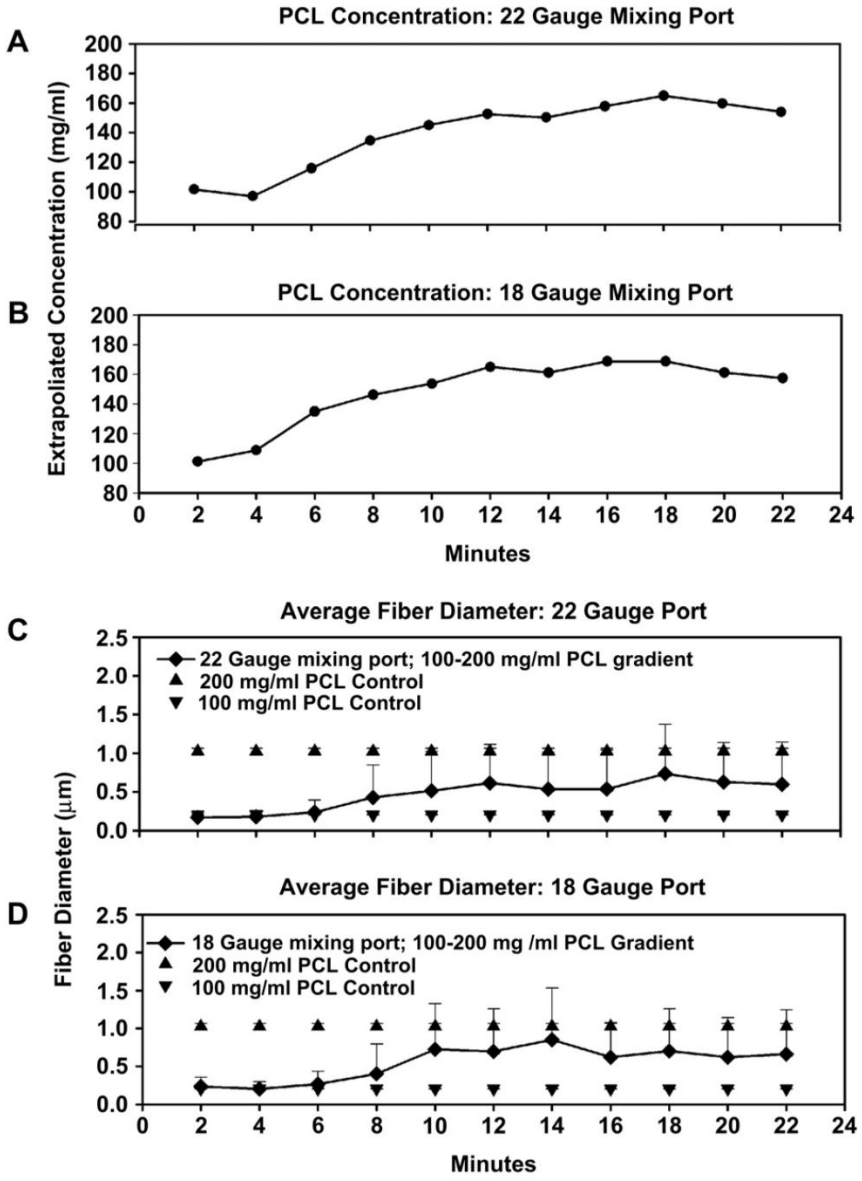

Figure 3.3. *PCL and fiber gradients as a function of time.* ***(A)*** *Concentration gradient produced by 22-gauge port system ranged from 100 mg to a maximal value of 165 mg PCL/mL TFE.* ***(B)*** *Concentration gradient produced by 18-gauge port system ranged from 100 mg to maximal value of 170 mg PCL /mL TFE.* ***(C)*** *Fibers produced by 22-gauge port were 0.170 +/- S.D.*

0.0792 µm at the onset and 0.784 +/- S.D. 0.886 µm at the conclusion. At 2, 4 and 6 min: 22-gauge fibers = 100 mg fibers. From 8-16 min: 100 mg fibers < 22-gauge fibers < 200 mg fibers. At 18-20 min: 22-gauge fibers = 200 mg fibers. At 22 min: 200 mg fibers > 22-gauge fibers. Fibers produced at 8 min < fibers at 10-16 min (all P<0.05). ***(D)*** *Fibers produced by 18-gauge mixing port ranged from 0.235 +/- S.D. 0.121 µm to 0.885 +/- S.D. 0.956 µm at the end of the spinning interval. At 2 and 4 min: 22-gauge fibers = 100 mg fibers. By 6 min: 100 mg fibers < 18-gauge fibers < 200 mg fibers. From 10-16 min: 18-gauge=200 mg fibers, at 18 and 20 min 200 mg fibers > 18-gauge fibers, at 22 min 18-gauge fibers = 200 mg fibers. Fibers produced at 6 min < fibers at 8,10,12,16, 18 min, fibers produced at 8 min < Fibers at 10,12,14,18 and 18 min (all P<0.05). Error bars in C and D denote 1 S.D. in the positive direction.*

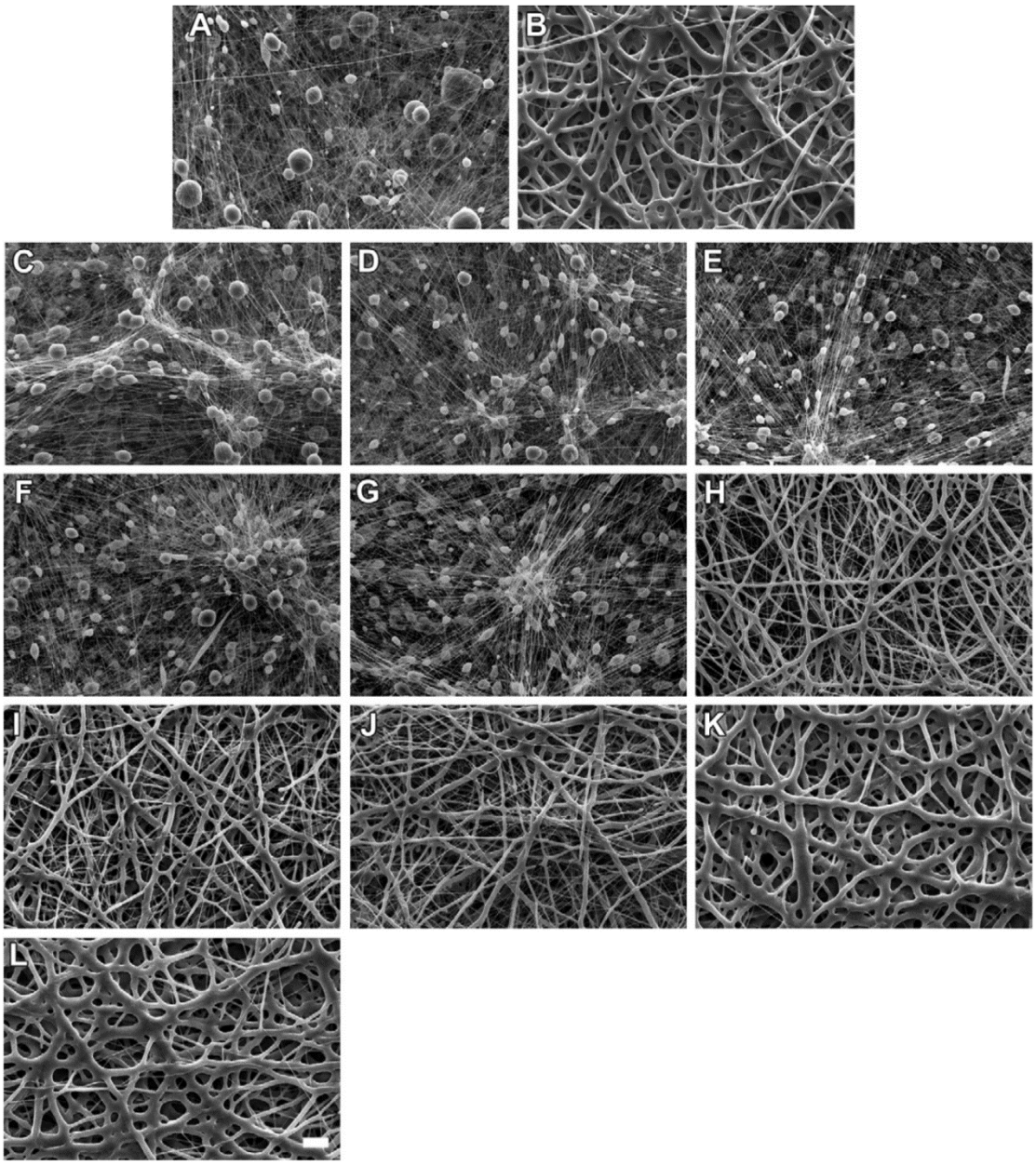

Figure 3.4. *SEM analysis of 22-gauge mixing port gradient electrospinning.* ***(A)*** *100 mg/mL control fibers* ***(B)*** *200 mg/mL control fibers.* ***(C)*** *Fibers produced from a 22-gauge mixing system after 2 minutes.* ***(D-L)*** *Fibers produced at each subsequent 2-minute time interval. Note that with respect to scaffolds produced with the 18-gauge port (Figure 3.5) the increased number "fiber fractions" that display small diameter fibers and beads (e.g. C-G). Bar= 10 µm*

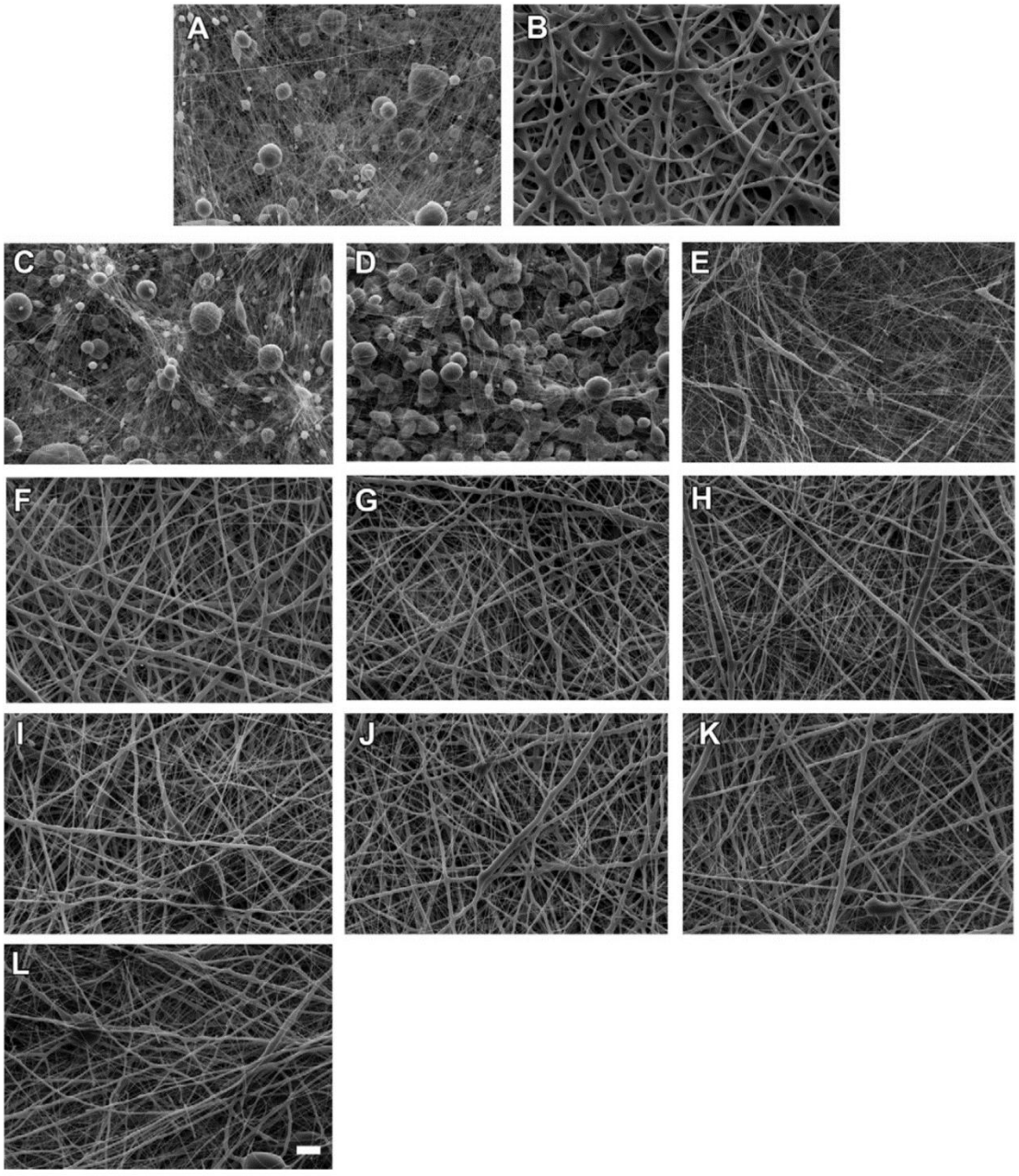

Figure 3.5. *SEM analysis of 18-gauge mixing port gradient electrospinning.* ***(A)*** *100 mg/mL control fibers.* ***(B)*** *200 mg/mL PCL control fibers* ***(C)*** *Fibers produced from an 18-gauge mixing system after 2 minutes.* ***(D-L)*** *Fibers produced at each subsequent 2-minute time interval.*

Scaffolds produced with the 18-gauge system exhibit a "steeper" fiber gradient with respect to scaffolds produced with the 22-gauge system. Bar= 10 µm

Tensile Testing: Random scaffolds

Fabricating a scaffold composed of fibers that vary continuously in cross-sectional diameter across the Z-axis of the construct should be manifest in the guise of unique material properties and mechanical failure characteristics. Much like our gradient scaffolds, a bi-layered laminated scaffold that is sequentially electrospun from a 100 mg/mL PCL solution followed by a 200 mg/mL PCL solution exhibits small diameter fibers on one face and large diameter fibers on the other face. This type of bi-layered laminate, composed of fiber layers with very different material properties, will undergo a delamination failure. Stress is concentrated at the interface of the two fiber layers and they separate from one another at the boundary prior to complete scaffold failure. The production of fibers that are continuously varied in cross-sectional diameter across the Z-axis of a scaffold should eliminate the abrupt boundary layer that is ordinarily present in a laminate structure and completely alter the failure characteristics of the construct.

In the following discussion scaffolds produced solely from either 100 mg/mL PCL or 200 mg/mL PCL will be referred to as 100 mg controls and 200 mg controls. Laminated scaffolds (produced by sequentially spinning 100 mg/mL PCL then 200 mg/mL PCL) will be denoted as 100-200 laminates. Gradient scaffolds produced with the 22-gauge mixing port will be denoted as "22-gauge" and scaffolds produced with the 18-gauge mixing port will be denoted as "18-gauge". The data sets generated during mechanical testing contain considerable information; however, we will focus on the key observations that demonstrate gradient electrospinning

reduces or eliminates the boundary layer that leads to the concentration of stress and delamination failure in conventional bi-layered scaffolds.

The results of peak stress testing were unremarkable. Within each scaffold type, the peak stress values at failure across the parallel axis with respect to the perpendicular axis was statistically identical in each construct (Figure 3.6A). In the parallel direction (with respect to the direction of mandrel rotation), the peak stress for the 200 mg controls was greater than all other scaffolds ($P<0.025$). The 100-200 laminates, 22-gauge and 18-gauge samples were statistically indistinguishable from one another and all were greater than the 100 mg controls ($P<0.001$). In the perpendicular direction peak stress for the 200 mg controls was greater than the 100-200 laminates and the 18-gauge samples ($P<0.024$) and all scaffolds exhibited a peak stress that was greater than 100 mg controls ($P<0.001$). As in testing across the parallel orientation, the peak stress for the 100-200 laminates, 22-gauge and 18-gauge scaffolds was identical across the perpendicular axis.

Peak strain testing revealed a subtle degree of anisotropy was present in the random scaffolds, gradient electrospinning eliminated this fundamental mechanical characteristic (Figure 3.6B). Peak strain was identical in all scaffolds in the parallel direction, however, peak strain was higher in the perpendicular direction with respect to the parallel direction in the 200 mg controls, the 100-200 laminates and the 22-gauge scaffolds ($P<0.001$). Of note, the 100 mg controls and the 18-gauge scaffolds did not exhibit anisotropy in this analysis and were statistically indistinguishable from one another. An examination of the stress-strain curves provides clear

evidence that scaffolds produced by gradient electrospinning have material properties that are fundamentally different from the 100-200 laminated scaffolds.

Stress-strain curves captured in the parallel direction for the 200 mg controls, 22 and 18-gauge scaffolds exhibited a linear function up to well defined peak stress value, the scaffolds then underwent fracture and complete failure (Figure 3.6C). The initial stages of the stress strain function in the 100-200 laminated scaffolds approximated that observed in these scaffolds. However, and in clear contrast, the stress strain function exhibited a broad plateau characteristic of a delamination failure. When tested in the perpendicular direction a more prolonged interval of failure was evident in the 200 mg controls (reflective of the modest anisotropy detected in tensile testing: Figure 3.6B). This interval of failure was greatly exaggerated in the 100-200 laminated scaffolds (Figure 3.6D) and is consistent with a delamination mode of failure. Gradient electrospinning completely eliminated the prolonged interval of failure observed in the 100-200 laminates and resulted in scaffolds that exhibited a well-defined peak stress value and little or no residual strain, regardless of the direction of testing.

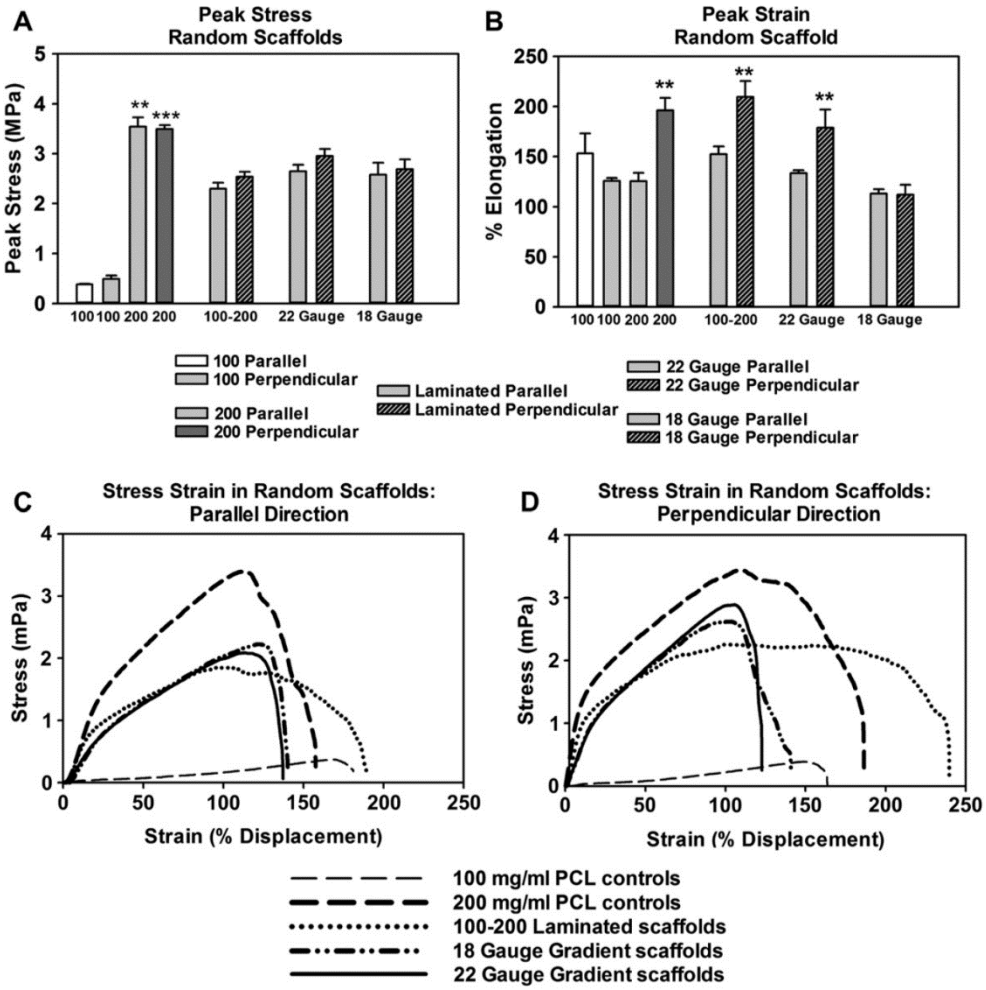

Figure 3.6. *Materials testing: Random scaffolds.* ***(A)*** *Peak stress across parallel axis = peak stress in the perpendicular axis within each scaffold type. Parallel direction only: peak stress 200 mg controls > all scaffolds (**P<0.025), perpendicular direction only: 200 mg controls > 100 mg controls, 100-200 laminates and 18-gauge scaffolds (***P<0.024).* ***(B)*** *Peak strain perpendicular direction > parallel direction in 200 mg scaffolds and 100-200 scaffolds (**P<0.001). Parallel = perpendicular axis in 100 mg controls and 18-gauge scaffolds.* ***(C)*** *Stress strain curves captured in parallel direction.* ***(D)*** *Stress strain curves in perpendicular direction. Note the poorly defined peak stress, characterized by a broad plateau, and increased*

strain after peak stress present in 100-200 laminates, this pattern is consistent with delamination and is absent in the 22 and 18-gauge scaffolds.

SEM: Random scaffolds subjected to conventional tensile testing

SEM analysis confirms that the 100 mg layer of the 100-200 laminated scaffolds initially fails during tensile testing, leaving the 200 mg layer as the load-bearing element (Figure 3.7C and 3.7D). As peak stress is approached in random scaffolds the fibers adjacent to the fracture zone begin to reorient and align along the axis of strain [112]. In 100-200 laminates this process is associated with the displacement, fragmentation and separation of the 100 mg layer away from the intact, and now aligned fibers remaining in the underlying 200 mg layer. In contrast, 22 and 18-gauge scaffolds exhibit two distinct faces, each with a continuous layer of fibers up to the fracture zone (Figure 3.7F).

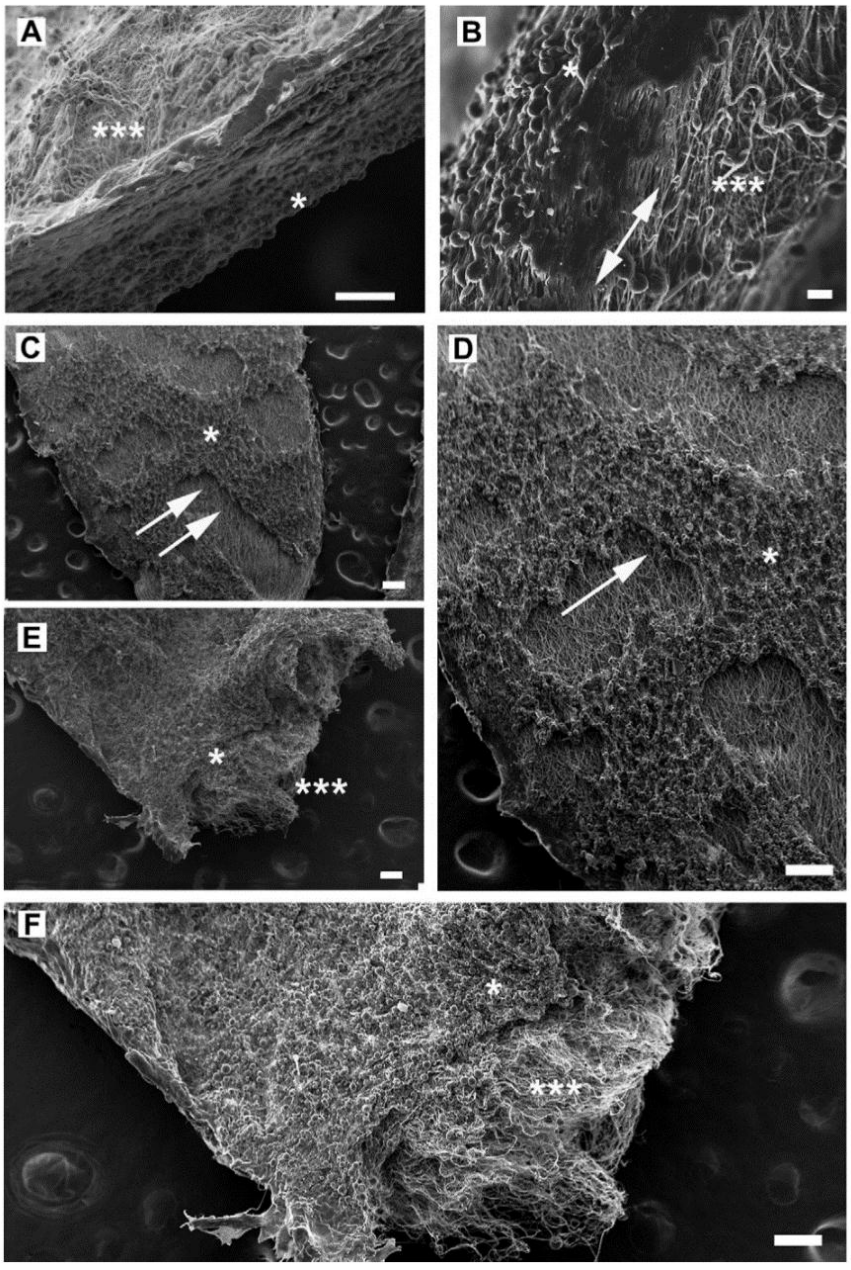

Figure 3.7. *SEM analysis of random scaffold failure characteristics.* ***(A)*** *Cross section through an untested 18-gauge random scaffold. Layer composed of larger diameter fibers on the top surface (***) transitions into heavily beaded dense layer of small fibers (*) bottom of image).* ***(B)*** *Tangential section through an untested 18-gauge aligned scaffold. Top layer (*) in this example is composed of beads interspersed with small diameter fibers that transition into larger diameter fibers (***).* ***(C & D)*** *Double arrow*

depicts axis of alignment. Fracture zone of 100-200 laminate scaffold after testing. The 100 mg layer (*) is fragmented and displaced away from the surface of the underlying 200 mg layer (arrows denote areas where continuity of the layers is lost). Note that fibers adjacent to the fracture zone in the underlying 200 mg layer align (D) as strain is applied to the construct. ***(E & F)*** *Failure of 18-gauge scaffold. The 100 mg fiber (*) layer is continuous across the surface of the 200 mg (***) layer up to the fracture zone. Bar A = 100 µm., B= 20 µm, C, D, E and F= 200 µm.*

Tensile Testing: Aligned scaffolds

To further explore the gradient technique we next prepared scaffolds composed of aligned fibers. This type of scaffold ordinarily sustains high stress and low strain in the parallel direction (along the axis of fiber alignment), and low stress and high strain in the perpendicular direction [113]. In materials testing the peak stress in aligned scaffolds fabricated as 200 mg controls, 100-200 laminates, 22-gauge, and 18-gauge scaffolds was substantially higher in the parallel direction with respect to the perpendicular direction ($P<0.001$: Figure 3.8A). For these aligned samples, peak stress in the parallel direction was also 2-3 times higher than that observed along this same orientation in the random scaffolds. Across the aligned samples, peak stress in the parallel direction for the 200 mg controls was greater than all other scaffolds ($P<0.001$); the 100-200 laminates, 22-gauge and 18-gauge samples were statistically identical and all three were greater than the 100 mg controls ($P<0.001$). In the perpendicular direction, peak stress for all samples also was statistically identical (and approximately 50% of that observed in random 200 mg, 100-200 laminates, 22-gauge and 18-gauge scaffolds tested along this same axis). Taken together, these results confirm the aligned nature of these constructs.

In strain testing, and as expected, the peak strain in the 200 mg controls and the 100-200 laminates was similar and both were higher in the perpendicular direction with respect to the parallel direction ($P<0.001$). These anisotropic strain properties were ***completely eliminated*** in aligned scaffolds produced by gradient electrospinning. Peak strain in the 22 and 18-gauge aligned scaffolds was statistically identical in the parallel and perpendicular directions. In addition to these results, the 100 mg aligned scaffolds did not exhibit anisotropy in the analysis of peak stress or peak strain, it seems likely that the beads present in these constructs serve to reduce anisotropic behavior (SEM reveals that fibers are entangled on the surface of the beads, Figure 3.1A). This fiber layer appears to impart this characteristic on the 22 and 18-gauge scaffolds. This striking effect can be observed in the stress strain curves.

The function of the stress strain curves in the parallel direction for the aligned 200 mg control scaffolds was similar to that observed in the random 200 mg control scaffolds. The stress strain function for the aligned scaffolds exhibited a linear domain leading up to a well-defined peak stress followed by almost immediate scaffold failure (Figure 3.8C). As expected, the stress strain function for the 200 mg aligned scaffolds was flatter and more elongated when tested along the perpendicular axis (*i.e.* elongation takes place at very low levels of stress, Figure 3.8D). The initial portion of the stress strain function for the 100-200 mg laminates was similar to the 200 mg controls and the 22 and 18-gauge scaffolds, however, once peak stress was achieved in these samples there was a dip in stress characterized by one or more plateaus, indicative of sequential failures in the laminated scaffolds (Figure 3.8C). A similar pattern was observed in the perpendicular direction (Figure3. 8D). This prolonged interval of failure was

absent in the 22 and 18-gauge scaffolds. Regardless of orientation, the stress strain curves for these gradient scaffolds exhibited a linear function that increased abruptly to a well-defined peak stress followed by complete scaffold failure with little or no residual strain.

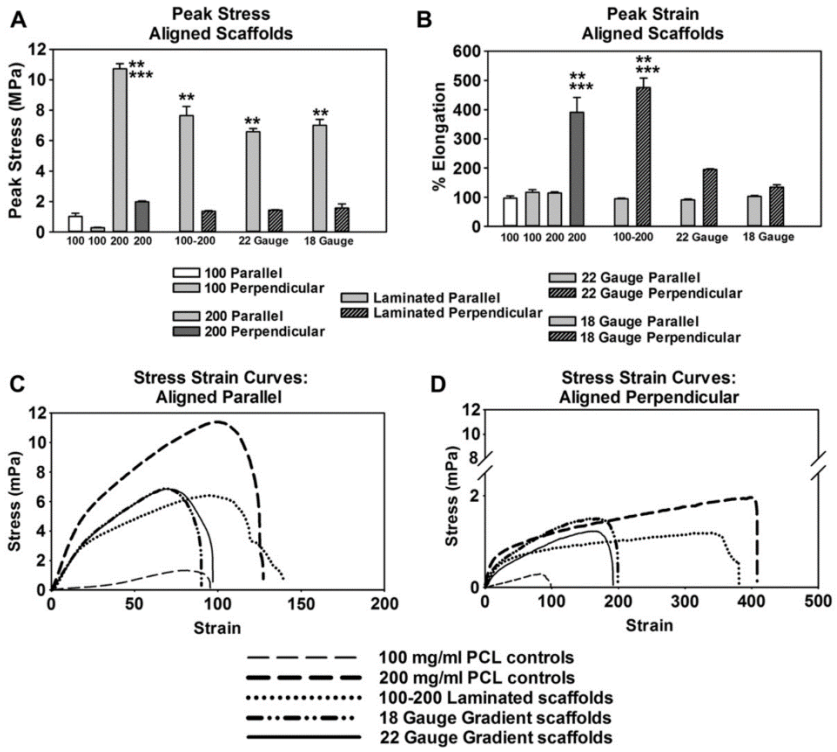

Figure 3.8. *Materials testing: Aligned scaffolds.* ***(A)*** *Peak stress across the parallel axis > peak stress in perpendicular axis for 200 mg controls, 100-200 laminates, 22-gauge and 18-gauge scaffolds (** P<0.001). Parallel direction only: peak stress 200 mg controls > all scaffolds (P<0.001); 100-200 mg = 22-gauge = 18-gauge samples > 100 mg controls (***P<0.001). No differences across treatments in perpendicular direction.* ***(B)*** *Peak strain in perpendicular direction > parallel direction in 200 mg controls and 100-200 laminates (**P<0.001). This anisotropy was not present in 100 mg controls, 22-gauge or 18-gauge scaffolds. Perpendicular direction only: peak strain for 200 mg scaffolds = 100-200 laminates > 100 mg, 22 and 18-gauge scaffolds (***P<0.001). Parallel direction only, no differences across treatment groups*

was detected. ***(C)*** *Stress strain curves captured in parallel direction.* ***(D)*** *Stress strain curves in perpendicular direction. Stress strain curves for 22 and 18-gauge scaffolds are similar, regardless of orientation, and that each exhibits a well-defined peak stress and very little residual strain after the peak stress is reached. Stress-strain curves for 100-200 mg laminates exhibited distinctive, elongated plateaus.*

Aligned scaffolds subjected to conventional tensile testing

As noted for random scaffolds, the 100 mg layer of aligned 100-200 laminated scaffolds is separated and displaced away from the underlying 200 mg layer during tensile testing (Figure 3.9A-D). In aligned 100-200 laminated scaffolds that have been tested in the parallel direction (along the fiber axis) the fibers of the 100 mg layer are pulled away from the 200 mg layer, often as a complete and intact sheet. Testing the 100-200 laminates in the perpendicular direction also results in the delamination of the 100 mg layer. Simultaneously, the aligned fibers of the underlying 200 mg layer undergo a degree of separation from one another and become partially re-oriented along the axis of testing. Scaffolds produced with the 22 or 18-gauge mixing ports exhibit two distinct surfaces at the fracture zones. Once face composed of small diameter fibers interspersed with beads and one composed of larger diameter, and highly aligned larger diameter fibers.

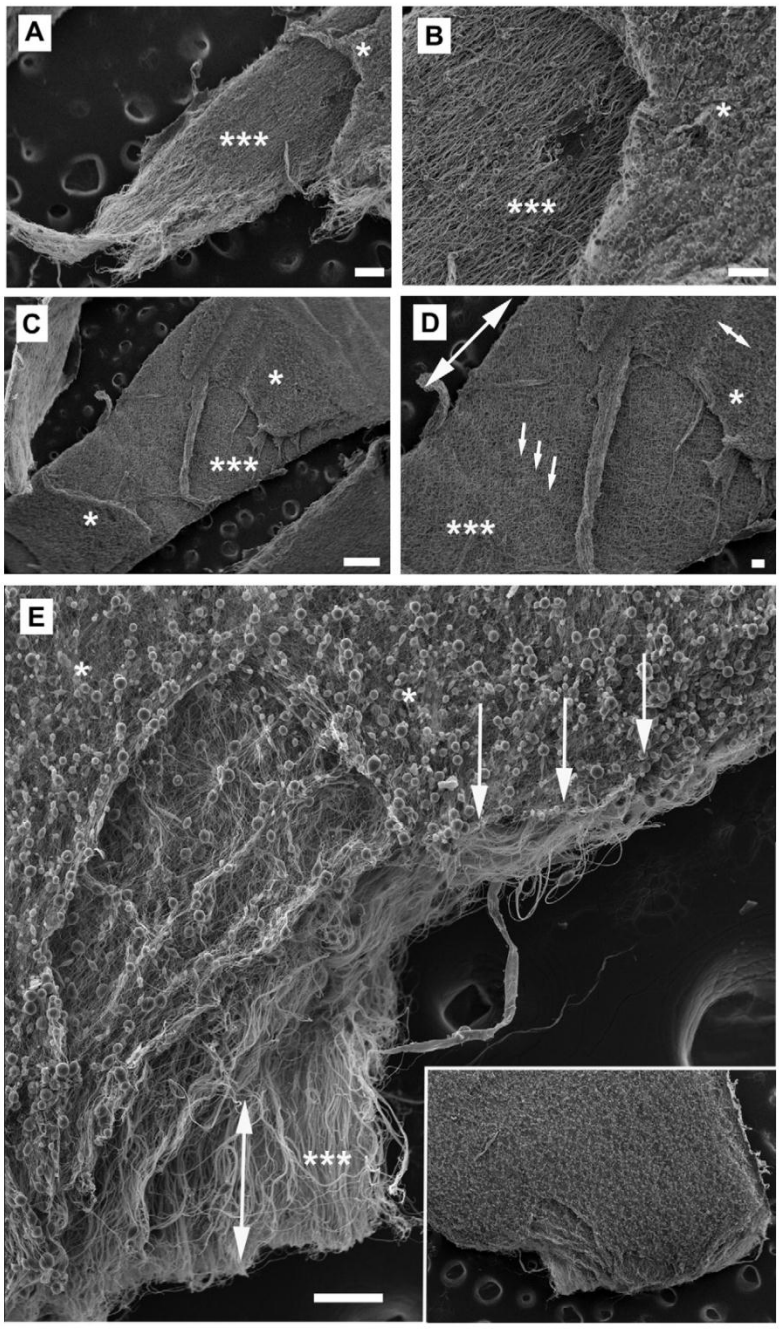

Figure 3.9. *SEM analysis of aligned scaffold failure characteristics.* ***(A)*** *Delamination of the 100 mg layer from the 200 mg layer adjacent to the fracture zone in 100-200 laminate scaffold tested in the parallel direction.* ***(B)*** *Scaffold from A: detail of delamination zone.* ***(C)****. A 100-200 mg laminate tested in the perpendicular direction* ***(D)*** *Scaffold from C: detail of delamination. Arrows indicate partial reorientation of fibers away from the perpendicular axis.* ***(E)*** *Fracture zone of aligned 18-gauge scaffold tested in the parallel direction. Note the nearly unified nature of the fracture, arrows. Inset is low magnification image of entire fracture zone. For all images: * 100 mg layer; *** 200 mg layer. Long double arrowhead= direction of strain. Small double arrowheads (D and E) indicates orientation of fibers prior to testing. Bar in A=200, C=500, B, D, E=100 µm.*

Burst Testing

Cylindrical constructs targeted to the reconstruction of hollow organs are subject to complex mechanical forces along multiple directions. Burst testing represents a critical metric of assessment for these structures. In random scaffolds (collected at 700 RPM) the apparent hoop stress at failure was similar in all samples and no statistical differences were detected across the treatment groups (Figure 3.10). Inducing fiber alignment in the cylindrical constructs substantially altered the material properties of the scaffolds. Apparent hoop stress in the aligned 200 mg controls, 100-200 laminates, and 22-gauge scaffolds was greater than the matched random counterparts ($P<0.002$). The 18-gauge aligned gradient scaffolds exhibited a higher apparent hoop stress than all other scaffolds ($P<0.02$).

SEM: Scaffolds subjected to burst testing

SEM analysis provides clear evidence that scaffolds produced with an 18-gauge mixing port and subjected to burst testing have unique structural properties (Figure 3.10). The catastrophic failure of laminated scaffolds during burst testing results in the nearly complete obliteration of the 100 mg fiber layer. The destruction is so complete that it is difficult to find domains on the remaining elements of the 200 mg layer that contain evidence of these fibers. Only small and scattered domains of the 100 mg fiber layer remain in these constructs. In contrast, the scaffolds fabricated using the 18-gauge mixing port exhibited two distinct faces after failure; one face was composed of a continuous layer of large diameter fibers. The other face was composed of interconnected domains of the 100 mg fibers. This layer was clearly stretched and damaged during burst testing, however it remained attached to the underlying fibers of the 200 mg layer.

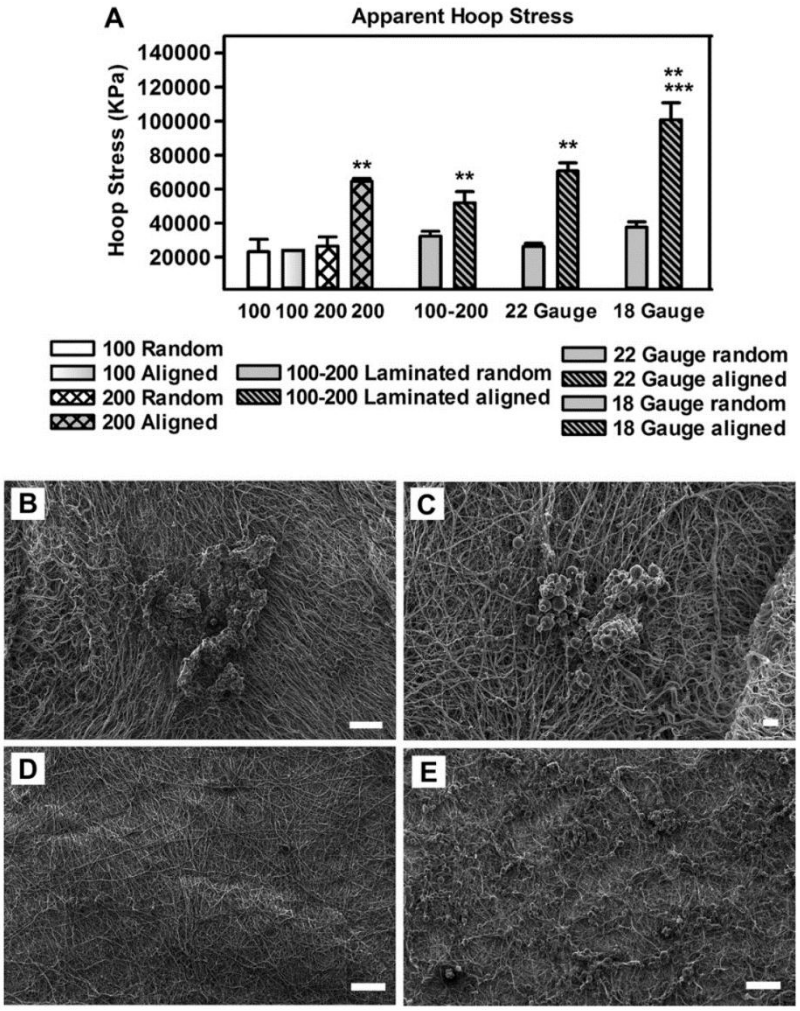

Figure 3.10. *Apparent Hoop Stress and SEM Analysis of Burst Test Failures.* ***(A)*** *Average thicknesses for scaffolds are as follows: 100 Control – Aligned (0.0160 in), 100 Control – Not Aligned (0.0153 in), 200 Control – Aligned (0.0147 in), 200 Control – Not Aligned (0.0163 in), Integrated 18G – Aligned (0.0080 in), Integrated 18G – Not Aligned (0.0132 in), Integrated 22G – Aligned (0.0140 in), Integrated 22G – Not Aligned (0.0147 in), Laminated – Aligned (0.0150 in), Laminated – Not Aligned (0.0140 in). No differences in apparent hoop stress were detected across random scaffolds. Apparent hoop stress in aligned 200 mg controls, 100-200 laminates, and 22-gauge scaffolds > matched random counterparts (**P<0.002). Hoop stress in 18-gauge aligned gradient scaffolds > than all other scaffolds (***P<0.02).* ***(B & C)*** *SEM analysis illustrating widely isolated islands of 100 mg material present in 100-200 mg laminates after burst testing.* ***(D)*** *SEM analysis of surface structure 18-gauge scaffold subject to burst testing: 200 mg layer* ***(E)*** *Surface structure 18-gauge scaffold subject to burst testing; 100 mg layer.*

3.4 DISCUSSION

The ECM and cellular elements of many tissue and organ systems are distributed into layers that vary in size, identity, degree of anisotropy, and intrinsic material properties. Such complex architectural patterns serve to modulate the physical properties of the tissue and provide phenotypic cues to the resident cells [114]. With the development and continuing maturation of the regenerative medicine discipline it has become increasingly clear that producing tissue-engineering scaffolds which can truly mimic the structure and function of the native extracellular matrix represents a daunting task. Conventional electrospinning systems can superficially replicate many aspects of the native extracellular matrix with respect to fiber size and composition. Composite scaffolds can easily be produced as laminated structures using basic techniques. For several reasons these layered structures are largely unsuitable as tissue engineering scaffolds. First, and foremost, layered electrospun scaffolds do not function as unified structures; they lack the transitional boundaries that serve to effectively transfer mechanical stresses between layers in native tissues. This leads to the concentration of stress at the boundary layer and subsequent delamination. Second, and unlike the native extracellular matrix, the fibers of electrospun scaffolds are deposited almost exclusively in the X and Y-planes with virtually no fibers oriented and/or entangled with one another across the Z-direction (perpendicular to the X and Y-plane). Finally, electrospun scaffolds are composed of distinct fibers that lack the accessory proteins that serve to bridge between and form crosslinks between the adjacent fibers of native tissues. To some extent solvent and melt-welding [115], the introduction of physical cross-links, or the use of external fixtures can be used to stabilize laminated tissue-engineering scaffolds, usually at the expense of overall porosity [116], bio-

compatibility, and/or physiological performance [117]. While delamination failures can be eliminated by any number of engineering solutions, the challenge is to create a structure that mimics the mechanical and functional characteristics of a biological tissue [98].

Polymer mixing properties

Mixing properties in gradient fiber electrospinning are largely mediated by an interaction between the mixing port and bulk solution properties. CFD analysis indicates that varying the diameter of the intermediate channel in the mixing port, even a small amount, yields different fluid mixing properties of the system. Changes in the fluid mixing ultimately affect the characteristics of polymer outflow from the device which leads to differences in scaffold properties. While it remains to be fully explored, the fluid mixing differences seen in the model may explain why the scaffolds produced with the 18-gauge mixing system appeared to outperform the scaffolds produced with the 22-gauge port in some materials testing experiments.

Materials testing

In tensile testing, the 100-200 laminated scaffolds approximated two individual scaffolds tested in parallel and, when these were intact, these constructs resisted stress very much like the 200 mg control scaffolds and scaffolds produced using the two reservoir gradient. The material properties of the 100-200 laminated scaffolds markedly diverged from the other constructs once the 100 mg fiber layer failed, which resulted in a noticeable decrease in the slope of the stress-strain curve, but not complete mechanical scaffold failure. This change in slope occurs because the load is carried exclusively by the 200 mg layer which continues to resist the load for a considerable time after failure of the 100 mg layer. This biphasic mode of failure is visually

evident in watching the test, physically manifest in the amount of residual strain after the peak stress that is observed in the 100-200 laminated samples, and graphically depicted in the stress strain curves by a poorly defined peak stress with a broad plateau region. Scaffolds produced with the 22 or 18-gauge mixing ports exhibit small diameter fibers on one face, large diameter fibers on the other like the 100-200 laminated scaffolds, yet fail as a unified structure.

One of the obvious effects of gradient electrospinning was a reduction in mechanical anisotropy. Random 18-gauge scaffolds exhibited peak stress values that were identical to the 100-200 laminates yet lacked the modest degree of anisotropy detected in the strain analysis for the 200 controls, 100-200 laminates and the 22-gauge scaffolds. This same effect was observed, and was even more pronounced, in the aligned samples. The aligned 100-200 laminates, 22 and the 18-gauge scaffolds all exhibited the same anisotropic properties in peak stress testing. All displayed far higher peak stress values in the parallel direction with the respect to the perpendicular direction, a hallmark of an aligned electrospun scaffold [110,113]. Conversely, strain was higher in the perpendicular direction with respect to the parallel direction in the 200 mg controls and the 100-200 laminates. This anisotropy in the strain analysis was completely suppressed in the 22 and 18-gauge scaffolds. These results, together with our SEM analysis demonstrate that gradient spinning produces unified structures. The integration of the 100 mg layer, which lacks anisotropic properties, into the anisotropic 200 mg layers of these scaffolds stiffens these constructs in the perpendicular direction and reduces peak strain values.

The results of our burst testing were equally definitive. In this test there is no capacity for a scaffold with biphasic failure tendencies to sustain any measurable stress after the least-

expandable element fails. The 100-200 laminates, under increasing radial pressure, expand to the degree dictated by the 100 mg fiber layer. Once this fiber layer fails, the 200 mg layer undergoes immediate and catastrophic failure. This rapid successive failure takes place because the scaffold initially resists a large amount of stress, however, the 100 mg layer fails at a far lower strain level than the 200 mg layer. Once the 100 mg layer fails the remaining scaffold is comparatively less thick than the original scaffold and, as such, unable to withstand the forces imparted on it by the burst test. Ultrastructural examination of the laminated scaffolds near the location of failure after burst testing revealed that the 100 mg layer is almost completely obliterated during this catastrophic delamination failure. Only small and extremely isolated islands of 100 mg layer were found still attached to the 200 mg layer. In contrast, scaffolds produced by gradient electrospinning were mechanically integrated, at failure these scaffolds exhibited a remnants of the 100 mg fibers at regular intervals on one face and 200 mg fibers on the other face after burst testing.

CFD Modeling

Through CFD modeling we were able to determine that the polymer concentration gradient and the rate at which the fiber gradient develops during electrospinning can be manipulated with even small changes in the diameter of the port. Additional experimental variables that were not modeled, but would still likely change mixing dynamics include length of the port, viscosities of the solutions (ratio of viscosities), the internal delivery dynamics of the reservoir (*e.g.* plunger velocity), temperature, solvent, solution compatibility (resistance to mixing), reservoir orientation (*e.g.* vertical vs. horizontal electrospinning), electric potential, and solution conductivity. While a model that includes all of these variables would be complex to a fault, we

believe that a simplified model that encompasses only port diameter, port length, solution viscosities, plunger velocity, and reservoir orientation would be both adequately representative and experimentally feasible.

3.5 CONCLUSIONS

Gradient electrospinning makes it possible to produce scaffolds with two distinctly different surfaces, one composed of small diameter fibers of PCL and one composed of larger diameter fibers of PCL. Average fiber diameter varied continuously across the Z-axis of these structures, resulting in a scaffold with unique material properties that failed as a unified structure. CFD modeling of different gradient fiber electrospinning experimental setups could enable researchers to predict and tailor scaffolds based on predicted mixing properties. Gradient electrospinning may provide an avenue to developing complex composite structures targeted to replace blood vessels, other hollow organs, cartilage, cardiac valves, and skin. At present we are exploring how this approach can be used to combine different types of polymers, of particular interest in our laboratories is to determine if we can produce composites of native proteins that transition into blends of native proteins and synthetic polymers. We are also examining how these unique composite structures and the resulting mechanical gradients can be used to promote physiological communication and/or the migration of cells into electrospun scaffolds.

CHAPTER 4

The Development of a New Protocol to Improve the Physical Sectioning of Fibrous Scaffolds: Obtaining Frontal Sections through a Modified Cryosectioning Technique

Preface: After the development of gradient fiber electrospinning and subsequent pilot studies regarding cellular infiltration into both single and multi-layered electrospun scaffolds it became clear that current methods of scaffold analysis were inadequate in determining the extent and characteristics of cellular infiltration into these constructs. Without the definitive ability to understand how cells interact with the architecture of a scaffold, that is, across the scaffold face and through its' depth, we could justify no further scaffold modifications or in-depth cell penetration analysis until appropriate techniques were developed. To address this limitation a novel cryosectioning protocol was employed, this method makes it possible to obtain serial frontal sections from electrospun scaffolds. Microscopic images assembled into montage images from serial sections was then used to create three-dimensional (3D) models of the cellular interactions that take place in the scaffolds. Additionally, several pilot experiments were conducted to design more extensive infiltration studies. In order to use a design loop to adjust scaffold properties it is necessary to develop tools that can be used to characterize how cells interact with tissue engineering scaffolds. In short, it necessary to know the starting conditions and ending conditions in order to make rational decisions about how to redesign scaffold properties to modulate cell distribution.

AN IMPROVED PROTOCOL FOR CRYOSECTIONING LARGE AREAS OF FIBROUS SCAFFOLDS – FRONTAL SECTIONING AND Z-STACKS

Casey P. Grey[1] and David G. Simpson[2]

[1]Department of Biomedical Engineering and [2]Department of Anatomy and Neurobiology

ABSTRACT

Electrospun scaffolds offer much promise in the field of tissue engineering as substrates for physiological regeneration. A major challenge when working with these scaffolds is determining whole scaffold cell-matrix interactions. The structure of scaffolds composed of dense arrays of nano- to micron-sized diameter fibers strongly scatter light and make it difficult to physically section these constructs. These characteristics limit data acquisition by scanning confocal and two-photon microscopy to very small regions and to depths of approximately 100 μm. Conventional physical sectioning techniques are commonly used to cut these constructs in cross-section due to the structural properties of the scaffolds which make cutting frontal sections extremely difficult and imprecise. Cross-sections supply good point infiltration data but very little spatial information regarding cell-matrix interactions. Here we detail a cryosectioning protocol that allows for the isolation of consistent serial frontal sections. By taking frontal sections it is possible to conduct microscopic analysis at specific scaffold depths (z-axis) over large surface areas. Data sets acquired from these samples are then processed for modeling using novel 3D reconstruction techniques.

4.1 INTRODUCTION

Electrospinning is a technique that can be used to produce three-dimensional (3D) tissue engineering scaffolds composed of nano- to micron-sized fibers fabricated from natural proteins,[48,49] synthetic polymers, [9,51,100,118] and blends of natural proteins and synthetic polymers.[119-121] The versatility of this fabrication technique allows considerable control over the composition, mechanical (e.g. tensile strength, elasticity, etc) and structural (e.g. fiber size, fiber alignment, scaffold shape, scaffold porosity, etc) properties of the resulting constructs.[5,9,103,122] Electrospinning produces a unique class of nanomaterials that can be utilized in a wide variety of biological applications, for example, electrospun scaffolds have been used to investigate how cells interact with 3D environments of varying compositions,[123,124] they have been used recently in efforts to test pharmaceutical agents on 3D cultures [125,126] and, in a more esoteric application, electrospinning has been proposed as a method for fabricating organs and tissues targeted for replacement therapy.[127-129] Understanding, promoting, and regulating the extent of cellular penetration and population of electrospun scaffolds is fundamental to each of these potential applications and considerable effort has been directed at achieving this objective.[9,120,130]

The refractive nature of the fibers that comprise an electrospun scaffold limits the utility of conventional light and confocal microscopy in the analysis of electrospun scaffolds.[126,131] Even with two-photon microscopy the structural properties of these constructs limits imagining to a maximum depth of approximately 100 μm, and even then the resulting z-stack data represents a small fraction of the entire surface area of the

scaffold.[131,132] Several laboratories, including our own, have used cross-sectional analysis of samples taken from frozen sections or histological preparations in order to judge the extent of cellular penetration into electrospun scaffolds.[5] However, given the complex surfaces and wide distribution of cells in electrospun materials it is difficult to characterize the depth and extent of cell penetration throughout an entire scaffold using these methods. Data collection in this type of analysis is usually limited to a few selected sections taken from the scaffold and, without a comprehensive morphometric approach, this type of analysis often results in a highly subjective and biased analysis of the samples.

Tissue engineering scaffolds targeted for use in reconstructive therapy are typically designed to mimic the dimensional characteristics of the native target tissue.[9,101,122,133] For example, the wall of a native, small diameter artery may reach nearly 500 μm in thickness in an adult, ostensibly requiring a scaffold of approximately the same dimensional characteristics to act as a graft.[134,135] In this example, due to the inherent limitations imposed by the structure of the scaffold, the spatial cell-matrix information for the majority of the scaffold would be unobtainable. Developing methods to better understand how cells interact on a global scale throughout a tissue engineering scaffold represents an important element of the design process. Without this type of information it is difficult to make rational decisions concerning what changes in structure, nutrient support, and/or seeding conditions might be necessary to modulate cell distribution and function. Scaffold structural considerations are too often based on limited data (e.g. cross sectional samples) at best and, at worst, academic guesswork. In this study we describe a method in which we are able to take serial frontal sections through the entire thickness of frozen electrospun scaffolds. This represents one method that provides nearly

unambiguous information concerning the depth and distribution of cells within a given scaffold design. By reconstructing data collected from the individual serial sections into a three-dimensional model it is also possible to explore how regional variations in scaffold structure impact cell-matrix interactions.

4.2 MATERIALS AND METHODS

Electrospinning

All reagents Sigma unless otherwise noted. Polycaprolactone (PCL: 65,000 M.W.) was suspended and electrospun from trifluoroethanol (TFE) at concentrations of 150 mg/mL (producing small fibers with beads) or 250 mg/mL (producing large fibers). Electrospinning syringes were capped with a blunt-tipped 18-gauge needle and placed into a syringe driver (Fisher Scientific) set to deliver the electrospinning fluid into an 18 kV-21 kV static electric field at a rate of 8 mL/hr across a 20 cm gap.[9] A solid cylindrical metal mandrel (length = 11.75 cm, diameter = 6.33 mm) or a perforated cylindrical metal mandrel were used as ground targets (functional length = 11.75 cm, mandrel diameter = 6.33 mm, pore diameter = 0.75 mm spaced laterally 2 mm and vertically 1.5 mm).[5,9] The target mandrels were designed to rotate and translate laterally (4 cm/s over a 12 cm distance) in order to facilitate an even distribution of fibers.

Cell Culture

Human dermal fibroblasts (hDF, Cascade Biologics C-013-5C) were cultured in DMEM-F12 (Gibco) supplemented with 10% fetal bovine serum (FBS, Hyclone) and 1% penicillin/streptomycin (P/S, Invitrogen). For cell culture experiments 6 mm diameter and ~1mm thick circular samples were punch cut from electrospun scaffolds (Figure 4.1) and sanitized in a 70% ethanol wash for 30 min followed by two phosphate buffer solution (PBS) rinses and one media rinse.

Figure 4.1. *Top-view of 6mm diameter electrospun sections.*

Scaffolds were seeded with 25,000 cells and cultured in an incubator set to 37^{o}C and 5% CO_2. Cell culture media was change every 3 days. For analysis, populated scaffolds were fixed in 10% glutaraldehyde in phosphate buffer solution (PBS) for 10 minutes followed by two rinses in PBS. Samples were placed in fresh PBS and stored at 4^{o}C until processed for analysis. Samples were cut into 50 µm thick serial sections as described in this study and stained with 4',6-diamidino-2-phenylindole (DAPI) and or rhodamine phalloidin.

Image Acquisition

Montage images of each serial section were prepared from data captured with a Nikon TE300 microscope equipped with a 10x objective and a DXM 1200 digital camera, all images captured at a resolution of 1280x1024. Brightfield images were overlaid with fluorescence images using the photomerge function of Adobe Photoshop CS4. 3D scaffold reconstruction was done using Google SketchUp Make.

4.3 RESULTS

Cryosectioning sample preparation and cutting protocol

1 – Samples are placed into a 30% sucrose solution prepared in phosphate buffer solution (PBS) for 3 days at 4^{o}C. This extended incubation period is used to insure that the scaffolds are fully infiltrated with the sucrose and cryoprotected during subsequent processing. Poor sucrose infiltration results in inconsistent cell preservation and scaffold fragmentation during cutting. This one of the most critical steps in this protocol (typical procedures call for 1 hour submersion in sucrose which resulted in very poor frontal sectioning).[136]

2 – Samples are removed from the sucrose solution and placed directly into a "cryomold" containing sufficient OCT embedding media to fully submerse the scaffolds. We have found that Fisher, flat-bottom culture dish works well as a cryomold. Avoid leaving unfrozen samples in liquid OCT for extended periods of time as this will reduce rhodamine staining of actin. Staining can be conducted on individual sections or on complete scaffolds depending on the nature of the samples to be processed and the timing of that processing (i.e. stained samples should not be stored for extended periods of time or fluorescence intensity will decrease).

3 – A non-seeded (scrap) scaffold of identical size to the sample to be processed is directly on top of the cell seeded sample.

4 – The entire cryomold is then placed inside the cryostat onto the cryobar (Figure 4.2) and, using a press tool, the sample is quickly submerged and flattened by pressing it down to the

bottom of the cryomold until all OCT had solidified. In this step the scrap scaffold mitigates physical damage to the scaffold from the press tool and provides a backing for when the press tool is removed (see Figure 4.3). The press tool was a semi-rigid, flat-bottom cylinder of similar size to the sample. We used a 5mm diameter, 2.5 cm long cylindrical eraser refill for this study (Helix, Grandville, MI).

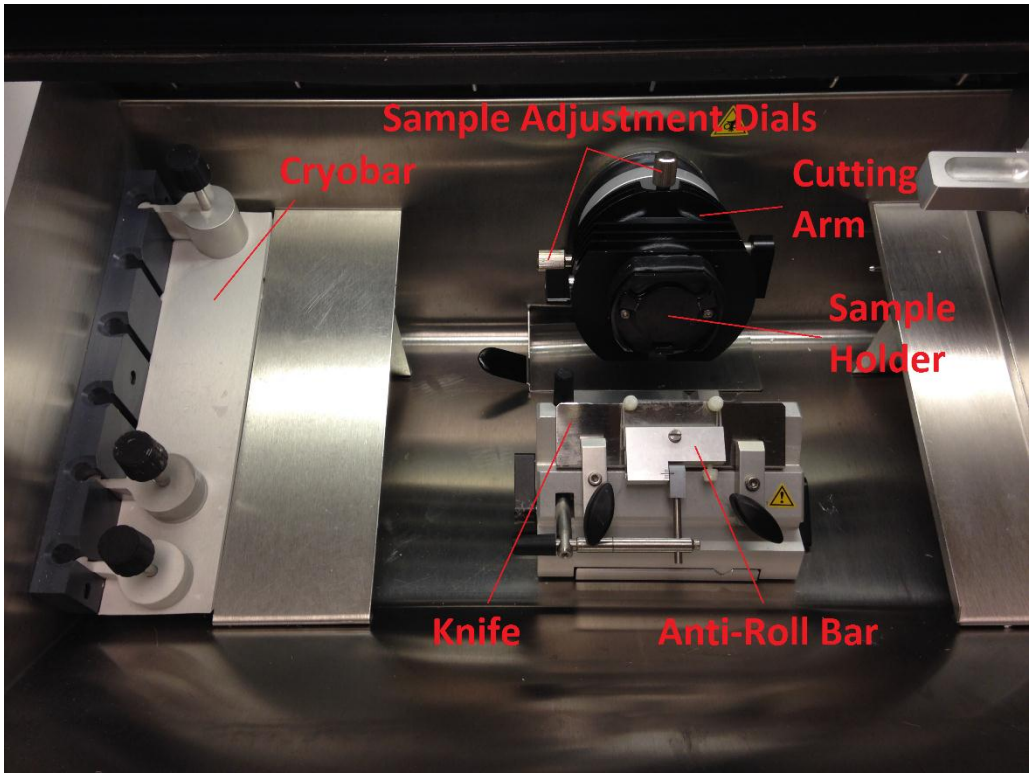

Figure 4.2. *Typical cryosectioning chamber. Temperatures used were as follows: cryobar (-35°C), chamber (-25°C), specimen (-34°C to -36°C).*

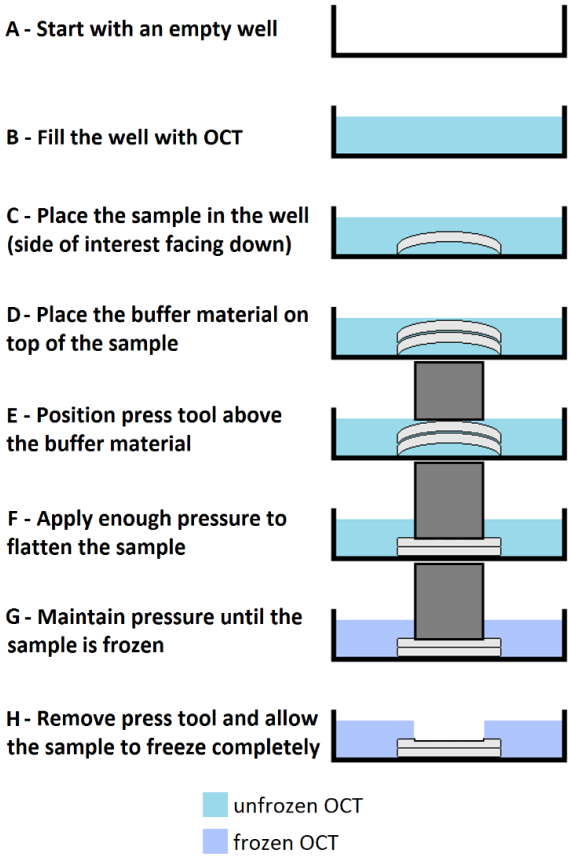

Figure 4.3. *Flattening and freezing a sample for cryosectioning. The flattening process is critically important – ensuring the sample is flush with the bottom of the flat bottomed cryomold allows for accurate alignment of the first, crucial serial section. Steps A-D are completed outside of the cryosectioning chamber (room temperature) while steps E-H are completed inside the cryosectioning chamber, on the cryobar or on an equivalent pre-cooled metal mass. Steps E and F must be completed quickly after placing the sample in the cryosectioning chamber to prevent the premature freezing of the sample in an un-flattened state (e.g. if a sample has residual tension, such as when electrospinning onto a small diameter mandrel, it will tend to curl).*

5 - Once the OCT in the cryomold has solidified the press tool is removed by gentle twisting, keeping the sample on the cryobar at all times. The scrap scaffolding facilitates this process.

6 – Frozen samples were allowed to fully solidify on the cryobar (3-5 min). At this point all tools needed for process (forceps, brushes, knife, etc) are placed into the cryochamber and allowed to come to sectioning temperature – use of cold tools prevents melting of the frozen OCT during handling and is critical for efficient sectioning.

7 – Frozen scaffolds are recovered from the cryomold and affixed to a textured cryosectioning plate using OCT. This is accomplished by placing the frozen scaffold flush onto textured plate, submerging it slightly into gel, and then immediately placing the sample back onto the cryobar to complete the mounting (the gelled OCT freezes to secure the sample to the plate). Do not allow the frozen scaffold to melt during this process.

8 - Once the sample is mounted onto the cryosectioning plate, the plate is secured to the sectioning arm of the cryostat and allowed to come to temperature (3-5 minutes).

9 - Aligning the sample with the knife edge is crucial. Bring the sample as close to the knife as possible (without touching) and align it as flush as possible to the blade. If the sample is not aligned properly the ensuing cut will yield only a portion of the section. If this happens, re-align the sample based on the previous cut and re-section. We store cut sections in a 48-well tissue culture plate supplemented with PBS. Retain any sections that may have been taken that are misaligned as these samples still represent the surface of the sample. Useful data can still be

extracted from these samples. It takes practice, patience, and experience to properly align the scaffold.

10 – For PCL scaffolds, one rotation of the cutting cycle per second was used to process the frozen material. The rate of travel across the knife blade that produces the best sections can be expected to vary to some degree by the nature of the sample processed.

11 – Once cut, each section is recovered from the knife surface with cold, fine tipped forceps, grasping the samples at the edge causes minimal damage. Each section is kept separate and placed into PBS (24, 36, and 48 well plates work well for this process), rather than onto a dry microscope slides. This serves a dual purpose; first, placing samples directly into PBS quickly dissolves any residual OCT and ensures that the samples stay hydrated; the hydration step improves overall image quality. Second, dissolving the residual OCT mitigates the concerns regarding reduced rhodamine staining mentioned above. Third, the PBS bath is very forgiving and helps to flatten or unfurl sections that may have folded during recovery. Immediate hydration also helps samples to remain flat or return to a flattened form if folded during handling. Manually flattening a sample after placement onto a dry microscope slide is extremely difficult as the delicate samples tend to tear rather than unfold.

12 - Sections can either be stored in PBS at 4^{o}C (assuming slow scaffold degradation rates) or stained and imaged immediately. Wash each sample well with fresh PBS to remove residual OCT. Place a drop of PBS onto a microscope slide or coverslip and, using fine-tipped forceps, transfer a cut section onto the microscope slide and into the drop of PBS drop (some less-stiff

samples will fold in on themselves once they are moved from the wells but generally unfold once resubmerged in the PBS droplet, manual manipulation was rarely required with the PCL scaffolds). Place a coverslip over the sample and remove the excess PBS so that the sample is flattened. The sample can then be imaged and either placed back into its original well for storage or, if desired, the coverslip can be sealed and the sample stored on the slide. Of note, placing the sandwiching samples between two microscope coverslips (eliminating the microscope slide) for imaging simplifies flipping the samples over to investigate either side of the scaffold in detail.

Image analysis

Our objective is to develop methods to characterize the distribution of cells within an electrospun scaffold on a global scale. To achieve this objective we systematically captured overlapping images across the entire surface of each individual 50 µm thick cryosection (total surface area=28-30 mm^2 of surface area for each complete scaffold section). Prior to moving the image field of view images were captured first in the bright field channel and then in the fluorescence channel, this insures registry between the two image data sets. The entire surface of each cryosection was imaged and then individual images were imported into Adobe Photoshop for assembly into a montage using the auto-merge function. Paired bright field and fluorescence images were first combined to produce a composite image, the fluorescence channel was then turned off. The individual composite images were then assembled into a montage that represented the entire surface area of each serial frontal section. The brightfield channel was used in this assembly process because images collected from the fluorescence channel (especially if DAPI images are required) lack sufficient data density to for the automerge function to assemble the montage (i.e. an image of widely distributed nuclei does not have

enough image terrain features to allow the algorithm to assemble the individual microscopic image fields into a montage).

Montage images from each individual frontal section were imported into Google SketchUp and placed in a z-stack orientation within the workspace (Figure 4.4A). To facilitate modeling we increased the distance between each frontal section by a factor of ten to better visualize scaffold layer properties. Montage composite images were aligned in the vertical orientation using scaffold features or fiduciary marks placed within the scaffolds prior to embedding (see Figure 4.5). This process was greatly simplified in this study because the exemplar scaffold was fabricated using air impedance electrospinning, a process that produces large scale features that penetrate the scaffold in the Z direction.

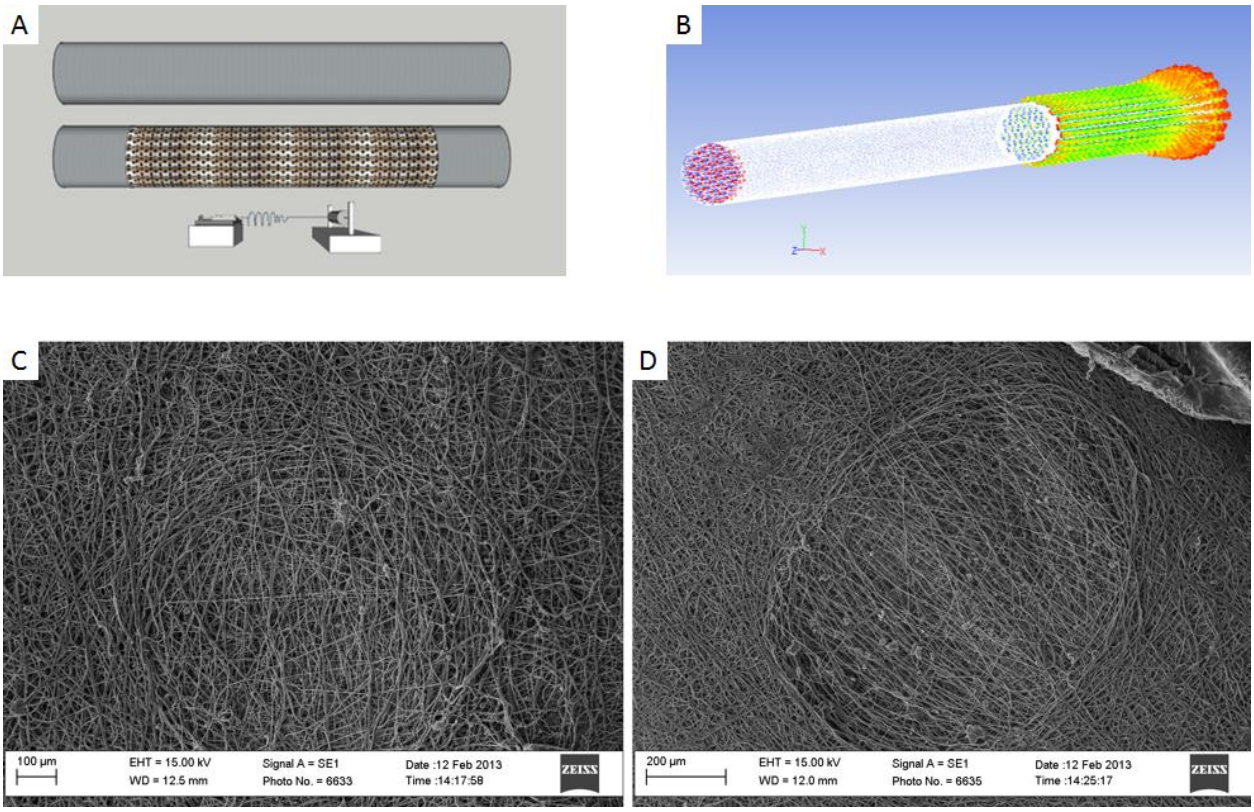

Figure 4.4. *Air impedance electrospinning. A) Depicts the two mandrels used in this study, solid mandrels (top) produce scaffolds composed of randomly oriented fibers whereas perforated mandrel (bottom) produce scaffolds that exhibit regions of increased porosity (see C, D). B) Computational fluid dynamics analysis of air flow out of perforations (pores) of an air impedance mandrel. Achieving uniform air flow throughout the length of the mandrel is extremely difficult. C) Scanning electron micrograph of an electrospun scaffold fabricated on an air impedance mandrel with no air flow (notice the macropore region in the center). D) Scanning electron micrograph of an electrospun scaffold fabricated on an air impedance mandrel with 100kPa air flow through the pores (notice the fibers begin to align and porosity is increased).*

To model cell position a 3D shaded rendering of a cylinder approximating the cross-sectional dimensions of a cell was created and used to replace the DAPI nuclear images marking the position of each cell within the scaffold (Figure 4.5B). We note here that the 3D shape used for cellular representation in this model arbitrary. In some cases it may be helpful to use different shapes, such as spheres, to improve cell visualization, however, it should be noted that this is only a representation of the location of the cell, not a depiction of actual cell shape.

Once all of the cells have been represented by a shaded cylinder (or other 3D object) in the montage z-stacks, the bright field image channel was turned off (Figure 4.5C) allowing just the 3D distribution of the cylinders that marked each cells position to be visible. Because cells tend to primarily occupy the surface and sides of the represented scaffold we created a digital slice in

the scaffold and rotated each half away to better reveal the position of cells that were embedded within the depth of the electrospun scaffold (Figure 4.5D).

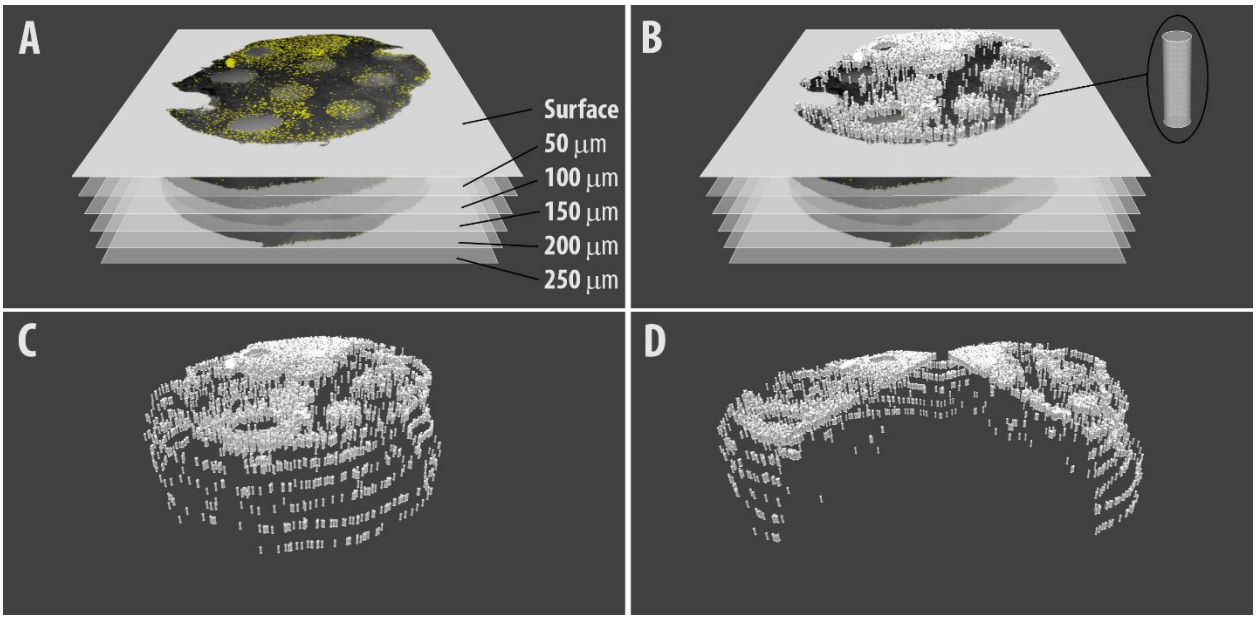

Figure 4.5. *Construction of a three dimensional model of cellular infiltration. A) Images are imported into the workspace and separated by a factor of 10. B) A three dimensional object of choice is used to replace each DAPI positive nuclei to represent cell location in space. C) The bright field channel images depicting the scaffold fibers are turned off. D) To better visualize cell penetration within the scaffolds a digital section was prepared and the opposing images were rotated to reveal the distribution of cells within the scaffold.*

4.4 DISCUSSION

Inadequacies of current techniques

Conventional confocal optical imaging techniques are limited to approximately the first 100 µm of a fibrous scaffold and, as a result, cannot adequately provide data on the distribution of cells on a global scale within a large scale construct. And, in order to capture more than a fractional amount of the surface area of the sample multiple Z image stacks must be collected and analyzed, a data intensive process from the prospective of microscope time, computer time and the time necessary to process the data images. Conventional cross sectional analysis (sections taken perpendicular to the surface of a scaffold) can theoretically obtain data similar in nature to the data generated by a frontal section technique. While this is possible, pragmatically frontal sectioning has several advantages compared to conventional cross sectioning. First, sections taken with this modified cryosectioning protocol retain better structural integrity and are subject to less physical damage (e.g. scaffold stretching, tearing, and distorting is less prevalent). Second, only relevant frontal sections need be analyzed. As a hypothetical example, cells are seeded onto the top surface of an electrospun sample that is 6 mm in diameter and 1 mm thick. Then, assume this particular scaffold supports the infiltration of cells to a depth of 200 µm (cell penetration to this depth is common in our lab when seeding onto scaffolds consisting of large fibers - data not shown). It would require taking 120 total 50 µm-thick conventional cross sections to capture data from the entire scaffold. From a practical prospective, it is unlikely that all 120 sections of this scaffold would be recovered, leaving gaps in the data set. In contrast, if frontal sections were taken, stained with DAPI and accessed the fluorescence marking the presence of cells would be present in only the first 5-6 frontal sections (Figure 4.6). Capturing

data from only the relevant sections of the sample simplifies data acquisition and accelerates image processing time. To summarize this example, cross sectioning the entire scaffold would require 120 total sections, all of which would have to be stained and imaged whereas frontal sectioning would require 20 total sections, only 5 of which would have to be stained and imaged. Third, data acquisition is also accelerated because the sample is physically cut into z-stack data sets. This bins the cells into unambiguous, specific Z depths, allowing a low magnification objective to be used during data acquisition.

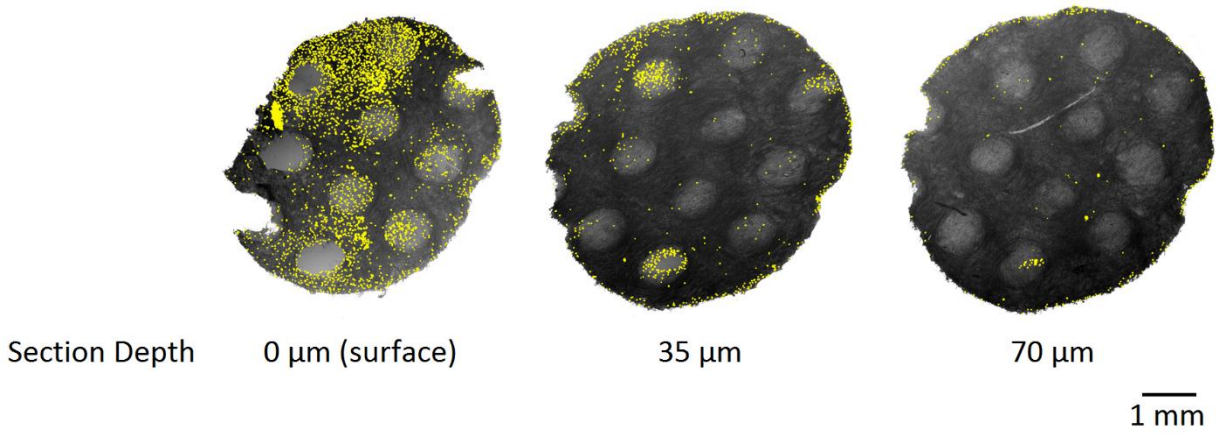

Figure 4.6. *Consecutive frontal images of an electrospun scaffolds seeded with human dermal fibroblasts stained with DAPI (yellow). Note how data management can be monitored by examining sections prior to image acquisition. Once some predetermined threshold of cells has been detected in the scaffold frontal sections the data sets are prepared for z-stack assembly. In this example, the majority of cells were present in the first 70 µm of the sample and subsequent frontal sections were excluded from the analysis. The large scale pores present in this scaffold were used to align the samples in the vertical direction prior to z-stack assembly.*

Storing frontal sections is also more convenient compared to storing conventional cross sections. In the example described and using 48 well plates to store sections (each section in one well) from each scaffold, cross sectioning would require 3 complete plates to store one scaffold whereas using frontal sectioning, 2 separate scaffolds could be stored in a single plate. Because fewer wells are used, the total amount of imaging reagent (e.g. DAPI or other fluorescence markers) required for staining the frontal sections is greatly reduced compared to the conventional sections (despite cross-sectioned samples having a smaller volume, the amount of reagent necessary to cover a sample is dependent on the sample thickness which, in this case, is the same). From a data output standpoint, cross sections depict the extent of cellular infiltration at a specific location (as does confocal microscopic analysis), data obtained from a frontal section reflects how local features impact the depth of penetration over a large surface area. This type of data might otherwise be lost in a conventional cross section. In our study, despite the large scale nature of the pores induced by air impedance electrospinning that were present in the scaffolds, it was not possible to clearly identify these features in conventional cross sectional analysis whereas they are easily distinguished in frontal sections (Figure 4.6).

3D Modeling

As noted, cell distribution and the extent of cell infiltration can be rapidly determined from individual frontal sections (Figure 4.6). In this figure the scaffold sections have been aligned, placed side-by-side for examination and projected with the appropriate depth and scaling legends. However, frontal sections are highly amenable to 3D reconstruction and modeling. Entire scaffolds may be reconstructed in this manner may be reconstructed (see Figure 4.7 for a partial reconstruction). The latter method may be useful if cellular infiltration is

location specific and high resolution images are required.

Insufficient interfiber spacing and or low scaffold porosity (despite the enormous void space that is present in these constructs) are commonly cited as factors that limit the penetration of cells into an electrospun scaffold. With caveats, our limited observations in this study largely support these assumptions. Scaffolds produced by air impedance electrospinning exhibit regions of lower fiber density and increase interfiber distances due to flow of air (Figure 4.6, 35 µm deep frontal section). These regions support increased cell penetration. However, this same analysis reveals that scattered cells are present in regions distal to these large scale features. It is unclear at this time if these scattered cells represent cells that have directly penetrated the scaffold or if these cells represent a population that first entered the large scale pores and then migrated laterally to reach these domains. One puzzling result we observed in this preliminary study was the presence of cells at depths of up to 350µm into the scaffolds after only one day in culture. Regardless of porosity or the physical nature of the scaffolds this would imply that the cells migrated into the scaffolds at rates that exceed current known maximum migration rates of 15um/hr. [137] This suggests the cells reach these depths by sieving through regions of the scaffolds that contain the more widely dispersed fibers (i.e. in regions were the air flow has induced more interfiber spacing) rather than by actively migrating. Future research should be directed at determining whether cellular infiltration primarily involves a single mechanism (e.g. active cellular migration) or whether there are multiple mechanisms governing specific phases of infiltration.

We hypothesize that the latter will prove true in the form of an initial passive phase of infiltration (e.g. cells simply sieve into the scaffold when seeded) followed by a secondary active phase of cellular infiltration (e.g. locomotive based cellular migration). The initial passive phase of infiltration is likely modulated by an interaction between scaffold porosity (with higher porosities reducing the likelihood of sieving cells contacting and becoming entangled with the fibers) and adhesion events between the seeded cells and the surrounding fibers of the electrospun matrix. At one extreme a scaffold exhibiting small pores and composed of materials that support high rates of cell adhesion (for example collagen) would exhibit a limited cell sieving phase. Conversely scaffolds with large pores and composed of synthetic materials that limit charge-based cell adhesion and receptor-mediated events can be expected to support a longer passive phase of cell sieving.

4.5 CONCLUSION

We described a modified cryosectioning protocol that addresses a major limitation in the analysis of electrospun scaffolds. This method provides unambiguous data concerning the extent to which cells penetrate a scaffold on a global scale. Our preliminary observations suggest that penetration occurs in a biphasic fashion. The early stage appears to be characterized by a rapid and passive sieving of cells through regions of the scaffold that exhibit increased interfiber spacing. The secondary stage is slower and likely driven by active migratory events (e.g. cellular locomotion). One consequence of this preliminarily model would suggest that cell infiltration can be maximized by employing interventions that prolong the passive phase of infiltration. This might be achieved by actively delaying cell adhesion events and promoting the retention of a rounded cell shape to facilitate the sieving process.

CHAPTER 5

Exploring Cellular Infiltration Patterns into Electrospun Scaffolds with Homogenous and Non-Homogenous Fiber Properties

Preface: In this study we explore how modulating the structure of an electrospun scaffold can be used to increase the penetration of cells into the matrix afforded by the fiber arrays. This study examines the hypothesis generated in pilot studies that cell infiltration into an electrospun scaffold is mediated by an initial phase of passive sieving followed by an active phase of cell migration. Results from this study are used to better define factors that limit cell seeding processes that are used in attempts to generate densely populated electrospun scaffolds.

Improved Infiltration of Human Dermal Fibroblasts into Novel Porous Electrospun Scaffolds

Casey P. Grey[1] and David G. Simpson[2]

[1]Department of Biomedical Engineering and [2]Department of Anatomy and Neurobiology

ABSTRACT

When cells are seeded onto electrospun tissue engineering scaffolds, the traditional line of thought has been that subsequent infiltration and occupation of the scaffold is due to the active migration of the cells from the surface into the construct. Our preliminary observations have suggested that infiltration is mediated by an initial passive phase in which cells simply sieve between the fibers of a scaffold followed by a secondary phase of infiltration driven by the active cellular migration (e.g. locomotion). The passive phase is largely governed by the physical properties of a scaffold and appears to take place during the early hours after cell seeding. Predictably, interventions that increase scaffold porosity and or interfiber spacing should serve to prolong this passive process and increase cell infiltration. In this study we examine how scaffold porosity impacts the extent to which cells infiltrate into the matrix afforded by the fibers of the constructs.

5.1 INTRODUCTION

A major goal of the tissue engineering research enterprise is to develop highly densely populated scaffolds for tissue replacement therapy. This has represented a daunting objective to achieve. In vitro there appears to be little impetus for cells to actively migrate into and populate the 3D space afforded by many different types of tissue engineering scaffolds. Most research directed at increasing the penetration of cells into electrospun scaffolds has been focused on increasing scaffold porosity.[5,139,140] Dense fiber arrays of most electrospun scaffolds appear to inhibit cell penetration and, at least from a observational perspective, in our laboratory cells appear less likely to migrate through the z-axis of a scaffold (bridging fibers) than along the x-y plane (traveling along fibers). Fibers of an electrospun matrix are deposited in a sequential fashion in a layered manner resulting in a fibrous mat predominantly oriented in the x-y plane. This layering does not appear to signal cells to enter from the free surface and into the spaces present between the fibers along the z-axis.

Air impedance electrospinning is a modification of the basic process of electrospinning that uses a perforated mandrel as a target to collect forming fibers.[5] Air is forced through the pores during spinning to suppress the accumulation fibers in the vicinity of the air flow. This results in the formation of a scaffold with regionally defined domains of increased porosity (i.e. less fiber packing, often referred to as “macropores”), these domains of increased porosity are readily visible upon microscopic examination (see Figure 4.6). The extent to which these structures vary across the axis of a scaffold has not been explored and it is unclear how even the air flow might be through all of the ports present in a perforated mandrel. Uneven air flow will result in the

production of scaffolds that exhibit heterogeneous domains of porosity, an unfavorable characteristics that complicates the interpretation of culture experiments designed to study cell penetration into these regions. Under uneven airflow conditions adjacent pores can be expected to have very different structural properties. In this first part of this study we model the air flow properties of an air impedance mandrel to validate the technique as well as the scaffolds produced in studying how regional variations in porosity impacts cell infiltration into these constructs.

5.2 MATERIALS AND METHODS

Electrospinning

All reagents Sigma unless otherwise noted. Polycaprolactone (PCL: 65,000 M.W.), was suspended in trifluoroethanol (TFE; 250 mg/mL). Electrospinning syringes were capped with blunt-tipped 18-gauge needles and placed into a syringe driver (Fisher Scientific) set to deliver 5 ml of the electrospinning solution into a 17 kV-19 kV static electric field at a rate of 9 mL/hr across a 20 cm gap.[9] A perforated cylindrical metal mandrel was used as a ground target (functional length = 11.75 cm, mandrel diameter = 6.33 mm, pore diameter = 0.75 mm spaced laterally 2 mm and vertically 1.5 mm).[5,9] In selected experiments a solid mandrel exhibiting the same dimensional characteristics perforated mandrel was used as a ground target. Scaffolds were collected with and without air flow passing through the perforations (0kPa (static controls), 100kPa, and 300kPa.) [5]. The mandrel was rotated (700 rpm) and translated (4 cm/s over a 12 cm distance) during electrospinning to promote the formation of a scaffold with a uniform thickness [9] These conditions result in the deposition of random fiber arrays on the surface of the target. Scaffoldswere cut longitudinally to remove them from the mandrel. Scaffolds, once dried to remove any residual solvent, were stored under desiccation until further processing.

Gradient electrospinning

Two-chambered electrospinning reservoirs were prepared by placing 2.5 mL of 150 mg/mL PCL into a 5 mL syringe. The intermediate disk ("mixing port"), created by piercing the rubber cap of a syringe plunger with an indwelling, 5 mm segment of an 18-gauge needle.[9] This intermediate disk is then positioned on top of the 150 mg/mL PCL solution. Next the syringe is filled with 2.5

mL of 250 mg/mL PCL. The plunger is then installed into the syringe. At the onset of electrospinning, the mixing port remains stationary until the primary syringe plunger comes into contact with it, at which point it is driven down the length of the syringe. By remaining stationary the mixing port allows the controlled mixing of solutions, thus creating the smooth gradient of polymer (and thus a gradient of fibers in the Z direction which vary in average cross sectional diameter). Laminated scaffolds were produced by sequentially spinning 2.5 mL of 150 mg/mL PCL solution onto a mandrel followed by 2.5 mL of 250 mg/mL PCL solution. This results in a scaffold with an abrupt change in fiber diameters at the interface where fibers fabricated with the low concentration PCL starting solution ends and the fibers fabricated with the high concentration of PCL begin.

Computational Fluid Dynamics (CFD)

All computer drawings and meshes were generated using Gambit (Version 2.4). Fluid model simulations were performed in Fluent (Version 12.0) using either 1,000 iterations or until convergence was achieved. Graphical representation of the fluid models was visualized using Tecplot.

Cell Culture

Human dermal fibroblasts (hDF, Cascade Biologics C-013-5C) were cultured in DMEM-F12 (Gibco) supplemented with 10% fetal bovine serum (FBS, Hyclone) and 1% penicillin/streptomycin (P/S, Invitrogen). Electrospun samples were sanitized in 70% ethanol for 30 minutes, rinsed 2x in phosphate buffer solution (PBS) and 1x in culture media. Cells were seeded at a concentration of 25,000 cells onto 6 mm diameter circular PCL scaffolds prepared

with a punch die and cultured in an incubator set to 37°C and 5% CO_2. A cloning ring was used to confine cells to the dorsal surfaces of the scaffolds during the early stages of culture. Media was change every 3 days. Scaffolds were fixed in 10% glutaraldehyde for 10 min and rinsed 2x in PBS and stored in a fresh aliquot of PBS at 4°C prior to processing. For cross-sections in each scaffold only three sections were collected between 2500 and 3500 µm (the middle of the scaffold with the largest cross-section surface area) and analyzed as representative samples. In frontal sectioning all samples containing cells were kept and analyzed. All cultures were stained with 4',6-diamidino-2-phenylindole (DAPI) to visualize the nuclei for cell counting experiments.

Cryosectioning

Frontal and conventional cross-sectional cryosectioning were used to process scaffolds. Cross-linked samples were incubated in 30% sucrose prepared in PBS for three days at 4°C and embedded for cryosectioning. In all experiments 50 µm samples were used for microscopic analysis. Cut samples were then placed immediately into PBS and stored at 4°C until further processing.

Image Analysis

All images were captured on a Nikon TE300 microscope equipped with a 10x objective and a DXM 1200 digital camera at a resolution of 1280x1024. Brightfield images were overlaid with fluorescence images (DAPI) using Adobe Photoshop CS4, and combined using the photomerge function.

Statistics

All data sets screened using ANOVA. The Holm-Sidak method was used for pairwise comparisons. P values as provided. Graphical depictions represent +/- the standard error unless otherwise noted.

5.3 RESULTS

Air Impedance Electrospinning – Modeling Airflow through a Porous Mandrel

Air impedance electrospinning uses a perforated target mandrel that has air forced through the perforations during electrospinning. This air flow partially inhibits the accumulation of fibers in the regions of the pore, increasing porosity in a regional manner coincident with the pores. The objective is to identify conditions in which the exiting air flow rates along equal along the entire length of the target mandrel. Computational Fluid Dynamics (CFD) modeling was used to characterize and validate air flow patterns. These experiments indicate that uneven airflow is present (Figure 5.1), at a maximum air flow (100kPa inlet pressure) the differences in outlet velocity are sufficiently divergent that the variations can be detected by touch along the length of the mandrel. These data indicate that design modifications are necessary in order to use this system to fabricate homogenous scaffolds exhibiting systematic, periodic and predictable variations in porosity. Figure 5.1 depicts the calculated air velocities with respect to pore location at an inlet pressure of 100kPa. The color and length of the vectors depicting flow are correlated to air velocity. Especially notable is the distal velocity bulge that represents the increased air velocities present at the pores located on the distal end of the mandrel.

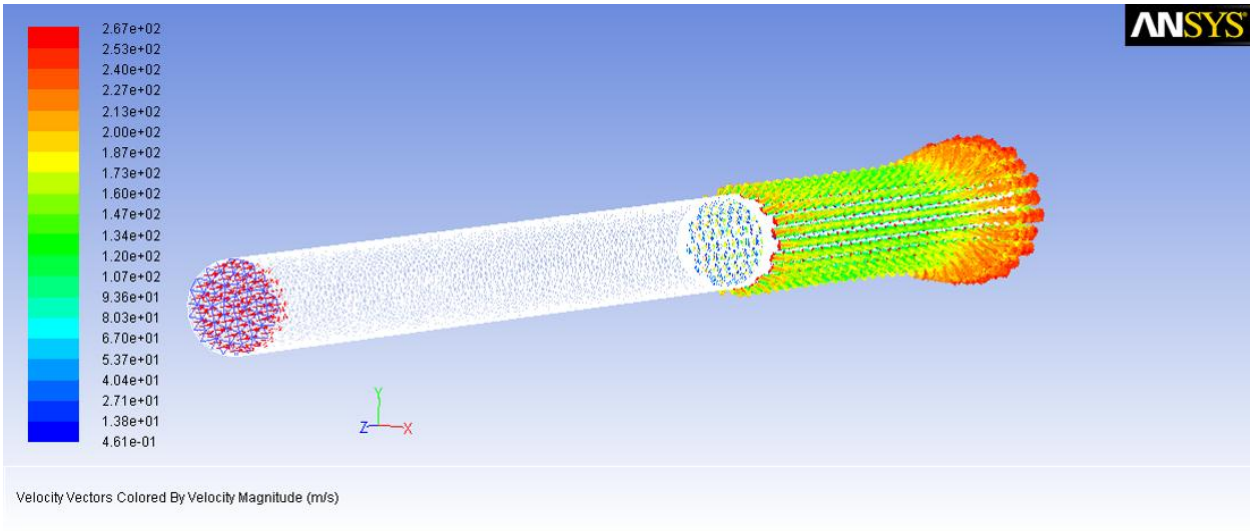

Figure 5.1. *Computational Fluid Dynamics (CFD) model of the air impedance mandrel used in this study. When air is forced through the mandrel it exits the pores in a nonlinear fashion with the highest air velocities seen at the most distal pores. At 100kPa inlet pressure the mass flow rate (MFR) of air exiting the last pore (right side in figure) can be as much as 215% higher than the MFR of air exiting the first pore (this is seen in the longest, 120 pore length design).*

Attempts to even out flow by introducing various internal geometries and baffles into the internal aspect of the perforated mandrel were largely unsuccessful. The most effective modification to the mandrel design was simply to reduce the total number of pores present by sealing off sections of the mandrel. With this approach we were able to reduce the MFR differential (most proximal pore vs. most distal pore) from 215% in the 120 pore model down to 99% by reducing the porous region to 60 pores. A further reduction to 20% was observed in this metric of flow differentiation when the porous region was regulated to just 30 pores (i.e. 20% difference in air flow most proximal to most distal). While these results show that differences in air flow at the proximal and distal ends of the mandrel can be reduced, there does not appear to be an obvious and simple design modification that can be implemented to even out the flow rates through all pores in a full

length mandrel. Given these results we chose to limit the analysis to scaffold materials deposited onto the proximal pore regions of the perforated mandrel that exhibit the most similar rates of air flow.

To justify this approach, we compared the mass flow rates (kg/s) of air flowing through each pore down the length of the mandrel. In this analysis the most proximal pores (pores 1-41) exhibited air flow rates that were not significantly different and, as a result, this region represents a consistent environment for depositing electrospun fibers. The remaining more distal pores (pores 42-52) exhibited significantly higher and more varied air flow rates. In a fabricated scaffold increased air flow translates into larger interfiber distances and increased scaffold porosity. In this model, scaffold material collected on regions associated with the proximal pores will have less porosity than scaffold material collected on the distal pores, resulting in construct with varying porosity (Figure 5.2 for data and p-values). The flow rates in these distal pores also varied so abruptly (pore 52 displayed significantly higher flow rates compared to pores as close as pore 48, p=.009) that scaffold samples taken directly adjacent to each other would theoretically have very different properties. Scaffolds produced under these varying flow rates would greatly complicate the analysis of the biological properties of the scaffold. For subsequent experimentation all scaffolds were fabricated and recovered from the mandrel containing the most proximal set of pores.

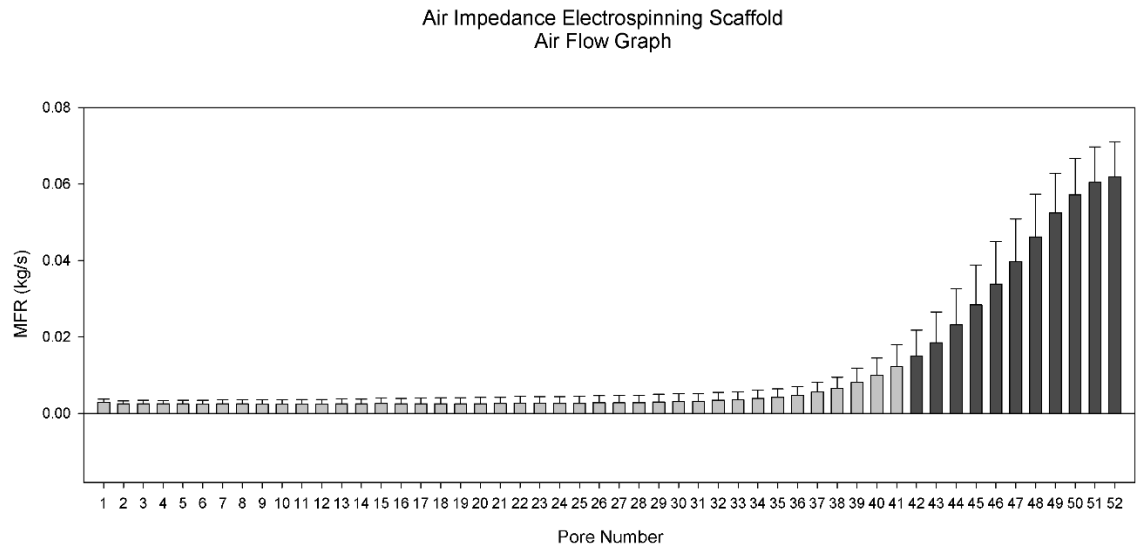

Figure 5.2. *Mass flow rates (kg/s) were obtained from pores down the length of the air impedance mandrel model (error bars represent standard error). Pore 1 represents the pore closest to the air source (most proximal pore, on the valve side) and pore 52 represents the pore closest to the closed end of the mandrel (most distal pore). Using pore 1 as a control, mass flow rates from pore 42 through 52 (the last pore) were found to be significantly higher (see dark grey) than mass flow rates in each pores 1-41 (light grey). P-values for pores 43 through 52 were <0.001 while pore 42 exhibited a p-value of 0.021. Similar results were found using an all pair-wise approach, with significant differences from pore 1 starting at pore 43 (p=.009) and continuing through pore 52 (p<.001 for pores 44-52).*

Cell Culture Experiments-conventional cross sectional analysis

Cells were seeded and cultured for varying periods of time on control scaffolds fabricated on a solid mandrel and experimental air impedance scaffolds to determine the baseline proliferative properties of the cultures (Figure 5.3). In these experiments we analyzed the cell data from

several angles. First we performed a generic analysis combining all experimental groups depending on the number of days they spent in culture. By analyzing the cell counts we can confirm that, generally, the cell culture matured as expected and cell population increased as a function of culture time ($p<.001$ comparing Day 14 vs Day 1 and comparing Day 7 vs Day 1, $p=.002$ comparing Day 14 vs Day 7).

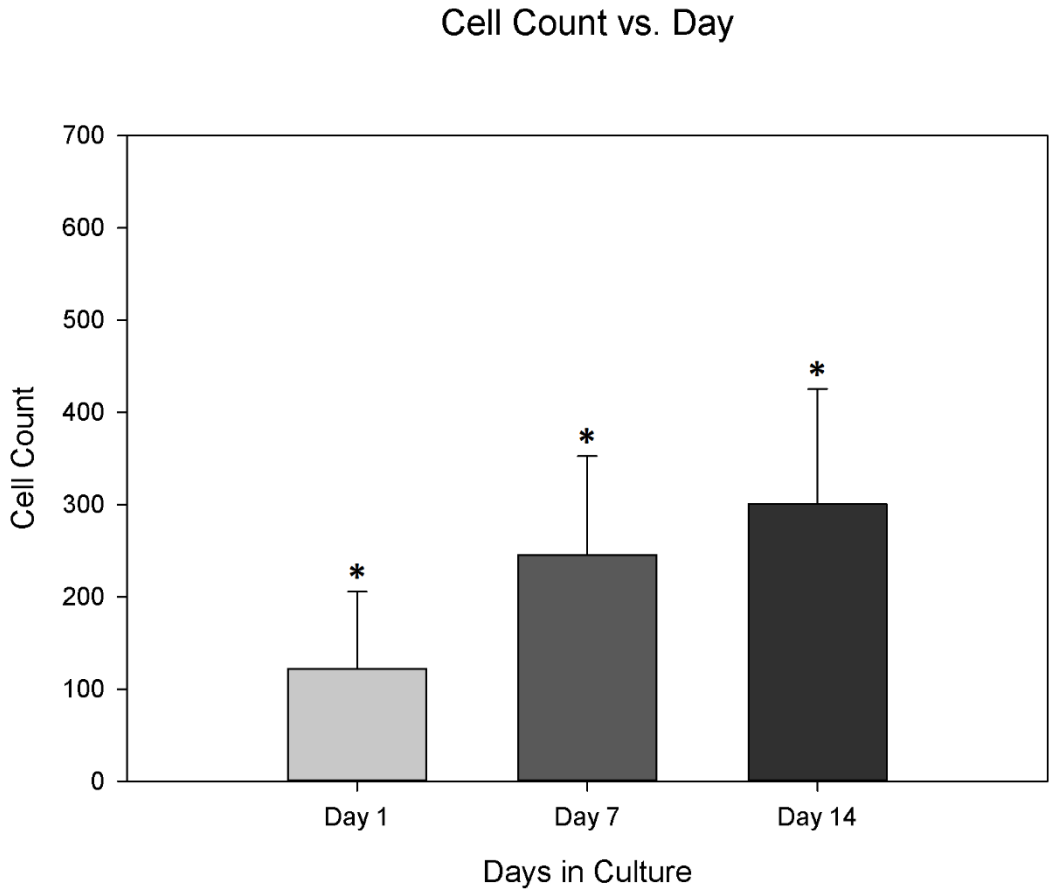

Figure 5.3. *Cell infiltration experiments (cross-sectional data) indicated that the cell population on scaffolds significantly increases with extended culture time. Cross-sectional data from 150 mg/mL and 250 mg/mL scaffolds (n=72) was obtained and all cells manually counted (y-axis), error bars are standard error.. For each scaffold, three representative sections were taken between depths of 2.5mm and 3.5mm. Cell population at each time point was found to be*

*significantly different with only slight variations in p-value (significance denoted by *). Days 7 and 14 were both found to be significantly different from Day 1 ($p<.001$) and Days 7 and 14 were found to be significantly different from each other ($p=.002$).*

If cells can readily penetrate one scaffold design versus another scaffold design, the scaffold that supports increased cell penetration effectively has more surface area available for cells to occupy. An extension of this hypothesis would be to predict that scaffolds which support greater cell penetration, due to increased porosity, might be expected to accumulate more cells through proliferation over time. From previous published work conventional electrospun scaffolds produced with the 250mg/mL starting solution should have the greatest porosity.[9] Further, scaffolds produced as gradients are mechanically coupled across the z-axis, and we have predicted this mechanical coupling would lead to greater cell infiltration. The predictions that scaffolds with higher porosity and or scaffolds that support greater penetration should accumulate more cells were not supported by experimentation (Figure 5.4). As in Figure 5.3, results came from total cell counts on all mandrels (solid and air impedance) and grouped by PCL concentration. 150 mg/mL scaffolds, 250 mg/mL scaffolds, 150-250 laminated scaffolds (seeded on the 250 mg/mL side), and gradient scaffolds (seeded on the 250 mg/mL side) were compared regardless of mandrel. In this analysis we found no significant differences across the different scaffold designs (Figure 5.4).

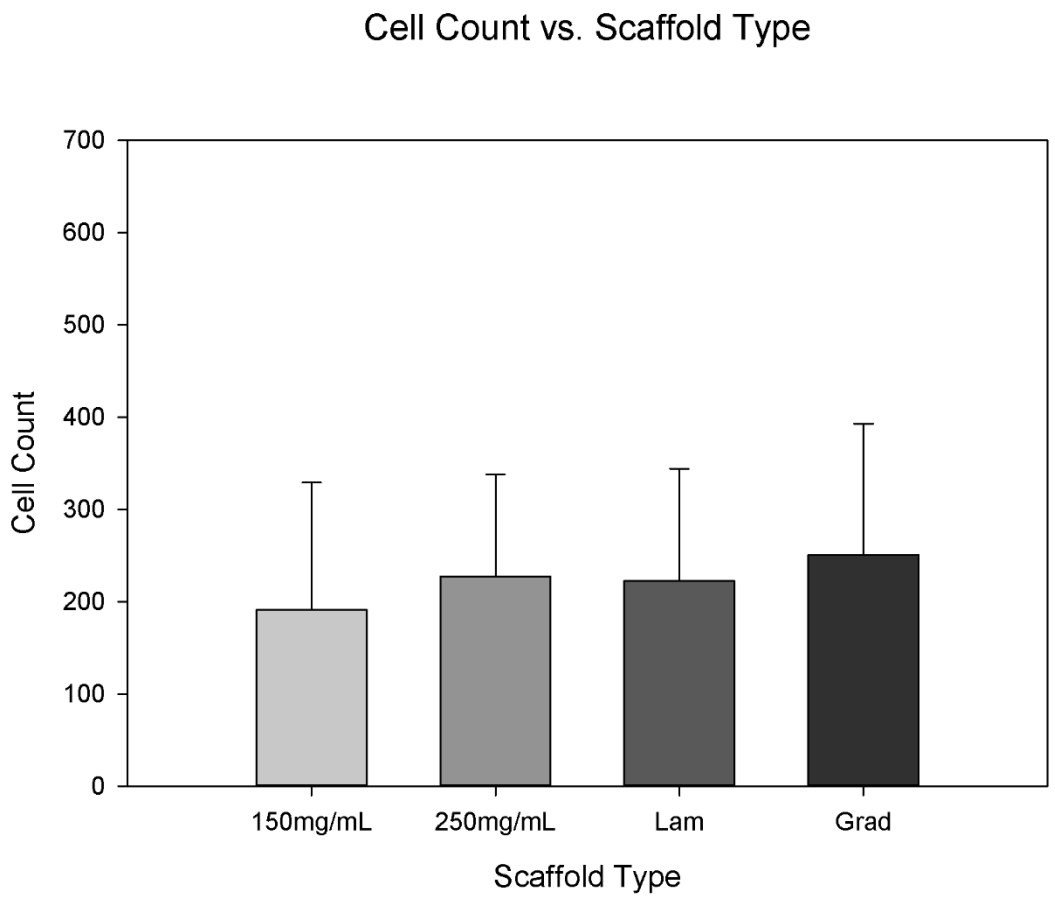

Figure 5.4. *Comparing cellular occupation (cell count in samples) between PCL scaffolds composed of different concentrations and concentration profiles (laminated/gradient) yielded no significant differences between the test groups across all time points to establish whether scaffold-specific trends emerged (n=54, error bars are standard error). For each scaffold, three representative sections were taken between depths of 2.5mm and 3.5mm. Lam=laminated scaffold, Grad=continuous gradient scaffold.*

To further explore the results of the proliferation experiments we examined the degree to which different scaffold designs supported general cell infiltration and occupation via total cell count from cross-sections (Figure 5.5). We compared the performance of A) scaffolds prepared on

solid mandrels and prepared with a uniform coating of fibers, B) scaffolds prepared on mandrels with ports and no air flow across the pores and, C) scaffolds prepared on mandrels with ports and air flow through the pores (scaffolds exhibiting localized areas of increased porosity). In this analysis we differentiated scaffolds only by the mandrel which they were fabricated on. From this analysis we found that both perforated mandrels (air and no air) exhibited had increased cell populations versus the solid mandrel ($p<.001$ comparing perforated mandrels with air flow vs solid mandrels and $p=.001$ comparing perforated mandrels with no air flow vs solid mandrels). There were no significant differences found between the perforated mandrel with air flow compared to the perforated mandrel without air flow.

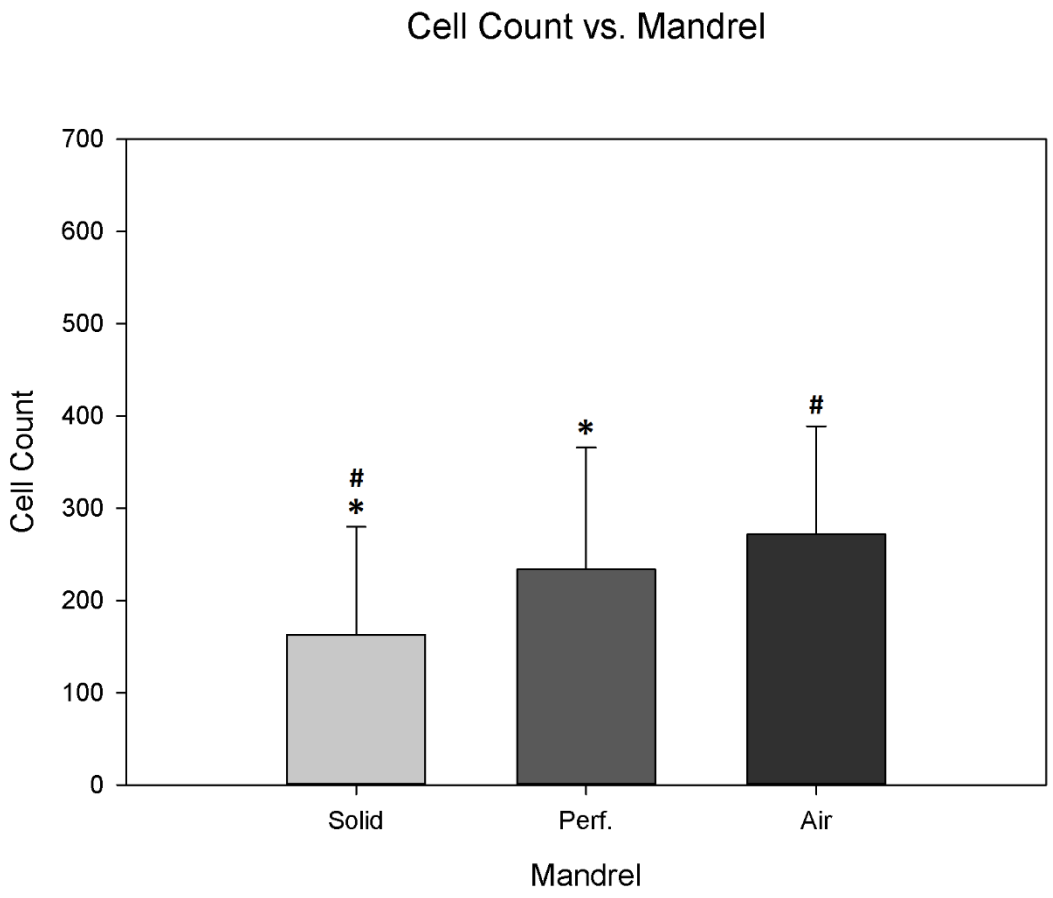

Figure 5.5. *Maximal cell occupation as a function of scaffold design (n=72, error bars are standard error). Taking another approach to cellular occupation with scaffolds the total cell count was taken for scaffolds depending on scaffold type (solid, perforated-no air, and perforated with air). For each scaffold, three representative sections were taken between depths of 2.5mm and 3.5mm. Perforated scaffolds fabricated with ("Air") and without air flow ("Perf") accumulated more cells compared to scaffolds produced on solid mandrels ($p=.001$ and $p<.001$, respectively). No differences were detected between the scaffold produced on the perforated mandrels prepared with or without air flow.*

Cell Culture Experiment 2 – Frontal Section Infiltration Depth Analysis

Preliminary cell culture experiments used conventional cross sectional analysis to evaluate the distribution and number of cells present in the different scaffolds designs. Because preliminary experiments showed only significant cell population differences between scaffolds fabricated on different mandrels the next generation of culture experiments eliminated multi-layered scaffolds and focused on scaffolds composed of single concentrations of PCL (either 150 mg/mL or 250 mg/mL) but fabricated on different mandrels (solid and air impedance with/without air flow). One clear limitation to cross-sectional analyses is that the representative section method largely makes an assumption that cells are more or less uniformly seeded and distributed on the scaffolds, collecting data for the entire scaffold is not feasible. To examine this assumption, frontal sections were taken of various scaffolds. This method effectively cuts the scaffolds into layers, and when done properly, results in complete sections of the entire scaffold that are taken in parallel, rather than perpendicular to the seeding surface. One consequence of this approach is that cell counting data from the different sections is effectively binned into specific depths. The

preliminary experiments in which conventional cross sectional analysis was conducted suggested that scaffolds deposited onto mandrel with perforations support more infiltration and the accumulation of more cells. We extended these preliminary experiments to objectively measure the extent of cell penetration using more frontal sections, a method that provides less ambiguous data than conventional cross sectional analysis due to the binning effect of physically cutting the sections. Figure 5.6 summarizes the results of the initial second generation experiments in which cells were seeded onto 150 mg/mL and 250 mg/mL scaffolds fabricated on either solid or air impedance mandrels. Similar in design to Figure 5.3 this analysis confirmed that the cell culture matured as expected by increasing total cell number as a function of culture time.

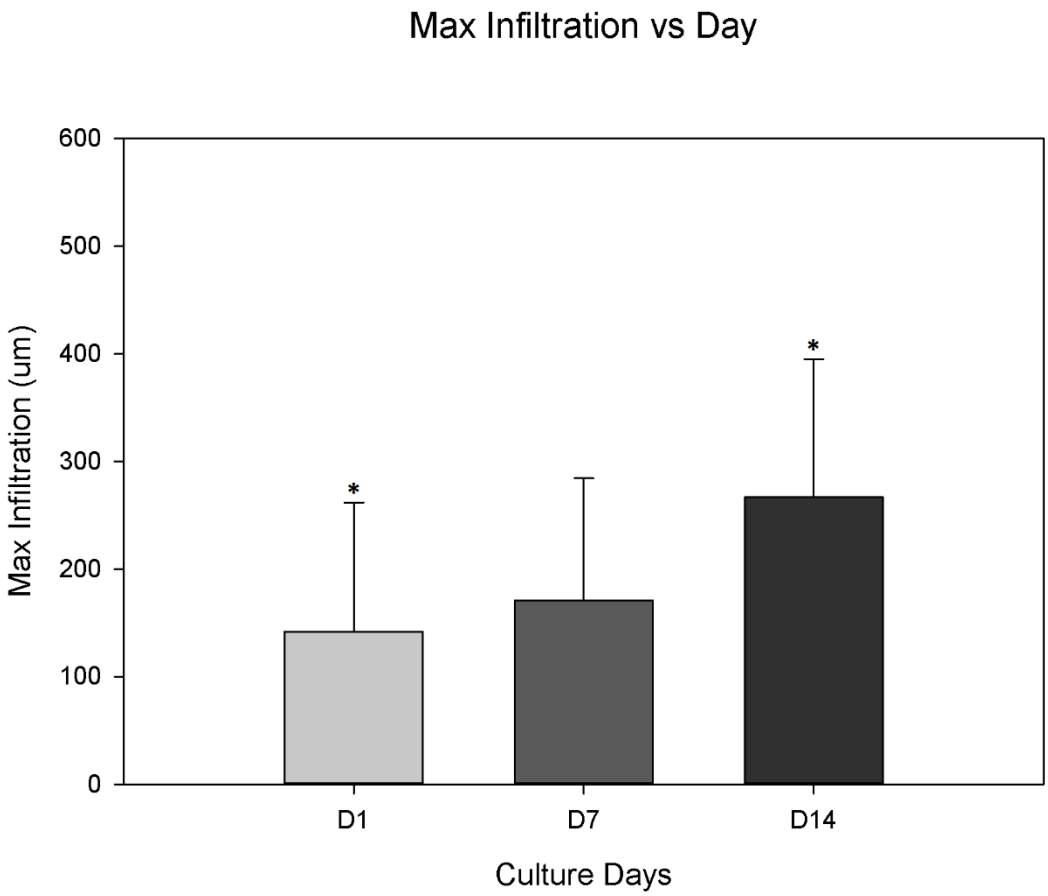

Figure 5.6. *Cells seeded on 150 mg/mL and 250 mg/mL scaffolds fabricated on either solid or air impedance mandrels (with and without air) differentiated only by culture time (n=12, error bars are standard error). Scaffolds were processed by frontal sectioning and cells were counted in each section to determine the number of cells throughout the scaffold. The extent of cell penetration increased as a function of time from day 1 to day 14 (p=.048).*

Analyzing the frontal section data to focus on the maximum depth of cell infiltration as a function of scaffolds produced on different types of mandrels at different time points revealed a clear trend for increased penetration on all scaffolds as a function of time (Figure 5.7). In addition, and surprisingly, scaffolds produced on perforated mandrels qualitatively exhibited more cells at deeper depths than scaffolds produced on a solid mandrel at day 1. A summary of the average maximum depth of cell infiltration/penetration for all scaffolds produced on solid mandrels and perforated mandrels with and without air flow is summarized in Figure 5.8. This data demonstrates that cell penetration appears to be greater in scaffolds produced on the perforated mandrels ***independently of air flow.*** Samples produced on the perforated mandrels in the absence of air flow would ordinarily be expected to perform more like a scaffold produced on a solid mandrel, in the absence of air flow the two theoretically should be very similar, but they are not. The data would indirectly suggest that scaffolds produced on perforated mandrels in the absence of air flow are essentially identical to those produced using flow; one likely explanation for the hypothesized increased porosity in the absence of air flow lies in electric edge effects induced by the pores. Charge accumulation along the edges of the pores may serve to disrupt fiber deposition and thereby increasing porosity in those domains. Given these circumstances scaffolds produced on perforated mandrels that exhibit regions of increased porosity (either from

edge or air flow or both) could simply be more effective at capturing cells during the initial cell seeding interval. The increased capture rate could equate into a higher probability that cells will penetrate the scaffolds. While this explanation is possible, it seems unlikely that this can solely account for the presence of cells so deep in some of these scaffolds at early time points. Rates of cell migration would have to be sustained and astronomical to account for the extent to which cells seem to penetrate some scaffolds. High rates of migration, given that cells attach and spread so slowly on most electrospun scaffolds, especially scaffolds prepared from synthetic materials, would seem to be an untenable explanation. The calculated velocity of penetration drops precipitous as a function of time in culture (Figure 5.9).

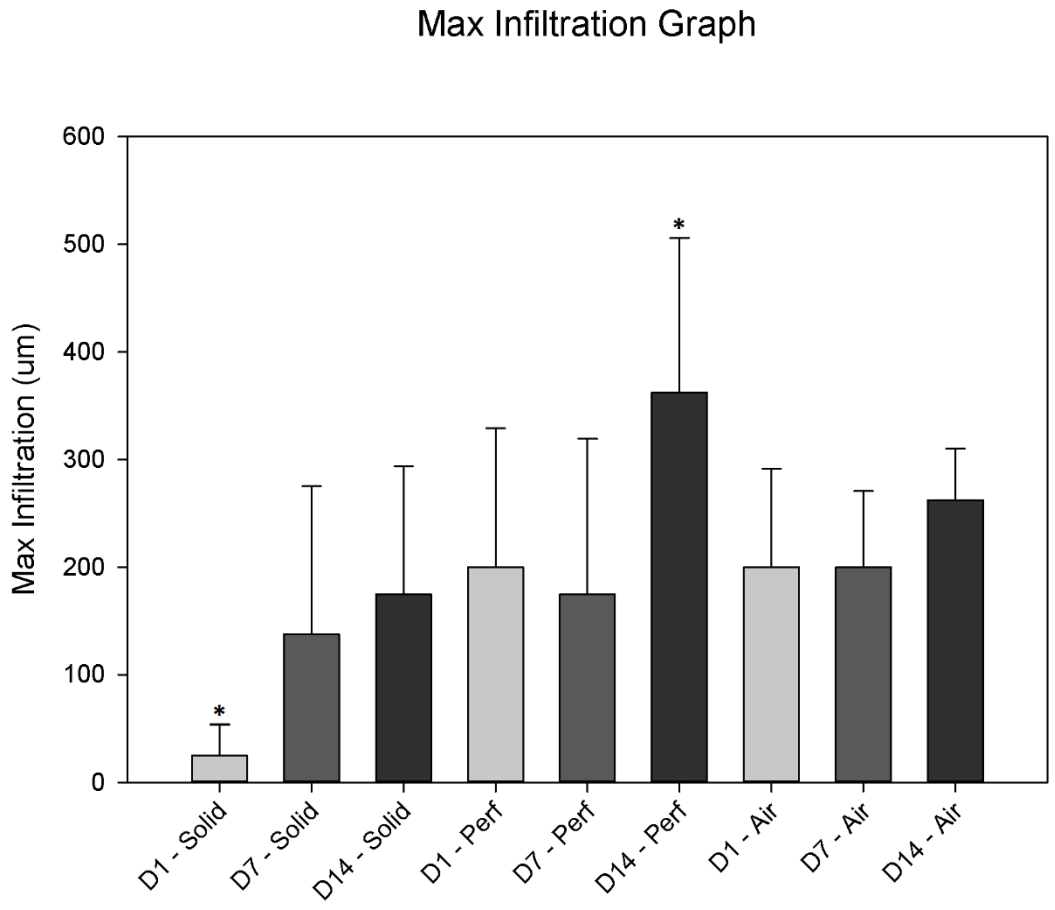

Figure 5.7. *Comparison of maximum cellular infiltration, as judged by the last frontal section containing any cells, on different scaffold types and throughout the three different time points (n=3, error bars are standard error). The only significant difference across the treatment sets was found to be between day 14 "perf" and day 1 "solid" (p=.006), a comparison that, by itself yields little value, but the general trend of increasing maximum infiltration between days and mandrel types deserves closer examination. Figure 5.8 attempts to extract useful information from maximum infiltration data by analyzing it from a different perspective.*

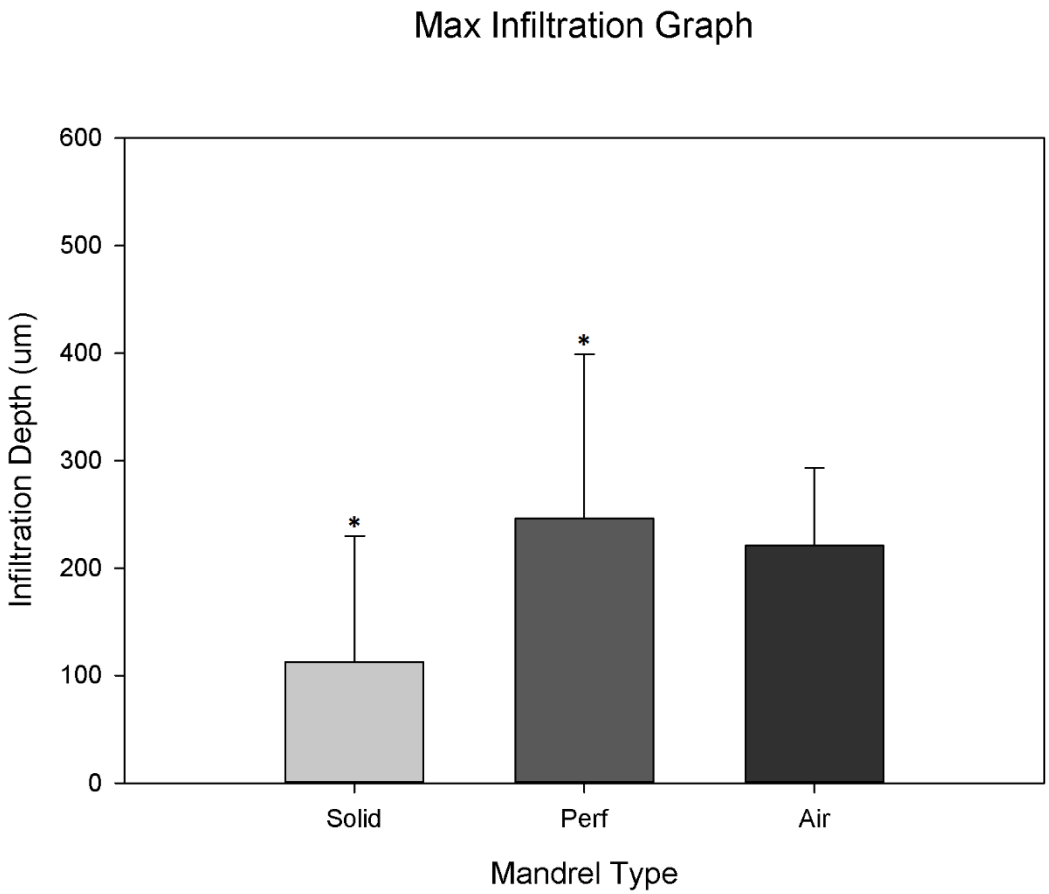

Figure 5.8. *Maximum infiltration depth vs. mandrel type. In this figure all infiltration data was differentiated only by mandrel type to elucidate any infiltration differences (n=12, error bars are standard error). Air impedance mandrels, both with and without air, are characterized by the presence of localized areas of increased porosity surrounded by domains exhibiting a higher density of fibers. Changes in porosity in scaffolds produced on the perforated mandrel in the absence of air flow can be attributed to edge effects of the electric charge on the grounded mandrel. In series of experiments scaffolds produced on perforated mandrels without forced air exhibited significantly increased cellular infiltration depths compared to conventional scaffolds fabricated on solid mandrels (p=.028).*

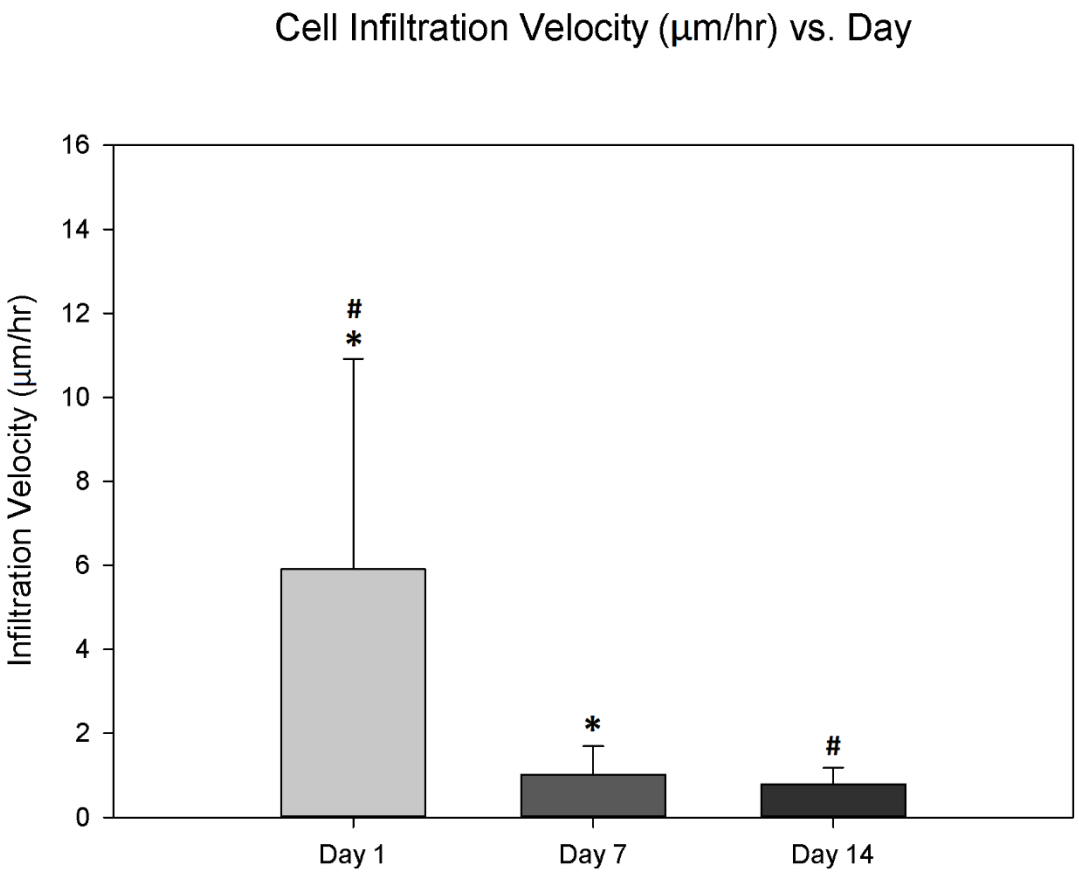

Figure 5.9. *Cell infiltration velocity vs. day. Infiltration data was differentiated only by culture day in this analysis and subsequent infiltration velocities were calculated by dividing the infiltration distance by culture time (n=12, error bars are standard error). Projected rates of cell migration decrease as a function of time in culture. The calculated rate of migration from this data indicates that the velocity of penetration is significantly greater in Day 1 compared to both Days 7 and 14 (p<.001).*

5.4 DISCUSSION

The goal of this research was to explore parameters that might be exploited to improve cell penetration into electrospun scaffolds. While this unique class of nanomaterials has great promise, to date, efforts to fabricate densely populated tissues in vitro have been largely unsuccessful. Generally these scaffolds are believed to be too dense with inadequate open spaces for migration, and perhaps, lacking in pro-migratory signals to induce cells to enter the matrix afforded by the fibers. The precise milieu of migratory signals is not fully understood and trying to recreate it in a consistent fashion is a difficult objective to achieve. Under base line conditions cells penetrate into most electrospun scaffolds at very slow rates, if at all. Once they pass from the free surface and into the interfiber domains there does not appear to be any driving force to induce further migration. It is certainly possible to identify and use soluble pro-migratory signals to induce cells to penetrate into scaffolds such as PDGF or other growth factors, however, the utility of this approach is limited to select cell types that respond to a given growth factor.

In this study we elected to explore an alternative approach and examined how modulating scaffold structure might be exploited to increase the potential to populate electrospun scaffolds. We explored two alternative designs, initially a large group of scaffolds composed of solid and multi-layered scaffolds. Data indicated that changes in mandrel type drove the most significant cell population increases, therefore the second round of cell culture experiments involved single-layer scaffolds and focused on differences between scaffolds fabricated on different mandrels. Scaffolds produced on perforated mandrels with and without air flow performed essentially identically and, as noted, we believe electric edge effects induced by the pores explain this result.

The fiber gradient scaffolds were designed to induce cell penetration by producing a mechanical gradient across the z-axis of the structure. We believed that by coupling the fiber arrays along the z direction and seeding cells on large scale fibers that gradually underwent a decrease in size (as a function distance in the z direction) that cells would be more likely to penetrate the construct. Evidence from this study suggests this hypothesis was not valid, at least with regards to our cell culture model and these scaffolds did not support penetration to any great extent over the controls. The potential for gradients in fiber diameter to induce unique cellular responses is still viable, however, because the cells in this study did not penetrate far enough into the scaffold (due to other limiting factors) to be introduced into the gradient region. From a fabrication and performance standpoint scaffolds produced on perforated mandrels without air flow supported the most extensive infiltration of cells. Not using air flow greatly simplifies scaffold fabrication, no air flow is easier to manage than air flow and should result in a far more uniform scaffold because you do not have to manage continuously varying air flow rates along the axis of the mandrel (e.g. Figures 5.1 and 5.2) .

Air impedance electrospinning represents a compromise between increasing scaffold porosity and maintaining scaffold strength by creating a patchwork of locally increased porosity surrounded by areas of more densely packed fibers for reinforcement. This consideration, while not critical in cell culture experiment, is of critical importance when a construct is to be used for reconstruction therapy. The scaffolds produced by this technique are designed to promote increased cell penetration into the macropore regions (imagine cells occupying a cylindrical pattern through the z-axis of the scaffold where the fibers are less dense). In theory, once the cells have sieved into these regions they should migrate laterally between the fiber arrays to fully

occupy the scaffold. Qualitative observations from our laboratory have long suggested that cells are more likely to migrate along the axis of the fibers rather than across the fibers. While this idea is plausible, our research indicates that migration into electrospun scaffolds, regardless of the design we examined, is not nearly robust enough to fully populate a scaffold in a reasonable amount of time. Maximum infiltration depths after 14 days in culture rarely exceeded 300 µm and never involved a substantial number of cells.

The perforated mandrels outperformed the solid mandrels and the gradient scaffolds in both overall cell population and maximum depth of cell infiltration and did so without requiring the additional variable of air flow in the mandrel. McClure et. al. developed air impedance electrospinning and showed that it generally increased the depth of cellular penetration into electrospun scaffolds.[5] Data in support of this model of cell penetration was largely based on cross sectional analysis of the scaffolds (Figure 5.10), unfortunately, definitively identifying the pores induced by the perforated mandrel in this type of analysis is difficult to achieve at best. In turn this makes it difficult to determine if cells preferentially penetrate the areas of increased porosity or whether some other aspect of the scaffold positively affected infiltration. Our approach in using frontal sections substantially confirms the critical role that the macropores play in promoting increased cell penetration into scaffolds produced on perforated mandrels (Figure 5.11).

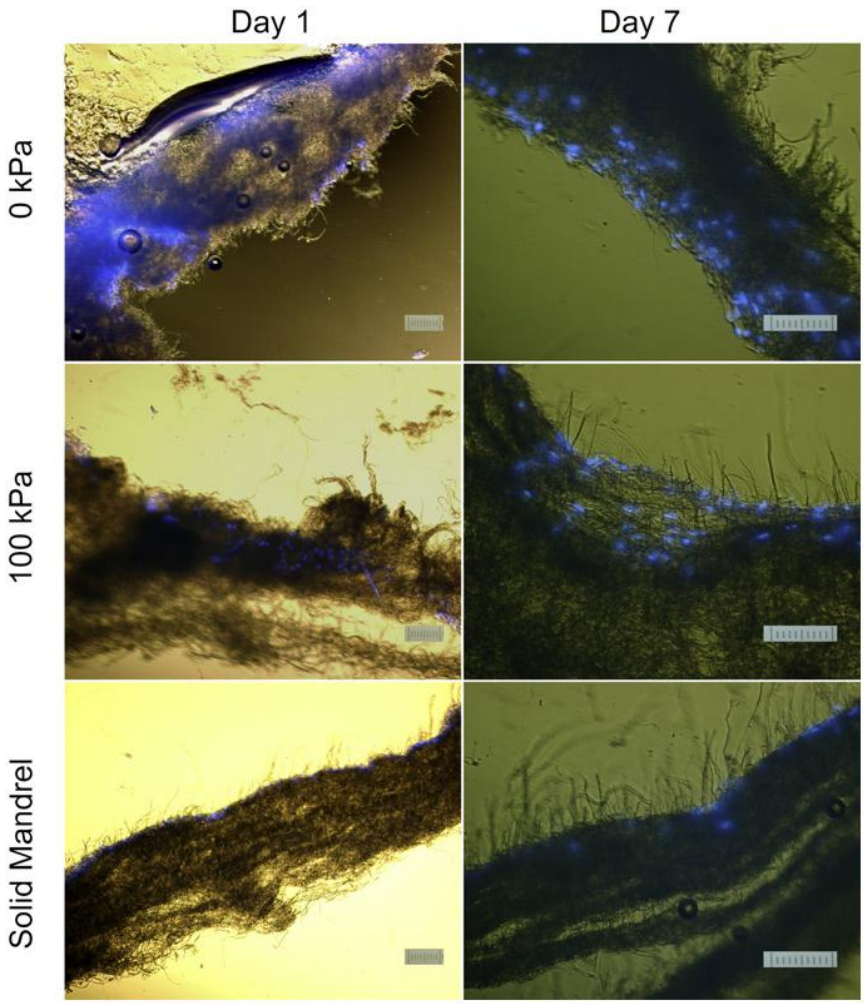

Figure 5.10. *This excerpt from McClure et.al. shows increased cell penetration into electrospun scaffolds fabricated on perforated mandrels using air flow compared to those fabricated on solid mandrels (scale bar = 100µm).[5] The macro pores are often damaged during processing and evaluating the precise locations of the pores and the relationship of these structures to cells is difficult to judge. These represent conventional cross sections taken from frozen sections and stained with DAPI to reveal fibroblastic nuclei.*

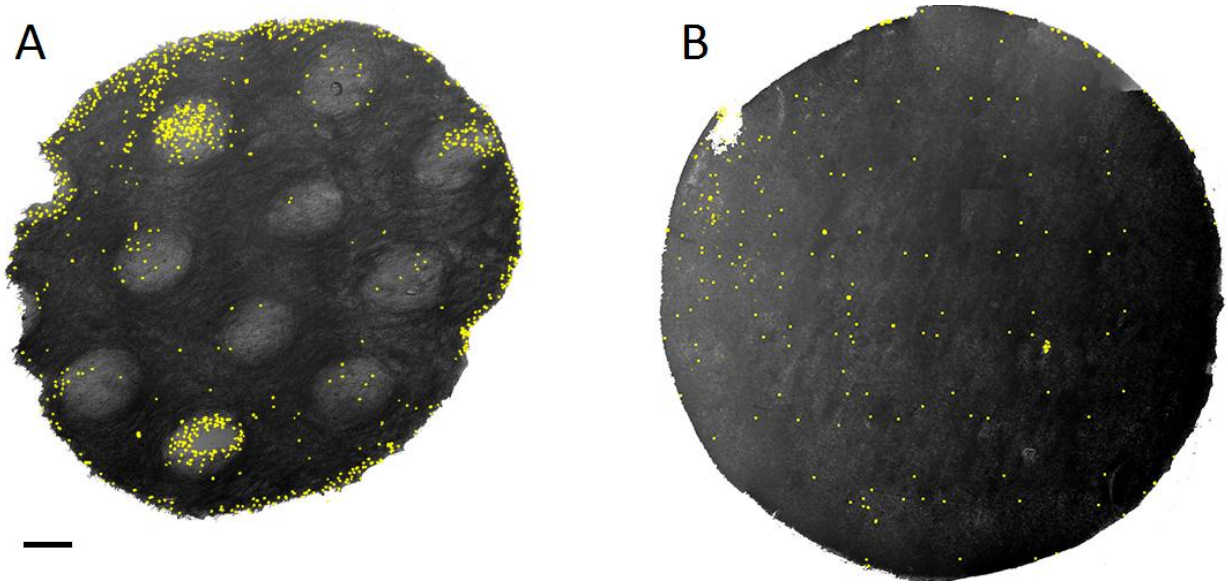

Figure 5.11. *(A) 150 mg/mL PCL electrospun scaffold fabricated on a perforated mandrel with no air flow (0kPa) and (B) 150 mg/mL PCL electrospun scaffold fabricated on a solid mandrel. Both frontal sections represent a depth of 50 µm into each scaffold. Cells are shown were stained with DAPI (false colored yellow) and can be seen aggregating in the macropore regions of the air impedance scaffold compared to the scaffold produced without the macropores. Scale bar represents 500µm.*

On day 1, the average maximal infiltration depth observed in all scaffolds was 142 µm after just 24 hours. This equates into and average infiltration velocity of approximately 6 µm/hr during the first 24 hours of culture. Given the barriers to migration present along the z-axis of an electrospun scaffold, the extended period of time it takes cells to adhere and spread out on a scaffold composed of synthetic fibers and the observation that velocity appears to precipitous drop at later time points in culture this would seem to imply that active migration cannot account for this result. Under the influence of an electric field the fastest rates of migration that are routinely achieved are about 15 µm/hr on a flat surface and under the influence of an electric

field.[141] Given these observations we suggest that the rate of cell penetration during the early stages of culture must take place through mechanisms independent of cell mediated migration events.

5.5 CONCLUSION

In this study we utilized a new sectioning technique to examine the effects of increased scaffold porosity on cellular infiltration into electrospun scaffolds. By performing these experiments on air impedance scaffolds we were able to control for all conditions excepting scaffold porosity. Air impedance scaffolds also have the added benefit that the locations of increased scaffold porosity are easily located, appearing as circles with obvious changes in fibrous makeup (macropores). We confirmed that air impedance scaffolds improve cellular infiltration into electrospun scaffolds and observed that this infiltration was predominantly in the regions of increased porosity (the macropore region). From these results we can conclude that strategies that involve increasing scaffold porosity to improve cellular infiltration into tissue engineering scaffolds are justified. The caveat to this approach is that increasing scaffold porosity typical results in decreased mechanical properties. It can be reasoned, with this inversely weighted relationship, that a middle ground may be reached where scaffold porosity is maximized while retaining adequate mechanical strength. Secondary observations in this study regarding the rates of cell infiltration suggest that, even if a scaffold is optimized to possess the maximum porosity for its application, the dynamics of cell migration will limit the speed at which cells occupy a significant portion of the scaffold. With this in mind, future efforts focused on determining the alternative mechanisms of cellular infiltration may lead to better understanding and control of the initial rapid infiltration.

CHAPTER 6

Pilot Studies and Theories Regarding the Mechanisms of Cell Infiltration into Electrospun Scaffolds

Preface: This study will test the hypothesis that cells infiltrate into electrospun scaffolds through passive as well as active means and that scaffold porosity plays a central role in governing the infiltration process.

6.1 INTRODUCTION

A commonly identified weakness, and consequently one that is attracts considerable attention in the field of tissue engineering, concerns the relatively low rate at which cells will infiltrate into an electrospun scaffold.[142,143] Most load-bearing scaffolds support cell infiltration to depths of only one to two hundred microns in tissue culture, a depth that is insufficient for use in the fabrication of tissues in vitro for in vivo replacement of dysfunctional tissues and or organs. It is clear that increasing the porosity of a scaffold can increase cell penetration and increase the density of cells present with the fiber arrays of an electrospun scaffold.

Results presented in Chapter 5 of this study demonstrate that cells can penetrate a considerable distance through the macropores of an air impedance scaffold. Further, circumstantial evidence would suggest that the extrapolated velocity that the cells would have to achieve in order to penetrate as far as they did would appear to rule out active migration in the process. In order to penetrate the fiber arrays of these scaffolds cells would literally have to migrate in a very circuitous route just to enter the scaffolds. Finally, with no external signaling to drive cells to migrate across the axis of the fibers there does not appear to be any impetus for them to enter further than the first several microns of the constructs. Without some sort of a signaling gradient it seems unlikely that cells will migrate very far into the densely packed fiber arrays. These observations further reduce the possibility that active migration can account for the penetration of cells deep into an electrospun scaffold over short intervals of time. This final study focuses on

defining the role that passive processes play in mediating the penetration of cells into electrospun scaffolds.

6.2 MATERIALS AND METHODS

Electrospinning

All reagents were obtained from Sigma unless otherwise noted. Polycaprolactone (PCL: 65,000 M.W.) was suspended and electrospun from trifluoroethanol (TFE) at concentrations of either 150 mg/mL (producing small fibers with beads) or 250 mg/mL (producing large fibers). Electrospinning syringes were capped with a blunt-tipped 18-gauge needle and placed into a syringe driver (Fisher Scientific) set to deliver the electrospinning fluid into the electrospinning chamber at a rate of 8 mL/hr.[9] A static electric field ranging from 18 kV-21 kV (Spellmen) was used to initiate electrospinning across a 20 cm gap. A grounded solid metal mandrel (length = 11.75 cm, diameter = 6.33 mm) or a grounded perforated metal mandrel (functional length = 11.75 cm, mandrel diameter = 6.33 mm, pore diameter = 0.75 mm spaced laterally 2 mm and vertically 1.5 mm) was used a target.[5,9] The target mandrels were designed to rotate and translate laterally (4 cm/s over a 12 cm distance) in order to facilitate an even distribution of fibers.

Cell Culture

Human dermal fibroblasts (hDF, Cascade Biologics C-013-5C) were cultured in DMEM-F12 (Gibco) supplemented with 10% fetal bovine serum (FBS, Hyclone) and 1% penicillin/streptomycin (P/S, Invitrogen). Electrospun scaffolds were sanitized in 70% ethanol for 30 minutes, rinsed 2x in phosphate buffer solution (PBS) and rinsed 1x in media. Cells were seeded at a concentration of 25,000 cells onto 6 mm round electrospun scaffolds and cultured in

an incubator set to 37°C and 5% CO_2. A glass cloning ring was used to keep the cells on the dorsal surfaces of the scaffold during the first 24 hr of culture. Media was changed every 3 days. At the conclusion of experimental intervals scaffolds were crosslinked in 4% glutaraldehyde for 10 min followed by 2x PBS rinses. Scaffolds were stored in PBS at 4°C prior to processing for microscopy. Sections were stained with 4',6-diamidino-2-phenylindole (DAPI) to visualize nuclei. Rhodamine phalloidin (1:50 in PBS plus 10 µg bovine serum albumin; BSA) was used to identify actin, and α smooth muscle actin (α-SMA) antibody (1:50 in PBS plus BSA, anti-alpha-Sm-1) was used to visualize α-SMA fibers.

Culture Manipulation Experiments – Trypsin Treatment

Scaffolds subjected to in-culture trypsin treatment were treated once a day until fixed. Trypsin treatment was performed under careful sterile and low-flow conditions (extreme care during pipetting). First the culture media was removed from each well. The scaffolds were then immediately washed with PBS for 10 minutes. The PBS was removed after 10 minutes and 40 µL Trypsin+EDTA was pipetted onto the scaffolds which were then incubated for 10 minutes at 37°C and 5% CO_2. Following incubation each treatment well with PBS was filled with an additional 120 µL culture media for 60 minutes at 37°C and 5% CO_2 to neutralize the trypsin (pipetting must be done with extreme care at this point – if the cells are free from the matrix they could easily be washed away). Finally the trypsin/media mixture was removed and the wells were filled with media and placed back in the incubator 37°C and 5% CO_2 at until the following days' treatment.

Cryosectioning

Cross linked samples were incubated in a 30% sucrose solution prepared in PBS for three days at 4^{o}C. Samples were then placed into the well of a flat-bottom, 48 well culture dish filled with optical temperature cutting compound (OTC), pressed to the bottom of the dish and allowed to freeze in a flat configuration, and the cut into frontal, serial 50 µm thick frozen sections. Cut samples were placed immediately into PBS and stored at 4^{o}C until further processing.

Image Analysis

All images were captured on a Nikon TE300 microscope equipped with a 10x objective and a DXM 1200 digital camera at a resolution of 1280x1024. Overlapping images across the frontal sections were captured in a systematic raster scan fashion. A brightfield image and a matching fluorescence image was captured from each domain prior to moving the camera to the next field of view, this was done to insure registry between the two channels. Brightfield and fluorescence images were overlaid using Adobe Photoshop CS4, the fluorescence channel was turned off and the photomerge function was used to assemble the individual images into a montage of the entire frontal section.

3-Dimensional (3D) Reconstruction

The montage images of each serial frontal section were imported into a Google SketchUp work space and placed in a z-stack orientation. As noted in Chapter 4 the distance between each frontal section was increased by a factor of ten to better visualize scaffold layer properties. Montage composite images were manually aligned in the vertical orientation using scaffold features associated with the macropores. To better visualize the position of cells 3D objects

representing the cells were imported and used to replace the DAPI staining marking the position of cells within the scaffolds.

Statistics

Data sets were screened using ANOVA. The Holm-Sidak method was used for pairwise comparisons. P values as provided. Graphical depictions represent +/- the standard error unless otherwise noted.

6.3 RESULTS

Our results indicate that cells are found deep within the matrix of an air impedance scaffold afforded by the fibers of an electrospun matrix within 24 hrs. To characterize the relative contributions of passive processes, for example the simple diffusion of cells into these deep regions through the macropores present in an air impedance scaffold and events associated with active migration we plated cells onto a scaffold to determine the extent to which they spread out during the first 24 hr of culture. As judged by rhodamine phalloidin staining of polymerized actin fibroblasts seeded for 6 hours onto PCL scaffolds exhibit clear evidence of spreading. Conservatively, if cells take to 6 hours to attach and spread to this extent the window in which active migration can take place is far less than 24 hours (the period of time in which cells were detected as deep as 142 microns into the scaffolds) and may be as little as 18 hr. This would increase the estimated rate of active migration from about 6 microns per hour to nearly 8 microns per hour. This velocity seems even more unlikely to occur within the dense fibrous structure of an electrospun matrix composed of a synthetic polymer.

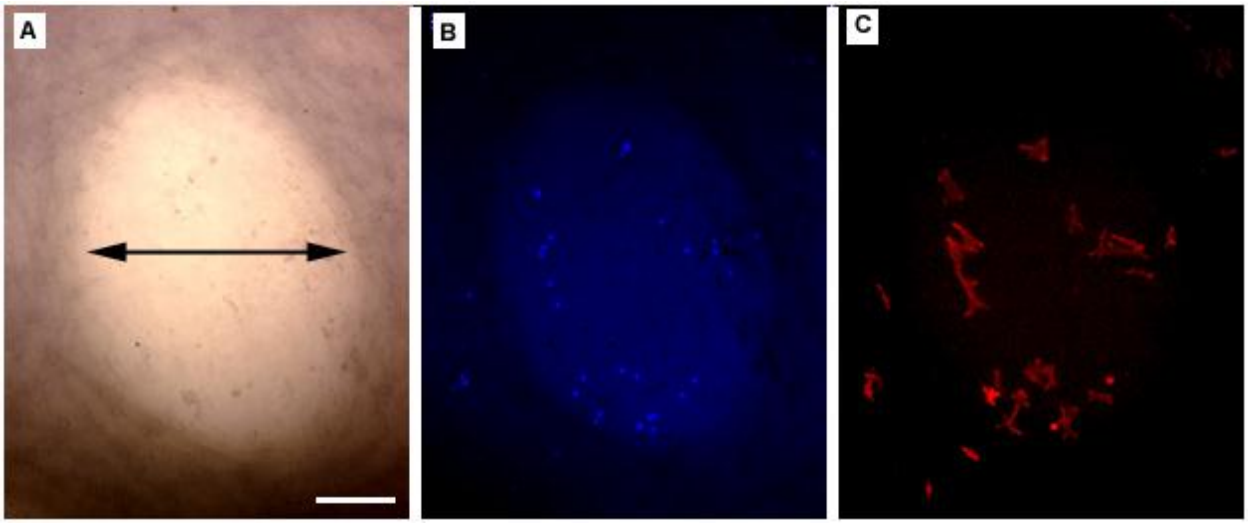

Figure 6.5. *Cell seeded surface of a scaffold produced from spinning 150mg/mL PCL in an air impedance system (no air flow). This image was taken 6 hours after cell seeding, 6 hours after seeding. Panel A depicts a bright field image of a macropore region, arrow indicates the diameter of the structure. Panel B depicts DAPI staining present. Panel C depicts rhodamine phalloidin staining of the actin cytoskeleton. Scale bar = 200 µm.*

Next we examined how the structure of different scaffolds modulates this baseline observation. Cells on all scaffolds at early time points appeared to be more or less dispersed in a random fashion over the surface of constructs during the first several hours of culture (e.g. as in Figure 5.11). Cells plated onto scaffolds produced with a solid mandrel remained dispersed and scattered over the entire surface of the construct at low density after 24 hours (Figure 6.6). Staining for actin on solid mandrels did not appear to concentrate in any specific area. In contrast, cells plated onto scaffolds fabricated onto perforated mandrels appeared to concentrate over the vicinity of the macropores and were well spread (figure 6.6). There is an insufficient number of observations to know if cells in the areas surrounding the macropores behave as if

they are plated onto a scaffold produced on a solid mandrel. No clear differences were observed between cells plated out onto the scaffolds produced with the perforated mandrels with or without air flow.

By day 3 the distribution and morphology of cells plated onto the perforated mandrels is markedly changed. On scaffolds produced on solid mandrels the cells remain dispersed over the surface and are well spread and stain brightly with the rhodamine. Cells on scaffolds produced on the perforated mandrels consistently appear to become concentrated along the rim of the macropores, staining for actin is very intense in these regions (Figure 6.7). This increased density of cells could be explained by the preferential migration of cells into these regions and or by a localized increase in proliferation rates. There is precedence for this type of cell concentration as a result of migration. In cell culture experiments cells suspended within collagen gels migrate to the periphery of the gels. Over time the cells contract the gels in an actin dependent manner, in part mechanical signals play a role in regulating this response. [144] The mechanical properties of scaffolds produced with pores are likely to vary considerably across the transition from the pore region where fibers are a relatively low density to the non-pore regions where the fibers are a very high density. This gradient may play a role in directing the concentration of cells during the early phases of culture along the rim of the pores.

Over the interval of day 3 to day 7 cells there were no remarkable changes in the appearance of the cultures. Cells in scaffolds produced on the perforated mandrels did display some propensity to express an elongated aligned phenotype across the fibers present in the macropores, this

phenotype was partially evident in pores that exhibited a low density of cells (see Figure 6.8 air impedance mandrel no air sample)

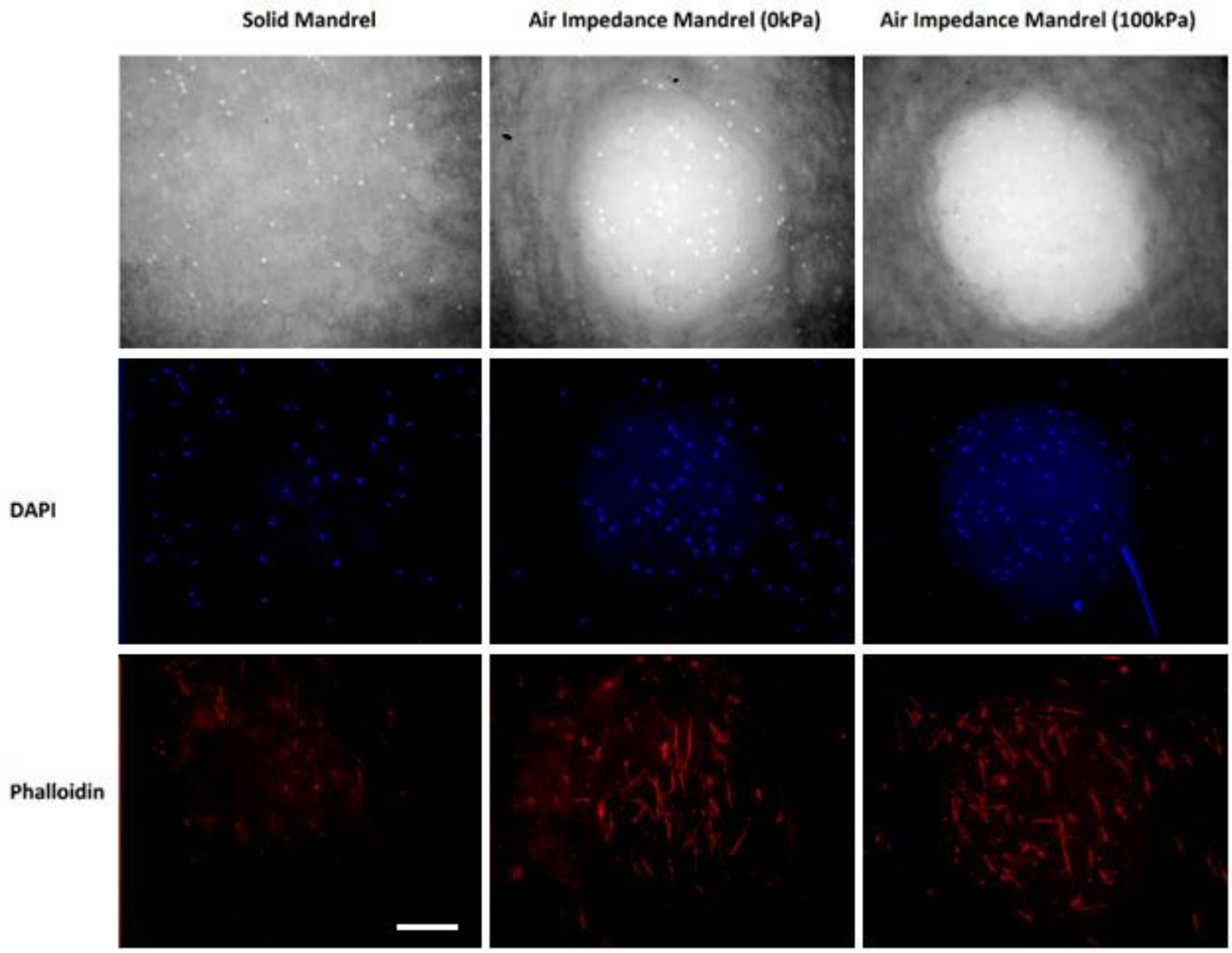

Figure 6.6. *Images taken from the surface of 150mg/mL PCL scaffolds prepared on a solid mandrel or a perforated mandrel with and without air flow. Cells were plated for 24 hr and processed for analysis. Brightfield images are depicted across the top of the panel, the macropores present in the scaffolds produced on perforated mandrels are readily visible. Note the poor staining present in cells plated out onto solid mandrel, cells stain weakly and are poorly spread. In contrast cells plated onto perforated mandrels and localized over the macropores*

stain brightly with rhodamine and are well spread. Cells in areas adjacent to the macropores appear to exhibit a phenotype more like cells plated onto solid mandrels. Scale bar = 200 µm.

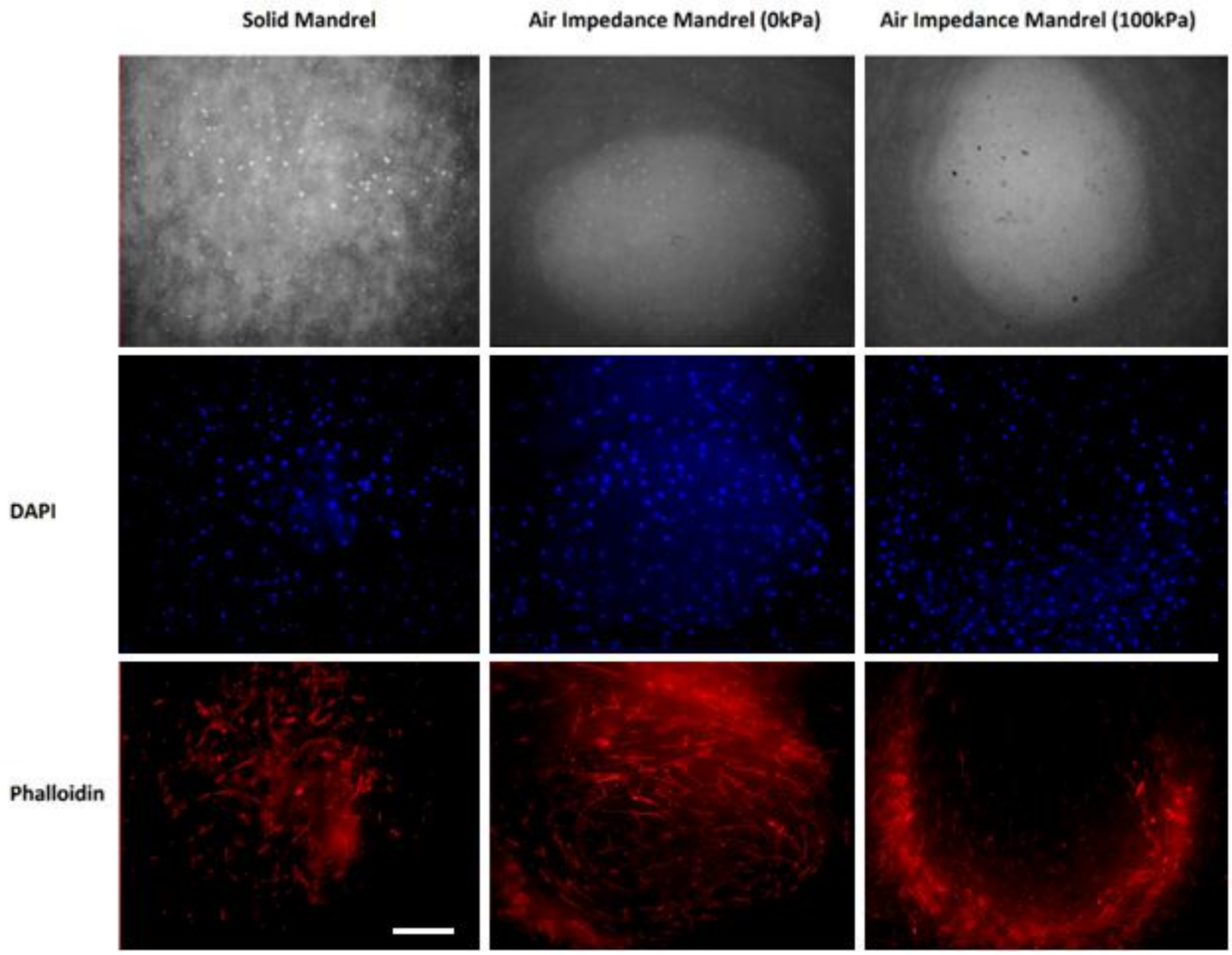

Figure 6.7. *Images taken from the surface of 150mg/mL PCL scaffolds prepared on a solid mandrel or a perforated mandrel with and without air flow. Cells were cultured for 3 days. Brightfield images are depicted across the top of the panel. Note how cells accumulate along the periphery of the pores scaffolds produced on perforated mandrels in what some authors refer to as a "contractile ring". Scale bar = 200 µm.*

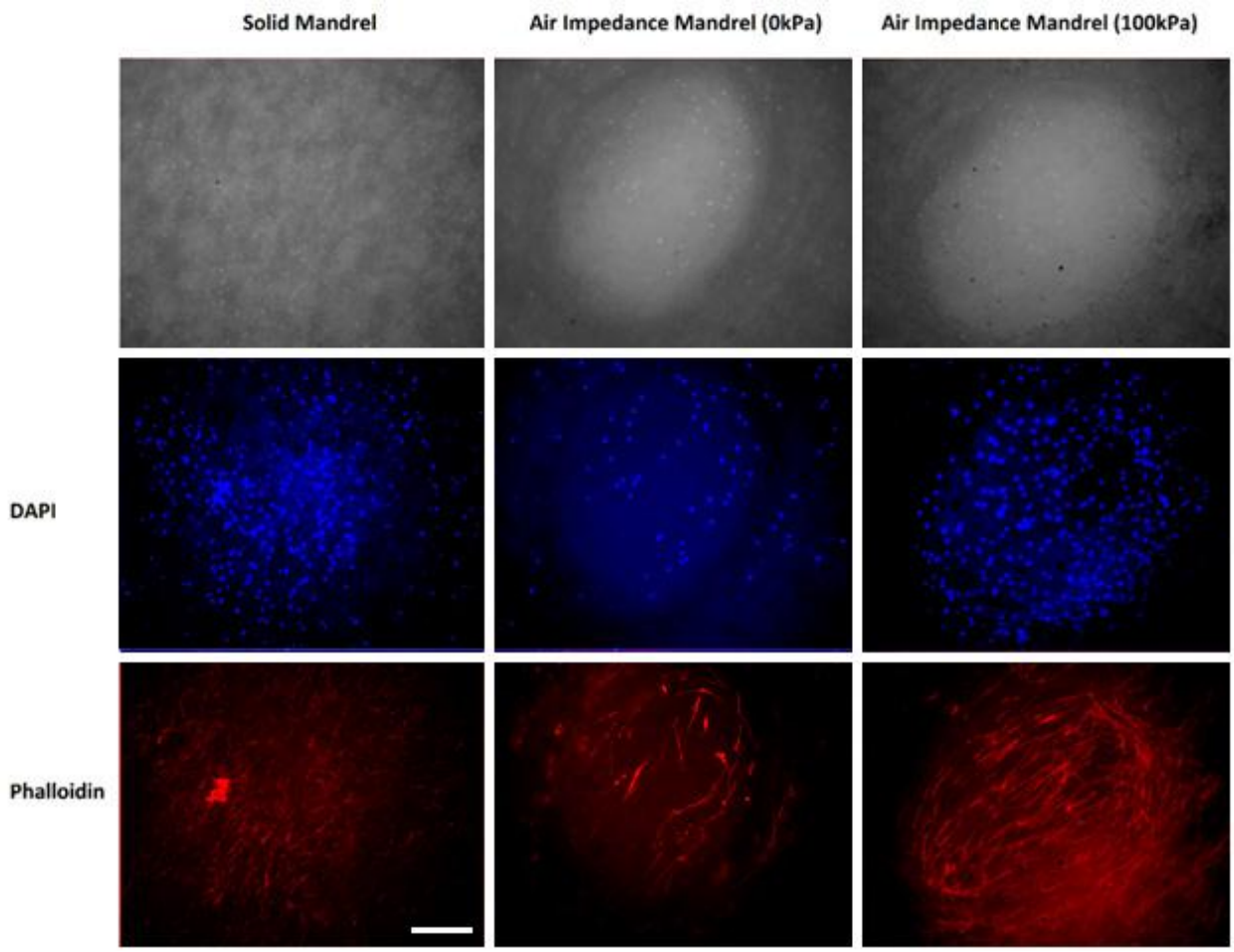

Figure 6.8 *Images taken from the surface of 150mg/mL PCL scaffolds prepared on a solid mandrel or a perforated mandrel with and without air flow. Cells were cultured for 7 day. Brightfield images are depicted across the top of the panel. Note the alignment of cells and the elongated phenotype expressed in regions associated with the macropores. This phenotype is particularly evident when regions are sparsely populated; see rhodamine staining for air impedance mandrel with no air. Scale bar = 200 µm.*

Fibroblasts can undergo differentiation into myofibroblasts and express arrays of alpha smooth muscle actin (α-SMA) positive fibers under the influence of transforming growth factor-β (TGF-β). These cells are highly contractile and mediate wound contraction in cutaneous injuries. The aligned phenotype of cells in the vicinity of the macropores in scaffolds produced on perforated mandrels is consistent with that observed with this differentiation process. To evaluate the phenotype of the cells present in the scaffolds we conducted staining experiments to determine if α-SMA was preferentially expressed in localized regions of the scaffolds. A positive control experiment was first conducted in which cells plated onto tissue culture plastic were exposed to 5 µL/100 µL PBS for 7 days and then stained for the presence of α-SMA positive fibers. The results of this preliminary experiment are presented in figure 6.9. This experiment confirms the activity of the antibody. Next we cultured cells for 14 days on a scaffold prepared on an air impedance mandrel and stained the culture for *α-SMA.* There was only a very low expression of this marker for myofibroblasts, indicating that most cells retained a normal fibroblastic phenotype (Figure 6.10).

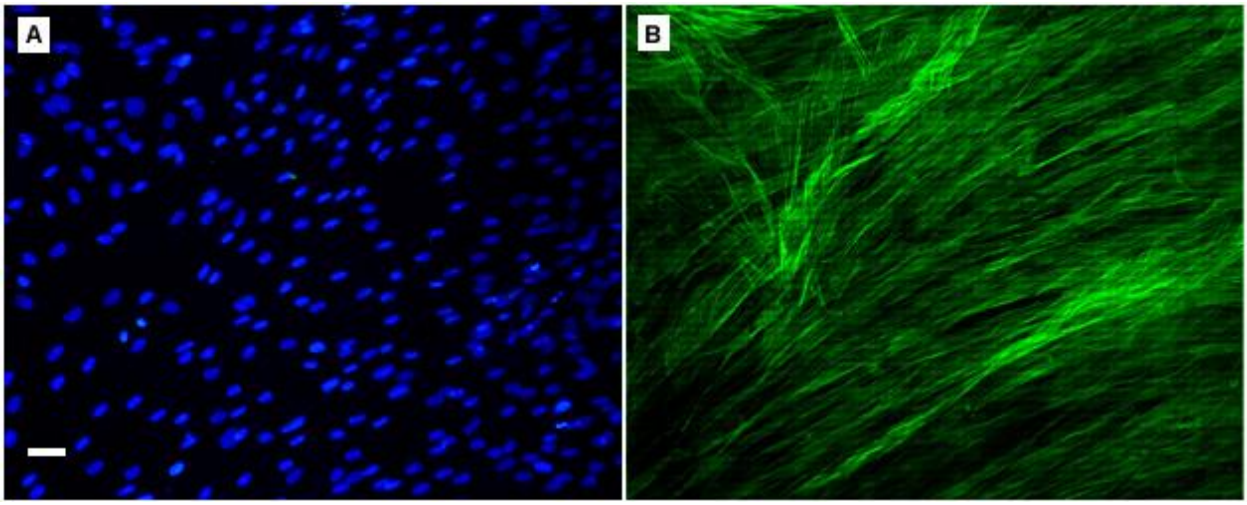

Figure 6.9. *α-SMA controls plated onto tissue culture plastic and treated with TGF-β express α-SMA positive actin fibers. Panel A, DAPI staining, PANEL B α-SMA. Scale = 10 µm.*

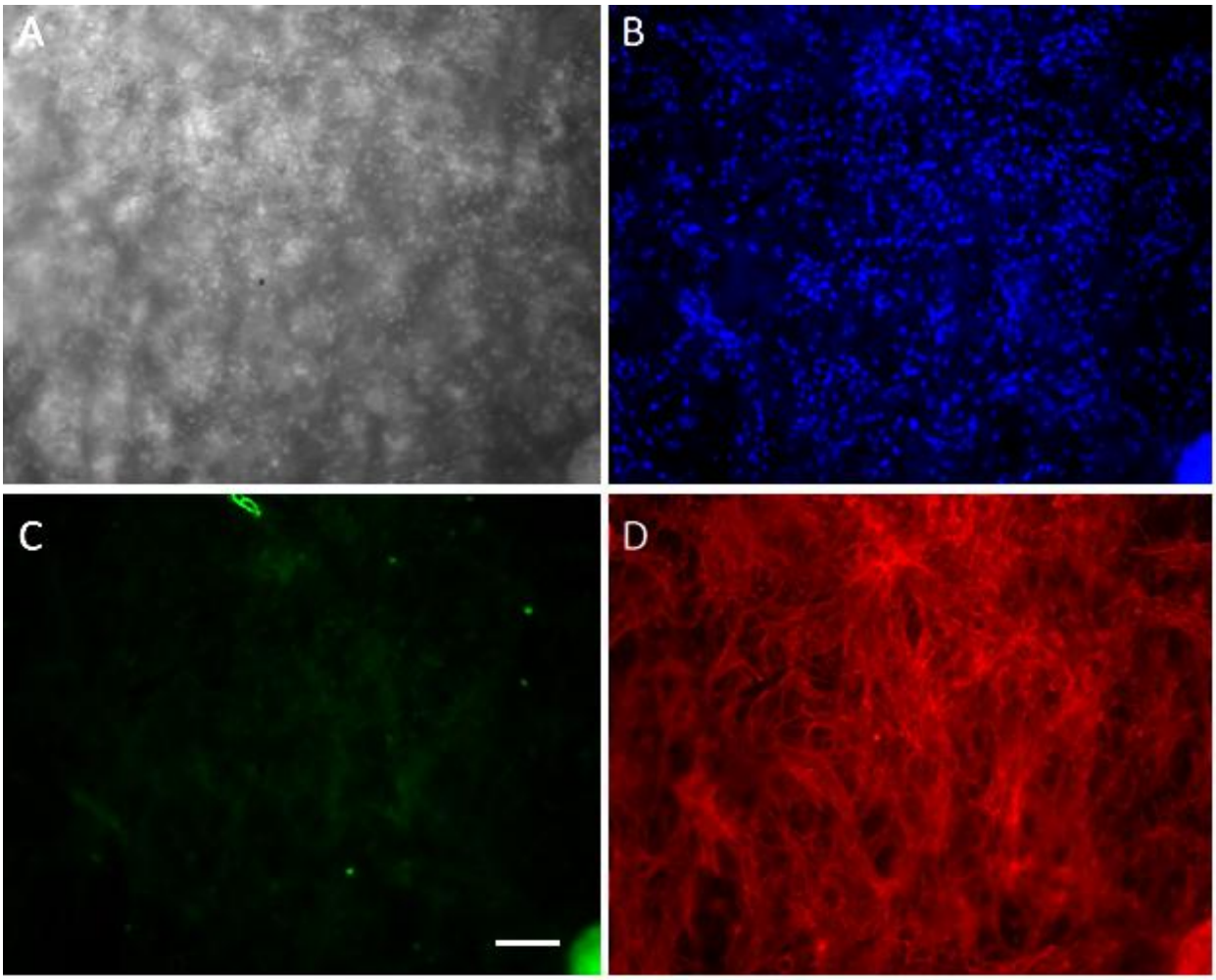

Figure 6.10. *Three is no clear evidence that human dermal fibroblasts undergo differentiation into myofibroblasts in response to local environmental cues on electrospun scaffolds. This image taken from the surface of an air impedance scaffold over a pore region. Images taken at day 14. Panel A, brightfield image, B DAPI image, C α-SMA and D rhodamine phalloidin. All images taken from the same field of view with cells that were triple stained for the fluorescence makers. Similar results were observed on all types of scaffolds at different time points. Scale bar = 100 µm.*

In summary our experiments indicate that it takes several hours for cells to attach and spread out on the surface of electrospun PCL scaffolds. Cells do appear to concentrate in the vicinity of the macropores that are present in scaffolds produced on the perforated air impedance mandrels. While these cells appear to express a phenotype similar to that of the myofibroblast they do appear to retain a normal phenotype on these constructs. These observations fail to reveal an obvious mechanism to account for the deep infiltration of cells into the scaffolds at early time points. Nor can these observations distinguish between processes that might be passive or active with respect to mediating cell penetration into the electrospun scaffolds.

Exploring mechanisms of cellular infiltration into scaffolds.

To test the hypothesis that cells sieve into electrospun scaffolds we suspended dermal fibroblasts in PBS and exposed them to 5% paraformaldehyde for 30 minutes. The cells were then rinsed PBS supplemented with 10 mg/ml BSA, recovered and plated onto tissue culture plates and electrospun scaffolds. Obviously this cross linking interval eliminates all possibility that active migration processes can take place, the cells are dead. Figure 6.11 shows the results from a live-dead staining assay of cells plated onto tissue culture plastic, all cells stained (red) with the marker indicating the plasma membranes were damaged and the cells were dead.

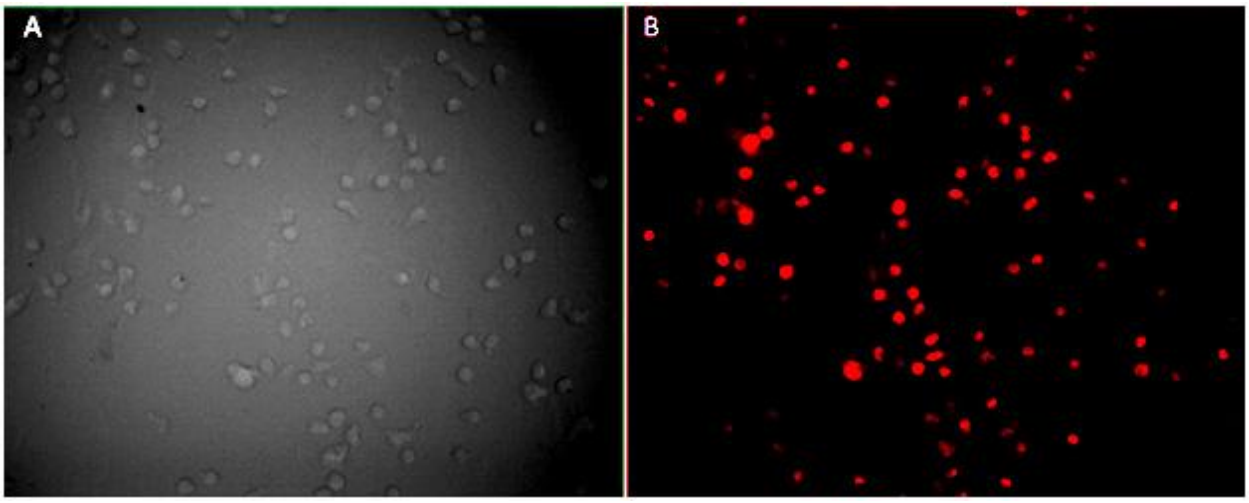

Figure 6.11. *Panel A bright field image, Panel B live-dead staining confirmed that cells were not viable at the time they were seeded onto scaffolds.*

Once the live dead staining assays were completed the dead cells were plated onto air impedance scaffolds (250 mg/mL, no air) for 1 day, stained with DAPI and processed for microscopic evaluation. Samples were embedded and frozen and then cut into 50 µm thick sections along the frontal plane to provide unambiguous data concerning the position of the cells in the Z axis. Cells were found to be as deep as 300 µm in these experiments (Figure 6.12, n=4). These data suggest that cells can passively sieve to considerable depth in the scaffolds.

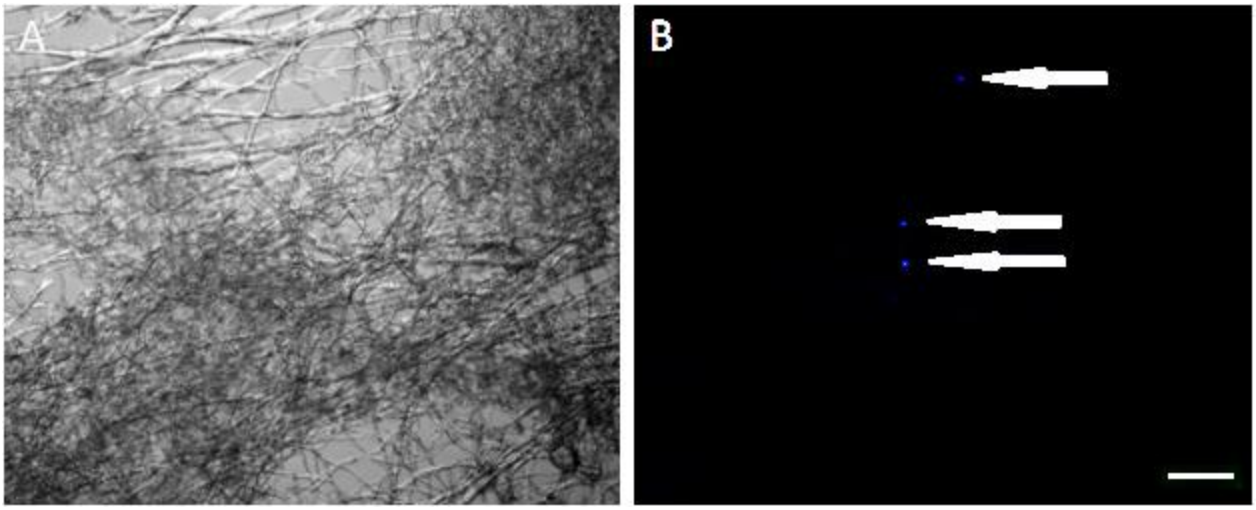

Figure 6.12. *To determine the extent to which passive processes modulate cell infiltration into electrospun scaffolds we plated dead cells onto the constructs for 24 hr. While cell density was low cells were detectable in frontal frozen sections as deep as 300 µm. This image was captured from the number 6 section from a scaffold; each frozen section was 50 micron thick. Panel A bright field image of the section, Panel B DAPI positive staining of cells. Scale bar = 100 µm.*

A natural extension of these experiments is to attempt to develop a 3D cell culture protocol designed to take advantage of the passive aspect of cell infiltration into porous scaffolds. To do this cells were plated onto scaffolds and at 24 hours intervals treated with trypsin+EDTA for 3 days. This results in the enzymatic release of cells from cell-matrix attachment sites and promotes cultured cells to adopt a spherical conformation in response to internal tension. Figure 6.13 shows the normal infiltration/distribution pattern of cells as a function of depth in scaffolds seeded with fibroblasts and cultured under baseline conditions. Cells are predominantly on the surface of the scaffolds with numbers decreasing in an exponentially decaying fashion with respect to scaffold depth.

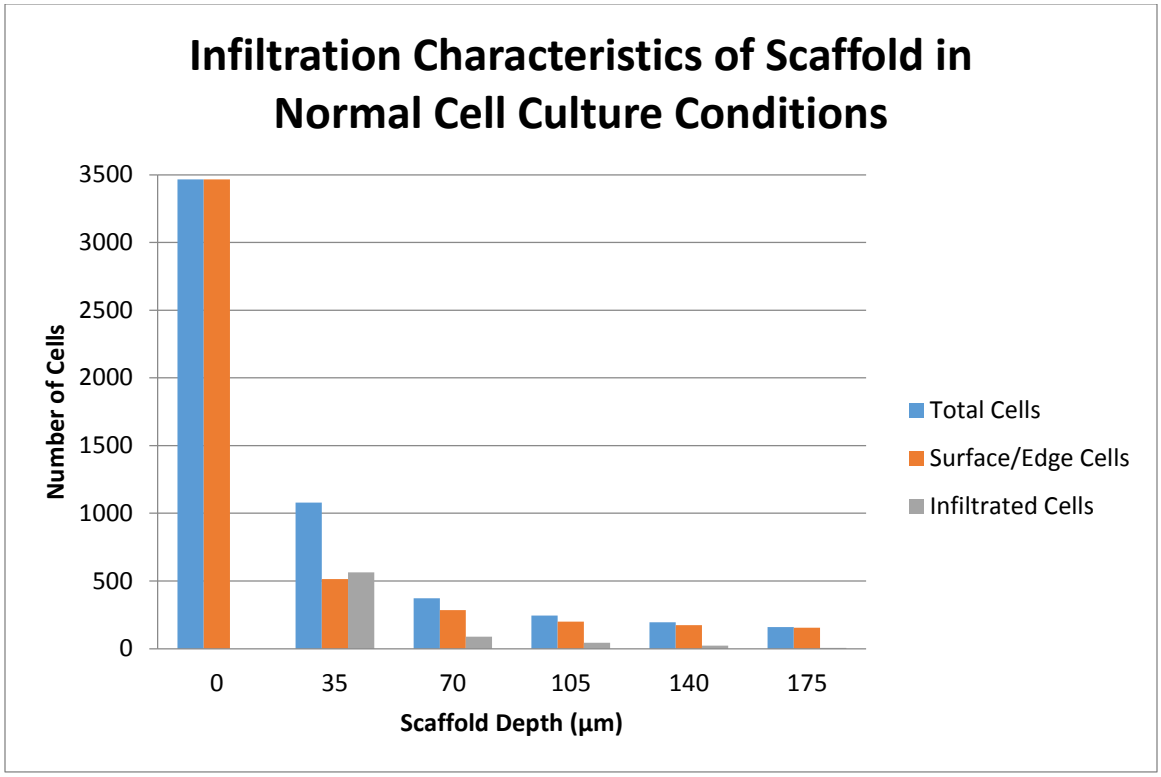

Figure 6.13. *Cells were plated onto a 150 mg/mL PCL scaffold fabricated on an air impedance mandrel (no air flow) and cultured for 3 days. At daily intervals cultures were incubated with fresh media to simulate and control for any effects that fluid disturbances might play in the experiments conducted with trypsin (where the media was removed and replaced with PBS trypsin at daily intervals). The X axis reports the number of cells counted based on DAPI staining, the Y axis reports the depth inside the scaffold where the cells were counted using serial frontal sections. Total cells refers to all cells counted, surface edge cells refers to those cells that occupy the peripheral surfaces of the cultures and infiltrated cells refer to cells within the scaffold and at least 50 µm from the lateral edges.*

Figure 6.14 represents a scaffold treated with tryspin+EDTA for 3 days with the goal of increasing the rate and extent of cellular infiltration into the scaffolds. While these pilot studies were not sufficient to determine statistical significance, the modified culture conditions produced cellular infiltration far superior to anything observed control experiments. The results of this pilot study suggest that cyclically releasing the cells by enzymatically disrupting the cell matrix attachments allows the cells to undergo repeated cycles of passive sieving deeper into the scaffolds. At a depth of 175 microns scaffolds were virtually devoid of cells under control conditions, cultures treated with the trypsin exhibited scattered populations of cells.

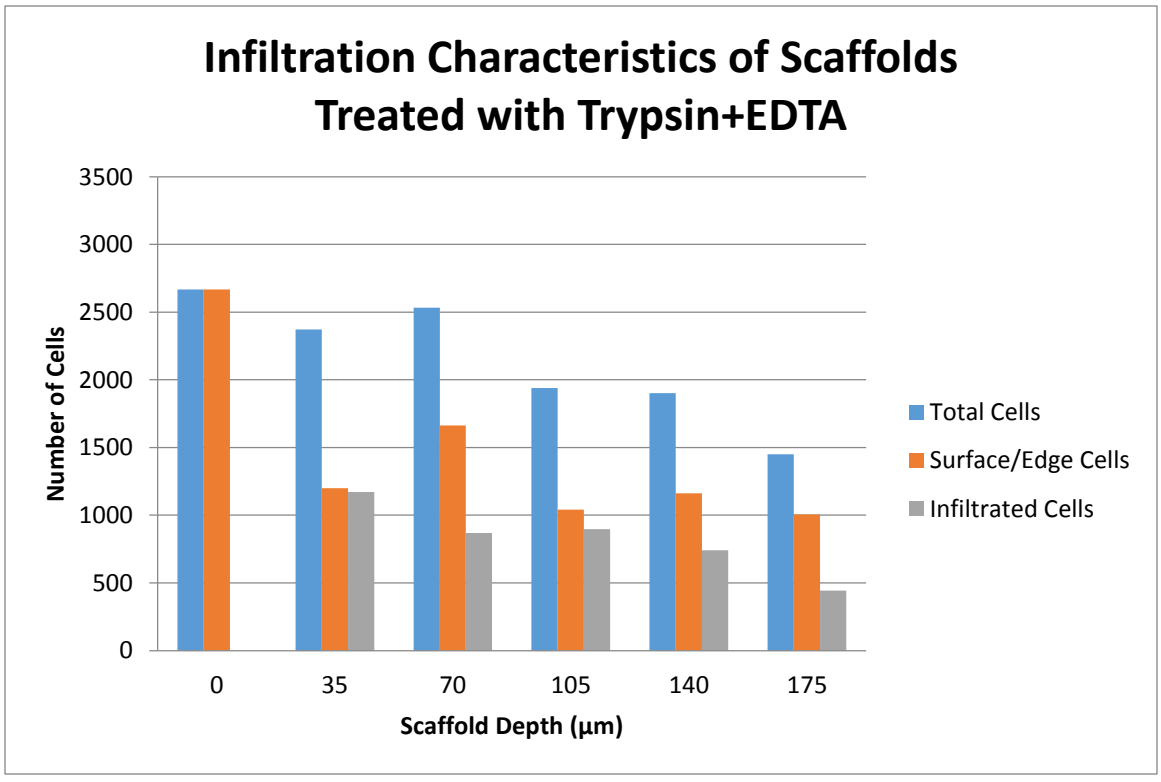

Figure 6.14. *Cell infiltration patterns seen in a 150 mg/mL PCL air impedance scaffold (no air flow) seeded with fibroblasts and incubated in trypsin at 24 hour intervals. The X axis reports*

the number of cells counted based on DAPI staining, the Y axis reports the depth inside the scaffold where the cells were counted using serial frontal sections.

Figure 6.15 summarizes the results of the experiment documented in figures 6.13 and 6.14. This plot highlights the characteristics of cellular infiltration into the scaffolds given the culture conditions. With everything held constant (scaffold type, flow conditions, culture time, etc) the trypsin treated cultures produced conditions that promoted cell penetration with respect to the controls at all depths.

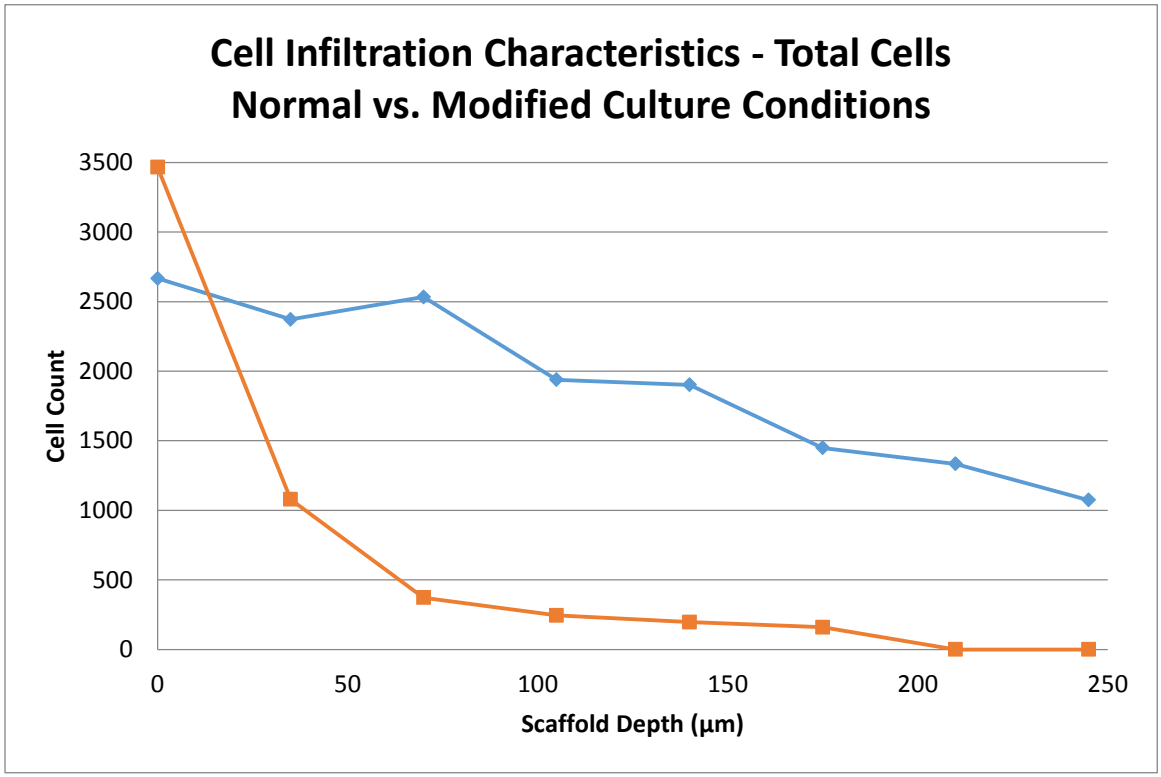

Figure 6.15. *Plotting the total cell count with respect to scaffold depth emphasizes how the cyclic trypsin protocol impacts cell number at different depths. Where blue represents the cultures treated with enzyme and orange represents controls. The X axis reports the number of*

cells counted based on DAPI staining, the Y axis reports the depth inside the scaffold where the cells were counted using serial frontal sections. The modified experimental culture group consisted of daily treatment with trypsin+EDTA whereas the normal culture group consisted of treatment with media only to control for fluid flow conditions. Cultures treated with the enzyme protocol exhibited a nearly linear function of cell number vs. depth (linear trend line yields an r^2 *value of 0.9483) as opposed to controls that exhibit n exponential decay-like function across the Z axis of the scaffold.*

Figure 6.16 summarizes the actual number of cells that have penetrated into the scaffold (Figure 6.15 depicts total cell number including those cells that remain on the surface of the scaffolds). From this plot it is evident that the "effective" number of cells infiltrating a scaffold under normal culture conditions becomes negligible after 75-100 µm of depth, however, treating the cultures with the trypsin protocol dramatically increased cell numbers throughout the scaffold. Further this is clear evidence that passive processes play a central role in the events that lead to cells penetrating an electrospun scaffold.

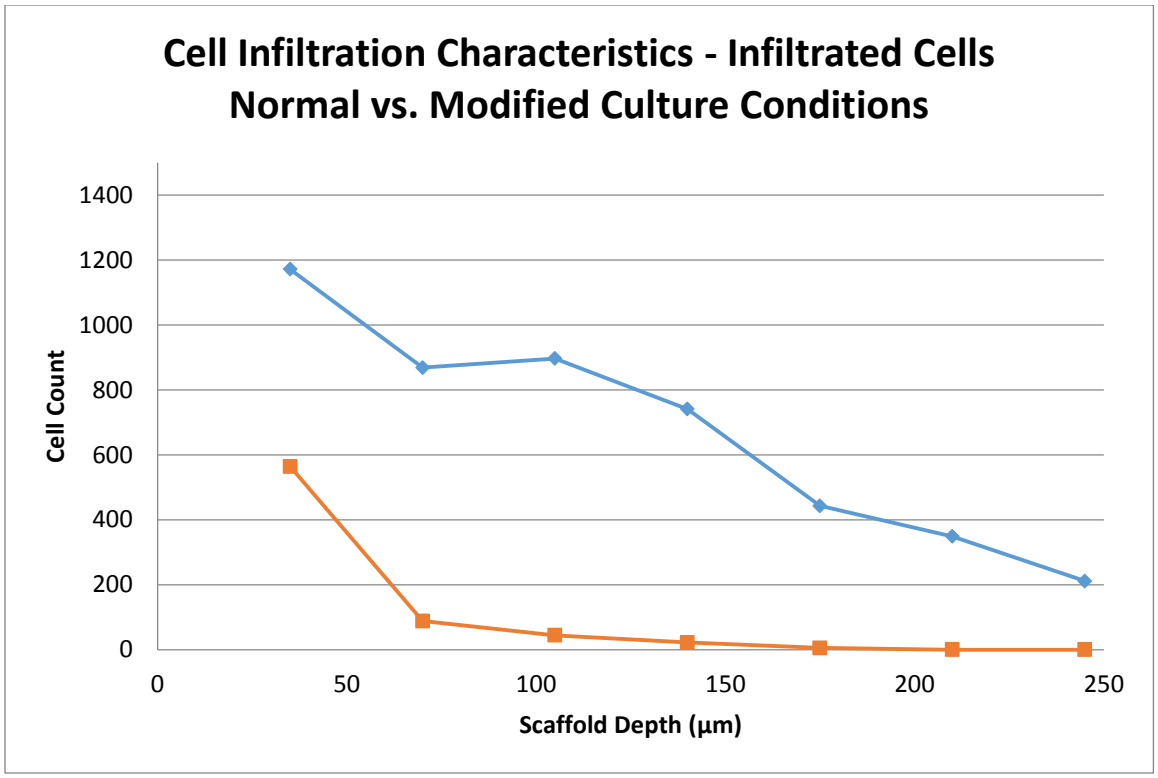

Figure 6.16. *Analyzing just the infiltrated cells gives a better idea of how effective the trypsin protocol is at increasing cell penetration. Where blue represents the cultures treated with enzyme and orange represents controls. The X axis reports the number of cells counted based on DAPI staining, the Y axis reports the depth inside the scaffold where the cells were counted using serial frontal sections.*

6.4 DISCUSSION

Several comments relevant to the discussion of the results reported in this chapter have already been presented throughout the body of the results. However, it is clear from the data that cells plated onto a scaffold produced on a solid mandrel do not appear to concentrate in any particular area of the scaffold. This result is in contrast to results reported with the scaffolds fabricated with macropores, cells clearly accumulate in these regions. The widely dispersed fibers present in these regions which define the "subpores" within the domain of the macropore likely are more efficient at capturing cells. During seeding the rounded cells would appear to adhere, or rather become trapped, more readily in these regions. The end result is an increased number of cells due to the physical characteristics of these regions, the cells can "fall" between the fiber and begin to undergo adhesion. In adjacent regions any physical or even thermal disturbances might be more likely to dislodge cells from the surface of the fibers.

The cells that initially adhere to regions associated with the macropores subsequently begin to accumulate along the periphery of these structures. While there is no obvious reason why this should occur work from other cell culture experiments using collagen gels it would appear that cells in this domains migrate to the edges like cells do in a collagen gel. One possible signal for inducing this response might be a mechanical gradient across the pores that cells "see" and detect and this mechanical gradient induces migration towards the periphery. The disparate concentration of electrospun fibers present in the pores and surrounding the pores must surely set

up a mechanical gradient (areas of low density and high density fibers plus any contractile forces applied by the cells across the network!).

Evidence that passive processes play an important role in the penetration of cells into electrospun scaffolds is provided by the experiments in which fixed, dead cells were plated and found deep within the scaffolds after 24 hr. Clearly migration cannot play a role in these results. One error that was made in these experiments was technical in nature, but this error may have inadvertently reduced the number of cells observed in the cultures. When cells are enzymatically released from a dish they round up, this rounding is a consequence of tension generated internally when the cells are attached to a culture dish. However, this process is not necessarily instantaneous and may take several minutes; until rounding is completed the cells may have odd elongated shapes and processes. These processes may suppress sieving because they increase cell cross sectional area which surely must be an important characteristic in sieving. Allowing the cells to rest for 30 minutes or so in solution and then fixing them might yield even more impressive results in these assays. The observation that cell shape could play an important role in these experiments may also be true in the experiments in which cells were repeatedly "dosed" with trypsin.

The second line of evidence that, albeit indirect, that supports the role of passive sieving in the penetration of cells into scaffolds comes from the trypsin experiments. While it takes time for cells to attach and spread on a synthetic scaffold they do spread and they do attach to these surfaces. Treatment with trypsin can be expected to release the cells from these attachments much like the release of cells from a tissue culture dish. Under these circumstances the cells

should round up and if there is sufficient pore area available the cells should then "fall" deeper into the scaffold in response to the enzyme treatment. One variable that could not be controlled for in these experiments is the possibility that the enzyme treatment drove cell penetration while inducing cell proliferation. This can be explored by determining the proliferative rate of cells in scaffolds treated with the enzyme regime.

6.5 CONCLUSION

Inducing cell infiltration into tissue engineering scaffolds is one of the major limitations facing the tissue engineering paradigm. Without the ability to promote and control the extent of cell infiltration into scaffolds the utility of using tissue engineering to replace damaged or diseased tissue is greatly limited. The central hypothesis of this study was that cell penetration into electrospun scaffolds was at the very least a biphasic event that entailed passive (i.e. sieving) as well as active (i.e. migration) processes. The results of this study suggest that a modification of this central hypothesis is necessary. While there is clear evidence of passive and active processes it is the passive phase that appears to be critical in during the early phases of culture. The active phases likely play a more important role once cells have sieved into a scaffold once the cells occupy regions in which they can migrate along the plane of the fiber arrays.

CHAPTER 7

Conclusion and Future Work

The central theme of this dissertation revolves around the idea of an easy to produce product that can be implanted in a patient to regrow diseased, damaged, or destroyed tissue. We typically refer to this hypothetical product as an ideal tissue engineering scaffold. The demand for an ideal tissue engineering scaffold stems from the needs of patients who suffer from tissue defects and the inadequacy of current treatment options. Unfortunately, current tissue engineering technology produces scaffolds with little architectural complexity that support very limited cellular infiltration. These basic limitations retard tissue ingrowth and overall tissue repair. In cases where a patient requires significant tissue repair the best regenerative option in use clinically today is an autologous scaffold which induces tissue regeneration by utilizing a physiologically-sized extracellular matrix, regenerative cues, and all while eliciting no immunogenic response from the patient. Autologous grafts come at the expense of donor site morbidity and with the caveat of a limited source. In some cases, harvesting the tissue to supply an autologous graft would be contraindicated due to limitations in a patient's ability to heal at the donor site. Lab fabricated tissue engineering scaffolds represent a logical research target because their limitations involve improving the performance of a relatively easily obtainable material as opposed to autologous grafts where the raw material is extremely precious. This dissertation focuses on taking tissue engineering technology forward in three ways: improving the architectural complexity possible in multi-layered electrospun scaffolds via gradient fiber electrospinning (Chapter 3), improving the ability to evaluate cell-scaffold interactions and develop three-dimensional reconstructions of cellular infiltration by making frontal sectioning of

large fibrous scaffolds possible (Chapter 4), and finally through the observation and subsequent experimentation on the tremendous potential of exploiting passive cellular infiltration to achieve significant improvements in the depth and extent of cellular penetration into tissue engineering scaffolds (Chapter 5 and 6).

Gradient fiber electrospinning represents an exciting advancement in electrospinning technology. This technique enables researchers to make multilayered scaffolds that exhibit gradual, rather than abrupt (e.g. laminate electrospinning) interlayer transitions which act to both mitigate delamination due to mechanical loading and to prevent interlayer gaps which could hinder cellular migration and interaction between layers. Unfortunately the potential of this technique was not realized immediately due to the well-described inadequacies of conventional cell culture methods to encourage deep scaffold infiltration of seeded cells. Because the cells cannot penetrate into the layer transition zones seeding on gradient fiber scaffolds is essentially the same as seeding onto scaffolds consisting of only one polymer concentration. The advancements in cell culture technology described in this dissertation make meaningful experimentation with gradient fiber scaffolds possible (Figure 7.1).

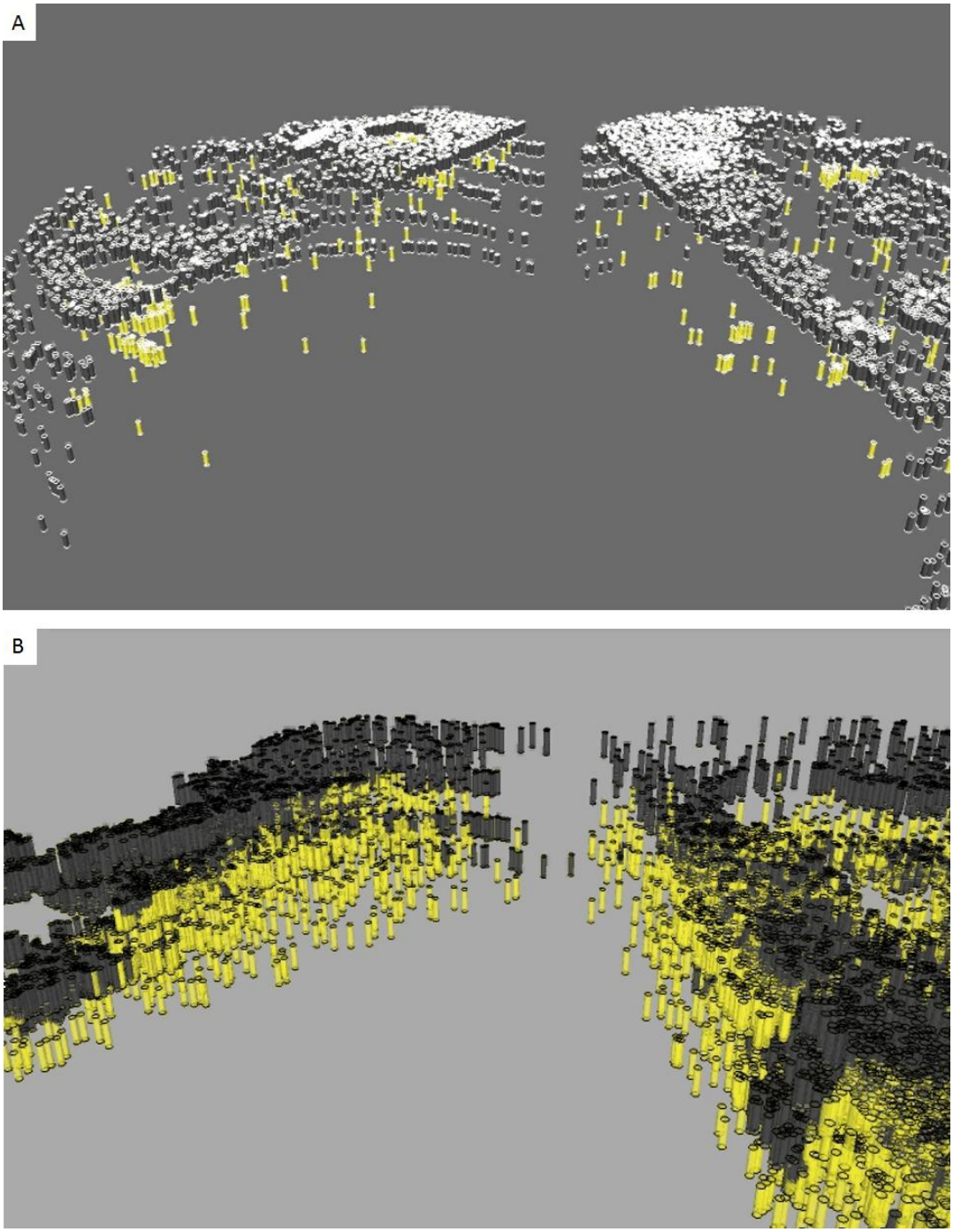

Figure 7.1. *In this figure are 3D representations of cellular infiltration generated by importing stained frontal sections into Google SketchUp and manually placing 3D objects over each cell (dark cylinder = surface/side cell, yellow cylinder = infiltrated cell). This shows the difference*

in infiltration between scaffolds in normal culture media (A) and those treated with trypsin+EDTA (B).

Through relatively simple modifications in cell culture conditions, e.g. the regular application of cell-matrix detachment agents such as trypsin+EDTA, researchers may be able to detach cells from a scaffold matrix to further encourage them to pass deeper into the structure (Figure 7.1). As our techniques and understanding of infiltration mechanisms improve we can start to incorporate factors such as scaffold orientation (e.g. some cells may float after detachment, some may sink), infiltration flow forces, and other infiltration forces to improve the speeds and consistency of cellular infiltration into scaffolds. Judging solely by the fastest infiltrations recorded in our studies (350 µm after day 1) and assuming that the cells cannot infiltrate passively after spreading (shown to occur no later than 6 hours after seeding), the potential passive infiltration velocities reach 58 µm/hr. This means that, if this passive phase of infiltration can be taken advantage of, cellular infiltration of a scaffold over a millimeter thick could occur in less than a day! Even more exciting is the potential in utilizing different cell-matrix attachment strengths. In this example, cells with strong matrix attachment strengths might be seeded first on one side of a scaffold using a highly concentrated trypsin+EDTA treatment. After the first side is seeded and the cells are allowed to attach the opposite side may be seeded with cells that possess weaker matrix attachment characteristics and thus requiring a lower concentration of trypsin+EDTA treatment which does not disrupt the first wave of cells already inside the scaffold. In this way researchers might be able to utilize the full potential of induced passive infiltration by saturating both sides of the scaffold. If this hypothetical scaffold was seeded in this manner it would be possible to produce scaffolds exhibiting one cellular profile on one side that transitions to another cell profile on the other side. In addition to 3D

layers of cells, the co-cultured transitional layer in the middle of the scaffold would be very interesting to study. For example, in pharmacological experiments a scaffold identical to our hypothetical scaffold might be produced and subjected to a drug. The scaffold could then be sectioned in cross-section and stained to determine the response of each cell type in homologous and heterogeneous population (a much more realistic scenario). Future research could lead to predictions of cellular infiltration rates given specific scaffold and culture conditions, making accurate 3D cell culture a reality. While we have shown promise to the idea, there is certainly a great deal of work to be done to fully understand how to take advantage of passive cellular infiltration into scaffolds. Despite this, mastering the ability to create a scaffold with a significant cell population throughout its structure would represent a step-jump in tissue engineering technology that could be achievable through the simple and logical passive mechanisms described in this dissertation.

Cited Resources

Scanning electron microscopy was conducted at the VCU, Department of Neurobiology and Anatomy Microscopy Facility, supported with funding from NIH-NCRR shared instrumentation Grant (1S10RR022495) and, in part, NIH-NINDS Center Core Grant (5P30NS047463). US and International Patents Pending.

Literature Cited

1 Harris DT, Badowski M, Ahmad N, et al. The potential of cord blood stem cells for use in regenerative medicine. Expert opinion on biological therapy 2007;7(9):1311.

2 Dhandayuthapani B, Yoshida Y, Maekawa T, et al. Polymeric Scaffolds in Tissue Engineering Application: A Review. International Journal of Polymer Science 2011;2011.

3 Griffith LG, Naughton G. Tissue Engineering: Current Challenges and Expanding Opportunities. Science 2002;295(5557):1009-1014.

4 Langer R, Tirrell DA. Designing materials for biology and medicine. Nature 2004;428(6982):487-492.

5 McClure MJ, Wolfe PS, Simpson DG, et al. The use of air- flow impedance to control fiber deposition patterns during electrospinning. Biomaterials 1201;33(3):771.

6 Agarwal S, Wendorff JH, Greiner A. Use of electrospinning technique for biomedical applications. Polymer 2008 12/8;49(26):5603-5621.

7 Chan B, Leong K. Scaffolding in tissue engineering: general approaches and tissue-specific considerations. Eur Spine J 0812;17(4):467-479.

8 Goh Y, Shakir I, Hussain R. Electrospun fibers for tissue engineering, drug delivery, and wound dressing. J Mater Sci 1304;48(8):3027-3054.

9 Grey CP, Newton ST, Bowlin GL, et al. Gradient fiber electrospinning of layered scaffolds using controlled transitions in fiber diameter. Biomaterials 1307;34(21):4993.

10 Lutolf MP, Hubbell JA. Synthetic biomaterials as instructive extracellular microenvironments for morphogenesis in tissue engineering. Nat Biotechnol 0501;23(1):47.

11 Pape HC, Evans A, Kobbe P. Autologous bone graft: properties and techniques. J Orthop Trauma 1003;24 Suppl 1:S36.

12 Triplett RG, Schow SR. Autologous bone grafts and endosseous implants: complementary techniques. Journal of Oral and Maxillofacial Surgery 1996;54(4):486-494.

13 Haraguchi Y, Shimizu T, Yamato M, et al. Scaffold-free tissue engineering using cell sheet technology. RSC Advances 2012;2(6):2184-2190.

14 Jha BS, Colello RJ, Bowman JR, et al. Two pole air gap electrospinning: Fabrication of highly aligned, three-dimensional scaffolds for nerve reconstruction. Acta Biomaterialia ;7(1):203-215.

15 Konig G, McAllister TN, Dusserre N, et al. Mechanical properties of completely autologous human tissue engineered blood vessels compared to human saphenous vein and mammary artery. Biomaterials 2009;30(8):1542-1550.

16 Alluin O, Wittmann C, Marqueste T, et al. Functional recovery after peripheral nerve injury and implantation of a collagen guide. Biomaterials 2009;30(3):363-373.

17 de Valence S, Tille J-, Giliberto J-, et al. Advantages of bilayered vascular grafts for surgical applicability and tissue regeneration. Acta Biomaterialia 2012;8(11):3914-3920.

18 Liu W, Ren Y, Bossert A, et al. Allotransplanted Neurons Used to Repair Peripheral Nerve Injury Do Not Elicit Overt Immunogenicity. PLoS ONE 2012;7(2).

19 Xu H, Holzwarth JM, Yan Y, et al. Conductive PPY/PDLLA conduit for peripheral nerve regeneration. Biomaterials 2014;35(1):225-235.

20 Valuckaite V, Seal J, Zaborina O, et al. High molecular weight polyethylene glycol (PEG 15-20) maintains mucosal microbial barrier function during intestinal graft preservation. J Surg Res 2013;183(2):869-875.

21 Breyer BN, Brant WO, Garcia MM, et al. Complications of Porcine Small Intestine Submucosa Graft for Peyronie's Disease. J Urol 2007;177(2):589-591.

22 Ezzell C. Pig Intestine Yields Versatile Tissue Graft. Sci News 1992;141(16):246-246.

23 Jha BS, Colello RJ, Bowman JR, et al. Two pole air gap electrospinning: Fabrication of highly aligned, three-dimensional scaffolds for nerve reconstruction. Acta Biomaterialia 2011 1;7(1):203-215.

24 Ding Y, Xu D, Feng G, et al. Mesenchymal Stem Cells Prevent the Rejection of Fully Allogenic Islet Grafts by the Immunosuppressive Activity of Matrix Metalloproteinase-2 and -9. Diabetes 2009;58(8):1797-1806.

25 Wimmer C, Krismer M, Gluch H, et al. Autogenic versus allogenic bone grafts in anterior lumbar interbody fusion. Clin Orthop 1999(360):122.

26 Hudson TW, Liu SY, Schmidt CE. Engineering an improved acellular nerve graft via optimized chemical processing. Tissue Eng 2004;10(9-10):1346-1358.

27 Vasita R, Katti DS. Nanofibers and their applications in tissue engineering. International Journal of Nanomedicine 2006;1(1):15-30.

28 Stammen JA, Williams S, Ku DN, et al. Mechanical properties of a novel PVA hydrogel in shear and unconfined compression. Biomaterials 2001;22(8):799-806.

29 Deligkaris K, Tadele TS, Olthuis W, et al. Hydrogel- based devices for biomedical applications. Sensors & Actuators: B.Chemical 2010;147(2):765-774.

30 Van Vlierberghe S, Dubruel P, Schacht E. Biopolymer-based hydrogels as scaffolds for tissue engineering applications: a review. Biomacromolecules 2011;12(5):1387.

31 Guiseppi-Elie A. Electroconductive hydrogels: Synthesis, characterization and biomedical applications. Biomaterials 2010;31(10):2701-2716.

32 Hoare TR, Kohane DS. Hydrogels in drug delivery: Progress and challenges. Polymer 2008;49(8):1993-2007.

33 Peppas NA, Bures P, Leobandung W, et al. Hydrogels in pharmaceutical formulations. European Journal of Pharmaceutics and Biopharmaceutics 2000;50(1):27-46.

34 Billiet T, Vandenhaute M, Schelfhout J, et al. A review of trends and limitations in hydrogel-rapid prototyping for tissue engineering. Biomaterials 2012;33(26):6020-6041.

35 Malda J, Visser J, Melchels FP, et al. 25th Anniversary Article: Engineering Hydrogels for Biofabrication. Adv Mater 2013;25(36):5011-5028.

36 Lam CXF, Mo XM, Teoh SH, et al. Scaffold development using 3D printing with a starch-based polymer. Materials Science & Engineering C 2002;20(1):49-56.

37 Rengier F, Mehndiratta A, Tengg-Kobligk H, et al. 3D printing based on imaging data: review of medical applications. Int J CARS 2010;5(4):335-341.

38 Lee JW, Kang KS, Lee SH, et al. Bone regeneration using a microstereolithography-produced customized poly(propylene fumarate)/ diethyl fumarate photopolymer 3D scaffold incorporating BMP- 2 loaded PLGA microspheres. Biomaterials 2011;32(3):744-752.

39 Tobita K, Liu LJ, Janczewski AM, et al. Engineered early embryonic cardiac tissue retains proliferative and contractile properties of developing embryonic myocardium. American journal of physiology.Heart and circulatory physiology 2006;291(4):H1829.

40 Akins RE, Rockwood D, Robinson KG, et al. Three- dimensional culture alters primary cardiac cell phenotype. Tissue engineering.Part A 2010;16(2):629.

41 Norotte C, Marga FS, Niklason LE, et al. Scaffold- free vascular tissue engineering using bioprinting. Biomaterials 2009;30(30):5910-5917.

42 Seol Y, Kang T, Cho D. Solid freeform fabrication technology applied to tissue engineering with various biomaterials. Soft Matter 2012;8(6):1730-1735.

43 Rengier F, Mehndiratta A, Tengg-Kobligk H, et al. 3D printing based on imaging data: review of medical applications. Int J CARS 2010;5(4):335-341.

44 Ru C, Luo J, Xie S, Sun Y. A review of non-contact micro- and nano- printing technologies. A review of non-contact micro- and nano-printing technologies 2014;24(5):053001.

45 Lantada AD, Morgado PL. Rapid Prototyping for Biomedical Engineering: Current Capabilities and Challenges. Annu Rev Biomed Eng 2012;14:73-96.

46 Woo Jung J, Yi H, Kang T, et al. Evaluation of the effective diffusivity of a freeform fabricated scaffold using computational simulation. J Biomech Eng 2013;135(8):84501.

47 Moore GE. Cramming More Components Onto Integrated Circuits. Proc IEEE 1998;86(1):82-85.

48 Jha BS, Ayres CE, Bowman JR, et al. Electrospun Collagen: A Tissue Engineering Scaffold with Unique Functional Properties in a Wide Variety of Applications. Journal of Nanomaterials ;2011.

49 Matthews JA, Wnek GE, Simpson DG, et al. Electrospinning of collagen nanofibers. Biomacromolecules 2002;3(2):232.

50 McClure MJ, Sell SA, Simpson DG, et al. A three-layered electrospun matrix to mimic native arterial architecture using polycaprolactone, elastin, and collagen: A preliminary study. Acta Biomaterialia ;6(7):2422-2433.

51 Woodruff MA, Hutmacher DW. The return of a forgotten polymer—Polycaprolactone in the 21st century. Progress in Polymer Science 2010;35(10):1217-1256.

52 George Collins, John Federici, Yuki Imura, et al. Charge generation, charge transport, and residual charge in the electrospinning of polymers: A review of issues and complications. J Appl Phys 2012;111:044701.

53 Xiang-Fa Wu, Yury Salkovskiy, Yuris A. Modeling of solvent evaporation from polymer jets in electrospinning. Appl Phys Lett 2011;98:223108.

54 Reneker DH. Bending instability of electrically charged liquid jets of polymer solutions in electrospinning. J Appl Phys 2000;87:4531.

55 Blackwood KA, McKean R, Canton I, et al. Development of biodegradable electrospun scaffolds for dermal replacement. Biomaterials 2008;29(21):3091.

56 Sill TJ, von Recum HA. Electrospinning: Applications in drug delivery and tissue engineering. Biomaterials 2008;29(13):1989-2006.

57 Matthews JA, Wnek GE, Simpson DG, et al. Electrospinning of collagen nanofibers. Biomacromolecules ;3(2):232.

58 NIH Estimates of Funding for Various Research, Condition, and Disease Categories (RCDC). Available at: http://report.nih.gov/categorical_spending.aspx.

59 Ganong's review of medical physiology. 24th ed. / Kim E. Barrett ... [et al.].. ed. New York : London: New York : McGraw-Hill Medical ; London : McGraw-Hill distributor; 2012.

60 Pardee J. Cell Origin, Structure, and Function. San Rafael: San Rafael : Morgan & Claypool Life Sciences; 2010.

61 Graaff VD. Human anatomy and physiology. Fourth edition.. ed.; 2013.

62 Boateng JS, Matthews KH, Stevens HN, et al. Wound healing dressings and drug delivery systems: a review. J Pharm Sci 2008;97(8):2892-2923.

63 Martin P. Wound Healing- Aiming for Perfect Skin Regeneration. Science 1997;276(5309):75-81.

64 Schreml S, Szeimies R, Prantl L, et al. Wound healing in the 21st century. J Am Acad Dermatol 2010;63(5):866-881.

65 1.2: Biology: The Study of Life. Available at: http://www.ck12.org/book/CK-12-Biology/r23/section/1.2/.

66 Blair HC, Zaidi M, Huang CL, et al. The developmental basis of skeletal cell differentiation and the molecular basis of major skeletal defects. Biological Reviews 2008;83(4):401-415.

67 Mi Q, Rivière B, Clermont G, et al. Agent-based model of inflammation and wound healing: insights into diabetic foot ulcer pathology and the role of transforming growth factor-β1. Wound Repair and Regeneration 2007;15(5):671-682.

68 Wilson SE, Mohan RR, Hong J, et al. The wound healing response after laser in situ keratomileusis and photorefractive keratectomy: elusive control of biological variability and effect on custom laser vision correction. Arch Ophthalmol 2001;119(6):889-896.

69 Haydock D, Hill G. Improved wound healing response in surgical patients receiving intravenous nutrition. Br J Surg 1987;74(4):320-323.

70 Callaghan T, Khain E, Sander LM, et al. A stochastic model for wound healing. Journal of statistical physics 2006;122(5):909-924.

71 Murphy PS, Evans GR. Advances in wound healing: a review of current wound healing products. Plastic surgery international 2012;2012.

72 Gottrup F, Ågren MS, Karlsmark T. Models for use in wound healing research: a survey focusing on in vitro and in vivo adult soft tissue. Wound Repair and Regeneration 2000;8(2):83-96.

73 Mutsaers SE, Bishop JE, McGrouther G, et al. Mechanisms of tissue repair: from wound healing to fibrosis. Int J Biochem Cell Biol 1997;29(1):5-17.

74 Bradley M, Cullum N, Nelson EA, et al. Systematic reviews of wound care management: (2). Dressings and topical agents used in the healing of chronic wounds. Health Technol Assess 1999;3(2):1.

75 Yip J, Shen Y, Berndt MC, et al. Primary Platelet Adhesion Receptors. IUBMB Life 2005;57(2):103-108.

76 The Molecular and cellular biology of wound repair. New York: New York : Plenum Press; 1988.

77 Leibovich SJ, Ross R. The role of the macrophage in wound repair. A study with hydrocortisone and antimacrophage serum. Am J Pathol 1975 Jan;78(1):71-100.

78 Hübner G, Brauchle M, Smola H, et al. DIFFERENTIAL REGULATION OF PRO-INFLAMMATORY CYTOKINES DURING WOUND HEALING IN NORMAL AND GLUCOCORTICOID- TREATED MICE. Cytokine 1996;8(7):548-556.

79 Barrandon Y, Green H. Cell migration is essential for sustained growth of keratinocyte colonies: The roles of transforming growth factor-α and epidermal growth factor. Cell 1987;50(7):1131-1137.

80 Koh TJ, DiPietro LA. Inflammation and wound healing: the role of the macrophage. Expert reviews in molecular medicine 2011;13:e23.

81 Gabbiani G. The myofibroblast in wound healing and fibrocontractive diseases. J Pathol 2003;200(4):500-503.

82 Serini G, Gabbiani G. Mechanisms of myofibroblast activity and phenotypic modulation. Exp Cell Res 1999;250(2):273-283.

83 Martin P, Lewis J. Actin cables and epidermal movement in embryonic wound healing. 1992.

84 Brock J, Midwinter K, Lewis J, et al. Healing of incisional wounds in the embryonic chick wing bud: characterization of the actin purse-string and demonstration of a requirement for Rho activation. J Cell Biol 1996 Nov;135(4):1097-1107.

85 Shah M, Foreman DM, Ferguson MW. Neutralisation of TGF-beta 1 and TGF-beta 2 or exogenous addition of TGF-beta 3 to cutaneous rat wounds reduces scarring. J Cell Sci 1995 Mar;108 (Pt 3)(Pt 3):985-1002.

86 Shah M, Foreman D, Ferguson M. Control of scarring in adult wounds by neutralising antibody to transforming growth factor β. The Lancet 1992;339(8787):213-214.

87 Krawczyk WS. A pattern of epidermal cell migration during wound healing. J Cell Biol 1971 May 1;49(2):247-263.

88 Jahoda CA. Induction of follicle formation and hair growth by vibrissa dermal papillae implanted into rat ear wounds: vibrissa-type fibres are specified. Development 1992 Aug;115(4):1103-1109.

89 Winter GD. Formation of the scab and the rate of epithelization of superficial wounds in the skin of the young domestic pig. 1962.

90 Atiyeh BS, Hayek SN. Moisture and wound healing. Journal des Plaies et Cicatrisation 2005;9:7-11.

91 Guo S, Dipietro LA. Factors affecting wound healing. J Dent Res 2010 Mar;89(3):219-229.

92 Rømer J, Bugge TH, Fyke C, et al. Impaired wound healing in mice with a disrupted plasminogen gene. Nat Med 1996;2(3):287-292.

93 Grøndahl-Hansen J, Lund LR, Ralfkiær E, et al. Urokinase-and tissue-type plasminogen activators in keratinocytes during wound reepithelialization in vivo. J Invest Dermatol 1988;90(6):790-795.

94 Holzapfel G, Gasser T, Ogden R. A new constitutive framework for arterial wall mechanics and a comparative study of material models. Journal of elasticity and the physical science of solids 2000;61(1-3):1-48.

95 Holzapfel GA. Determination of material models for arterial walls from uniaxial extension tests and histological structure. J Theor Biol 2006 1/21;238(2):290-302.

96 O'Connell MK, Murthy S, Phan S, et al. The three-dimensional micro- and nanostructure of the aortic medial lamellar unit measured using 3D confocal and electron microscopy imaging. Matrix Biology 2008 4;27(3):171-181.

97 Simpson D, Bowlin G. Tissue-engineering scaffolds: can we re-engineer mother nature? . Expert review of Medical Devices 2006;3(1):9-15.

98 Leong KF, Chua CK, Sudarmadji N, et al. Engineering functionally graded tissue engineering scaffolds. Journal of the Mechanical Behavior of Biomedical Materials 2008 4;1(2):140-152.

99 Simpson D. Dermal templates and the wound-healing paradigm: the promise of tissue regeneration. Expert review of Medical Devices 2006;3(1):471-484.

100 Madurantakam P, Cost C, Simpson D, et al. Science of nanofibrous scaffold fabrication: strategies for next generation tissue-engineering scaffolds. Nanomedicine 2009;4(2):193-206.

101 Ayres C, Jha B, Sell S, et al. Nanotechnology in the design of soft tissue scaffolds: innovations in structure and function. Wiley Interdisciplinary Reviews: Nanomedicine and Nanobiotechnology 2010;1:20-34.

102 Mcmanus M, Boland E, Sell S, et al. Electrospun nanofibre fibrinogen for urinary tract tissue reconstruction. Biomedical materials (Bristol, England) ;2(4):257.

103 Boland ED, Coleman BD, Barnes CP, et al. Electrospinning polydioxanone for biomedical applications. Acta Biomaterialia ;1(1):115-123.

104 Telemeco TA, A., Telemeco TA, et al. Regulation of cellular infiltration into tissue engineering scaffolds composed of submicron diameter fibrils produced by electrospinning. Acta Biomaterialia ;1(4):377-385.

105 Sell SA, M., Sell SA, et al. Electrospun polydioxanone- elastin blends: potential for bioresorbable vascular grafts. Biomedical materials (Bristol, England) ;1(2):72.

106 Lee SJ, Liu J, Oh SH, et al. Development of a composite vascular scaffolding system that withstands physiological vascular conditions. Biomaterials ;29(19):2891-2898.

107 Kidoaki S, Kwon IK, Matsuda T, et al. Mesoscopic spatial designs of nano- and microfiber meshes for tissue-engineering matrix and scaffold based on newly devised multilayering and mixing electrospinning techniques. Biomaterials ;26(1):37-46.

108 Erisken C, Kalyon DM, Wang H, et al. A hybrid twin screw extrusion/electrospinning method to process nanoparticle-incorporated electrospun nanofibres. Nanotechnology ;19(16):165302.

109 Erisken C, Kalyon DM, Wang H, et al. Functionally graded electrospun polycaprolactone and β-tricalcium phosphate nanocomposites for tissue engineering applications. Biomaterials ;29(30):4065-4073.

110 Ayres C, Bowlin GL, Henderson SC, et al. Modulation of anisotropy in electrospun tissue-engineering scaffolds: Analysis of fiber alignment by the fast Fourier transform. Biomaterials ;27(32):5524-5534.

111 Soliman S, Pagliari S, Rinaldi A, et al. Multiscale three-dimensional scaffolds for soft tissue engineering via multimodal electrospinning. Acta Biomaterialia ;6(4):1227-1237.

112 Newton D, Mahajan R, Ayres C, et al. Regulation of material properties in electrospun scaffolds: Role of cross-linking and fiber tertiary structure. Acta Biomaterialia ;5(1):518-529.

113 Ayres CE, Bowlin GL, Pizinger R, et al. Incremental changes in anisotropy induce incremental changes in the material properties of electrospun scaffolds. Acta Biomaterialia ;3(5):651-661.

114 Simpson DG, T., Simpson DG, et al. Modulation of cardiac myocyte phenotype in vitro by the composition and orientation of the extracellular matrix. J Cell Physiol ;161(1):89.

115 McCullen SD, Haslauer CM, Loboa EG. Fiber-reinforced scaffolds for tissue engineering and regenerative medicine: use of traditional textile substrates to nanofibrous arrays. J Mater Chem 2010;20(40):8776-8788.

116 Rho KS, Jeong L, Lee G, et al. Electrospinning of collagen nanofibers: Effects on the behavior of normal human keratinocytes and early- stage wound healing. Biomaterials ;27(8):1452-1461.

117 Liverani L, R., Liverani L, et al. Simple fabrication technique for multilayered stratified composite scaffolds suitable for interface tissue engineering. Materials Science & Engineering A ;557:54-58.

118 McClure MJ, Sell SA, Simpson DG, et al. Tri-layered electrospinning to mimic native arterial architecture using polycaprolactone, elastin, and collagen: a preliminary study. Journal of visualized experiments : JoVE 2011(47).

119 Weinberg C, Bell E. A blood vessel model constructed from collagen and cultured vascular cells. Science 1986 January 24;231(4736):397-400.

120 Woods I, Flanagan TC. Electrospinning of biomimetic scaffolds for tissue-engineered vascular grafts: threading the path. Expert Review of Cardiovascular Therapy 2014 07/01; 2014/08;12(7):815-832.

121 Zhang Y, Ouyang H, Lim CT, et al. Electrospinning of gelatin fibers and gelatin/PCL composite fibrous scaffolds. Journal of Biomedical Materials Research Part B: Applied Biomaterials 2005;72B(1):156-165.

122 Barnes CP, Sell SA, Boland ED, et al. Nanofiber technology: Designing the next generation of tissue engineering scaffolds. Adv Drug Deliv Rev 2007 12/10;59(14):1413-1433.

123 Moroni L, Licht R, de Boer J, et al. Fiber diameter and texture of electrospun PEOT/ PBT scaffolds influence human mesenchymal stem cell proliferation and morphology, and the release of incorporated compounds. Biomaterials 2006;27(28):4911-4922.

124 Lim SH, Mao H. Electrospun scaffolds for stem cell engineering. Adv Drug Deliv Rev 2009;61(12):1084.

125 Justice BA, Badr NA, Felder RA. 3D cell culture opens new dimensions in cell- based assays. Drug Discov Today 2009;14(1):102-107.

126 Pampaloni F, Reynaud EG, Stelzer EHK. The third dimension bridges the gap between cell culture and live tissue. Nature reviews.Molecular cell biology 2007;8(10):839.

127 Boudriot U, Dersch R, Greiner A, et al. Electrospinning Approaches Toward Scaffold Engineering—A Brief Overview. Artif Organs 2006;30(10):785-792.

128 Lannutti J, Reneker D, Ma T, et al. Electrospinning for tissue engineering scaffolds. Materials Science & Engineering C 2007;27(3):504-509.

129 Horst M, Madduri S, Milleret V, et al. A bilayered hybrid microfibrous PLGA– Acellular matrix scaffold for hollow organ tissue engineering. Biomaterials 2013;34(5):1537-1545.

130 Baker BM, Gee AO, Metter RB, et al. The potential to improve cell infiltration in composite fiber- aligned electrospun scaffolds by the selective removal of sacrificial fibers. Biomaterials 2008;29(15):2348-2358.

131 Semwogerere D, Weeks ER. Confocal microscopy. Encyclopedia of biomaterials and biomedical engineering 2005.

132 Whited BM, Hofmann MC, Lu P, et al. Dynamic, nondestructive imaging of a bioengineered vascular graft endothelium. PloS one 2013;8(4):e61275.

133 Jha BS, Colello RJ, Bowman JR, et al. Two pole air gap electrospinning: Fabrication of highly aligned, three-dimensional scaffolds for nerve reconstruction. Acta Biomaterialia 2011 1;7(1):203-215.

134 Kritchevsky SB, Shimakawa T, Tell GS, et al. Dietary antioxidants and carotid artery wall thickness. The ARIC Study. Atherosclerosis Risk in Communities Study. Circulation 1995;92(8):2142.

135 Xu C, Inai R, Kotaki M, et al. Electrospun nanofiber fabrication as synthetic extracellular matrix and its potential for vascular tissue engineering. Tissue Eng 2004;10(7-8):1160.

136 Brown D, Lydon J, McLaughlin M, et al. Antigen retrieval in cryostat tissue sections and cultured cells by treatment with sodium dodecyl sulfate (SDS). Histochem Cell Biol 1996;105(4):261-267.

137 McDougall S, Dallon J, Sherratt J, et al. Fibroblast Migration and Collagen Deposition during Dermal Wound Healing: Mathematical Modelling and Clinical Implications. Philosophical Transactions: Mathematical, Physical and Engineering Sciences 2006;364(1843):1385-1405.

138 Phipps MC, Clem WC, Grunda JM, et al. Increasing the pore sizes of bone-mimetic electrospun scaffolds comprised of polycaprolactone, collagen I and hydroxyapatite to enhance cell infiltration. Biomaterials 2012;33(2):524-534.

139 Szentivanyi AL, Zernetsch H, Menzel H, et al. A review of developments in electrospinning technology: new opportunities for the design of artificial tissue structures. Int J Artif Organs 2011;34(10):986.

140 Blakeney BA, Tambralli A, Anderson JM, et al. Cell infiltration and growth in a low density, uncompressed three-dimensional electrospun nanofibrous scaffold. Biomaterials 2011;32(6):1583-1590.

141 Messerli MA, Graham DM. Extracellular electrical fields direct wound healing and regeneration. Biol Bull 1108;221(1):79.

142 Yang S, Leong K, Du Z, et al. The design of scaffolds for use in tissue engineering. Part I. Traditional factors. Tissue Eng 2001;7(6):679-689.

143 Hollister SJ. Porous scaffold design for tissue engineering. Nature materials 2005;4(7):518-524.

144 Carver W, Molano I, Reaves TA, et al. Role of the α1β1 integrin complex in collagen gel contraction in vitro by fibroblasts. J Cell Physiol 1995;165(2):425-437.

Appendix

Casey Grey, M.S.

CUMULATIVE GPA

- 3.676

RESEARCH PUBLICATIONS

- Exploring the efficacy of cyclic vs static aspiration in a cerebral thrombectomy model: an initial proof of concept study (Journal of NeuroInterventional Surgery, November 2014)
- Gradient fiber electrospinning of layered scaffolds using controlled transitions in fiber diameter (Biomaterials, July 2013)
- Hydrodynamic comparison of the Penumbra system and commonly available syringes in forced-suction thrombectomy (Journal of NeuroInterventional Surgery, March 2013)

INTELLECTUAL PROPERTY

- Impact Aspiration – a novel approach to thrombectomy for ischemic stroke (pursuing full patent)
- Techniques for manufacturing electrospun bandages
- Electromagnetic stator coils replacing permanent magnets on speakers and microphones
- Continuous integrated fiber electrospinning
- Syringe for micro-millimetric delivery utilizing a mechanical expansion aid
- Bulk electrospinning with the ability to uniformly incorporate therapeutic reagents

In addition to the research outlined in the work above, the following papers have been published in peer reviewed journals.

Cyclic Impact Aspiration for Thrombectomy in Acute Stroke: An In Vitro Proof of Concept

Scott Simon, MD [1]

Casey Paul Grey, MS [2]

Trisha Massenzo, BS [2]

David G. Simpson, PhD [3]

P. Worth Longest, PhD [4,5]

[1] Department of Neurosurgery, Pennsylvania State University, Hershey, PA (USA)

[2] Department of Biomedical Engineering, Virginia Commonwealth University, Richmond, VA (USA)

[3] Department of Anatomy and Neurobiology, Virginia Commonwealth University, Richmond, VA (USA)

[4] Department of Mechanical Engineering, Virginia Commonwealth University, Richmond, VA (USA)

[5] Department of Pharmaceutics, Virginia Commonwealth University, Richmond, VA (USA)

Corresponding Author

Casey Paul Grey, MS

Address:

VCU Department of Biomedical Engineering

401 West Main Street

P.O. Box 843067

Richmond, Virginia, 23284-3067

Abstract

Background and Purpose: Current technology for endovascular thrombectomy in ischemic stroke utilizes static loading and is successful in approximately 85% of cases. Through the application of cyclic loading we explore the engineering principle of fatigue as the basis for a new thrombectomy technology.

Methods: Impact Aspiration is a novel aspiration technique involving cyclic rather than static aspiration pressure. A system was created using a Penumbra Aspiration System, three-way valve, and Penumbra 5max catheter. Synthetic clot was aspirated in a flow model at different frequencies and using different fluid mediums. Success or failure of clot removal and time were recorded. All statistical analyses were based on either a one-way or a two-way analysis of variance, Holm-Sidak pair-wise multiple comparison procedure (alpha = 0.05).

Results: Cyclic loading outperformed static loading in overall clot removal and removal speed ($P<.001$). Within cyclic loading, Max Hz frequencies (~6.3 Hz) cleared clots faster than 1 Hz ($P<.001$) and 2 Hz ($P=.024$). Loading cycle dynamics (specific pressure waveforms) affect speed and overall clearance ($P<.001$). Water as the aspiration medium is more effective at clearing clots than air ($P=.019$).

Conclusion: Cyclic loading significantly outperformed static loading in both speed and overall clearance of synthetic clots in our experimental model. Within cyclic loading, efficacy is improved by increasing cycle frequency, utilizing specific pressure cycle waveforms, and using water rather than air as the aspiration medium. We aim to apply these results and principles to more complicated physiological flow models to further explore this method.

Introduction

Thrombectomy devices for use in ischemic stroke have undergone a step-wise evolution as each generation of technology becomes more effective without increasing complications. Despite progress, the best thrombectomy technology currently only achieves recanalization in approximately 85% of cases.[1] In the interest of positive patient outcomes after ischemic events, the continued development of thrombectomy technology should be encouraged as it is necessary until successful recanalization is assured in all cases.[2] This study represents another step in the evolution of thrombectomy technology towards the goal of 100% recanalization.

Current thrombectomy techniques focus on applying endovascular disruptive forces to facilitate the removal of occluding thrombi. This can involve mechanical entrapment and extraction of clots via deployable mesh-like device (e.g. stent retrievers[3]) or, in suction thrombectomy (the topic of this study), an aspiration source (e.g. pump, large-gauge syringe[4-7]) is used to dislodge clots from the vasculature so they can be removed via a catheter. While these techniques are moderately successful,[8] we propose a transition from static to cyclic forces in thrombectomy. In this way we can subject clots to material fatigue, reducing the required load-to failure (theoretically enabling the removal of more-entrenched clots) and the time-to-failure at a specific load (theoretically reducing the time to reperfusion[9,10]).

Simply defined by Wiley, "Fatigue refers to the modification of the properties of a material due to the application of stress cycles whose repetition can lead to fracture."[11] Unlike most real-

world examples of fatigue, such as the de Havilland Comet 1 plane crash in 1954 where material fatigue was unintended and undesirable,[12] increasing the likelihood of clot failure through fatigue mechanisms is exactly the goal of this study.

Knowing that a clot is simply an occlusive material possessing measurable material properties (albeit dynamic ones)[13], and that cyclic loading facilitates material failure,[11,12] we hypothesized that the introduction of cyclic aspiration forces in suction thrombectomy would measurably improve aspiration performance compared to the static forces characteristic of current suction thrombectomy techniques.[6] Moreover, as failure in fatigue is a function of total load cycles,[14] we hypothesized that increased frequencies would lead to increased treatment efficacy. To test our hypothesis, we evaluated the efficacy of novel cyclic suction thrombectomy force profiles against the current static suction thrombectomy force profile through their performance aspirating synthetic clots in a flow model.

Methods

The Cyclic Impact Aspiration Technique

The model, depicted in Figure 1, involved performing cyclic impact aspiration by placing a three-way valve (Harvard Apparatus, Holliston, Massachusetts, USA) in between a vacuum source (Penumbra aspiration pump, Penumbra, Alameda, California, USA) and the catheter (Penumbra 5Max reperfusion catheter, Penumbra, Alameda, California, USA) to establish open continuity between the vacuum source, the catheter tip, and air (the aspiration medium) when the valve was opened. Temporarily closing the valve to air (e.g. with index finger) allowed the pump to establish a vacuum at the catheter tip. Subsequently removing the finger reopened the system to air and rapidly diminished the vacuum at the catheter tip. Impact aspiration is performed by repeatedly opening and closing the valve to air so that cyclic pressure profiles are developed at the catheter tip. Additional tests were performed by changing the aspiration medium to water (incompressible fluid) rather than air (compressible fluid). This was accomplished by submerging the three-way valve in water. The system was primed with the aspiration medium before experimentation.

Additionally, using this model allows modification of not only frequency but also the pressure profile. We describe two general ways to cycle aspiration pressure at a specific frequency. Down-cycling (DC) involves a brief pressure-relieving impulse in each cycle with a majority of time spent at maximum treatment pressure (Results, Figure 2B-C). Up-cycling (UC) involves a brief pressurizing impulse in each cycle with a majority of time spent at minimum treatment

pressure (Results, Figure 2D-E). At frequencies higher than 2 Hz the pressure plateau characteristic of DC aspiration was not possible via manual control, thus we considered all aspiration above 2 Hz to be UC as it consisted of very brief pressurization impulses.

Clot Removal Flow Model Analysis

Synthetic polyurethane clots (Concentric Medical, Mountain View, California, USA) were extruded with a cylindrical template cut to a specific clot size (see Results) using Traceable Digital Calipers (Control Company, Friendswood, Texas, USA). They were then placed in a flow model consisting of a Penumbra 5Max reperfusion catheter (1.37mm tip ID) inside hard plastic tubing submerged in water. The clots were positioned near the catheter tip and exposed to either suction alone (Penumbra aspiration pump) or cyclic aspiration via our Impact Aspiration technique. The test was performed until either the clot was removed or five minutes had elapsed. If the clot was not cleared within five minutes, the standard dwell time of current stent retrievers, the trial was considered unsuccessful. It is important to note that the synthetic clot changes in consistency (and, presumably, mechanical properties) within several days after opening, therefore only freshly opened packages were used in experimentation.

Aspiration Pressure Analysis

Pressure profiles were generated by placing an Equus 3620 Innova Vacuum Gauge (Equus Products, Irvine, California, USA) distal to the three-way valve and recording the pressures generated during static aspiration and Impact Aspiration at frequencies of 1 and 2 Hz as well as a third group labeled "Max Hz" where the experimenter cycled the system as fast as possible. The

"Max Hz" category was necessary to capture Impact Aspiration performance at higher frequencies while acknowledging that accurately reproducing frequencies above 2 Hz was not possible with our manual technique. The actual frequency for the "Max Hz" trials was determined by dividing the number of cycles by the time elapsed. Limitations in our ability to manually control the pressure cycling prevented us from testing a wider range of frequencies.

After noticing the increased efficacy of the UC Impact Aspiration technique, and with limited synthetic clot available, we focused our efforts on obtaining as much data on the UC technique in order to facilitate statistical analysis of the results.

Statistical Analysis

All statistical analyses were based on either a one-way (static loading vs. cyclic loading and UC Impact Aspiration clot clearance trials) or two-way analysis of variance (all other analyses), Holm-Sidak pair-wise multiple comparison procedure (alpha = 0.05).

Results

Cyclic loading: Cycle Dynamic Details

Pressure cycle dynamics for each system are approximated in Figure 2. Figure 2A and the corresponding open "O" and closed "C" markings on Figures 2B-D shows how modulation of the three-way valve creates the pressure profiles used in this study. The Penumbra Pump acting alone, provided an adequate pump-down time, rapidly creates and maintains a vacuum (Figure 2B).[6] Down-cycling (DC) and up-cycling (UC) Impact Aspiration are detailed in Figure 2C-D.

Aspiration Pressure Dynamics

The Penumbra System alone creates a rapidly-developing static pressure curve that reaches a peak value of -622 mmHg (-24.5 inHg). Impact Aspiration creates a dynamic pressure curve where the pressure cycles between a maximum and minimum value at a specific frequency (maximum and minimum relating to the magnitude of pressure). Impact Aspiration at 1 Hz cycles between -605 mmHg and 0 mmHg (between -23.8 inHg and 0 inHg). Impact Aspiration at 2 Hz cycles between -559.0 mmHg and 0 mmHg (between -22.0 inHg and 0 inHg). Impact Aspiration at Max Hz (~6.3 Hz) cycles between -480 mmHg and -127 mmHg (between -18.9 inHg and -5.0 inHg). The relationship between frequency and pressure differential for the three Impact Aspiration values is remarkably linear with linear curve-fitting yielding an equation of $y = 47.654x - 653.4$ with an r^2 value of 1.

Clot Sizing

By systematically increasing the synthetic clot diameter until the Penumbra System could no longer successfully clear the clots from the flow model we created a stroke model in which immediate suction alone would be an insufficient treatment. Synthetic clots with a diameter of 2.16 mm and a length of 3 mm satisfied the criteria and were used in all experimentation.

Strategy for Analyzing Aspiration Success

Examining the data as a whole brings to light the complex interplay between the variables (static aspiration, cyclic aspiration, and within cyclic aspiration, frequency, aspiration medium, and pressure waveform) and the ultimate results (overall clot clearance rate and clot clearance time). In the following sections we systematically examine how each individual variable affects the experimental results.

Static Loading vs. Cyclic Loading

Aspiration with the Penumbra pump alone failed to clear a single clot (n=10) whereas the combined clearance rate of Impact Aspiration was 91.43% (64 cleared, n=70). Impact Aspiration was significantly better at clearing clots from the flow model compared to static aspiration with the Penumbra pump ($P<.001$).

Cyclic loading: Frequency Comparison

Impact Aspiration had successful clearance rates of 84% (1 Hz, n=25), 100% (2 Hz, n=25), and 90% (Max Hz, n=20) and clearance times of 35.1s SD 22.8s (1 Hz, n=21), 40.7s SD 55.4s (2 Hz, n=25), and 7.8s SD 6.8s (Max Hz, n=18). Aspirating at Max Hz was significantly faster at clearing clots compared to both 1 Hz (P<.001) and 2 Hz (P=.024). There were no significant differences between frequencies when considering general ability to clear clots from the flow model.

Cyclic loading: Aspiration Medium Comparison

When air was used as the aspirating medium Impact Aspiration had an overall clearance rate of 85% (n=40) and an average clearance time of 34.7s SD 49.3s (n=34). When water was used as the aspirating medium Impact Aspiration had an overall clearance rate of 100% (n=30) and an average clearance time of 23.8s SD 22.7s (n=30). Impact Aspiration using water as the aspirating medium was significantly more effective at clearing clots compared to when air was used as the aspirating medium (P=.019). There were no significant differences between the two aspirating mediums when considering clearance time.

Cyclic loading: Cycle Dynamics Comparison

Using down-cycling (DC) pressure profiles in Impact Aspiration resulted in a clearance rate of 60% (n=10) and an average clearance time of 80.7s SD 94.8s (n=6). Using up-cycling (UC) pressure profiles resulted in a clearance rate of 96.67% (n=60) and an average clearance time of 24.3s SD 24.8s (n=58). Compared to DC, UC pressure profiles were both significantly more

effective in general ability to clear clots from the flow model (P<.001) and significantly faster at clearing the clots from the flow model (P<.001).

UC Impact Aspiration Clot Clearance Trials

Max Hz cycling with water as the aspiration medium was significantly faster than 1 Hz cycling with either air (P=.015) or water as the aspiration medium (P=.025). While clearance time clearly trended downwards with increasing aspiration frequency, no other differences were found to be statistically significant (Figure 3).

Discussion

From our results we believe that cyclic loading can supplant static loading as the base aspiration profile for the treatment of ischemic stroke. In the interest of preventing the distal migration of thrombi, Impact Aspiration would have to be performed either in conjunction with continuous aspiration or as a standalone treatment with a minimum frequency such that a vacuum is maintained throughout testing. In this study ~6.3 Hz (Max Hz) was the only frequency that accomplished this as both 1 Hz and 2 Hz had minimum pressures of 0 mmHg. Implementing a pressure-controlling device would allow flexibility in aspiration frequency due to the increased control over minimum pressure. Additionally, utilizing an aspiration medium that was under a low vacuum (e.g. -50 mmHg) rather than atmospheric pressure would ensure that treatment operated under continuous vacuum. As with current static aspiration techniques, we believe cyclic aspiration would pair successfully with supplemental treatment methods such as the use of a separator wire.

Cyclic vs. Static Loading

While the dips in the pressure-time curve (Figure 2) show cyclic loading delivers less total force to the clot compared with static loading, we showed that cyclic loading is superior to static loading in clearing clots from our flow model ($P<.001$). The discrepancy between total force delivered and experimental outcome indicates that the dynamics of loading play a significant role in the success of the procedure. The rest of the discussion will focus on the different aspects of cyclic loading and how they affect clot clearance.

Frequency

Figure 3 clearly shows that increasing frequency of Impact Aspiration decreases clot clearance time. While Max Hz cycling was not 100% successful in this study (it's worthwhile to note that all clearance failures occurred with air as the medium), the significant decrease in clot clearance time is a good indicator that increasing frequency is the correct path to more effective treatments. We believe that additional dimensions of frequency and amplitude modulation may be added to this technique in which their values are temporally adjusted depending on either the clinical scenario or more advanced understanding of clot fatigue failure mechanisms.

UC vs. DC

The significantly greater efficacy of UC compared to DC Impact Aspiration may shed light on the mechanism by which cyclic loading outperforms static loading. UC differs from DC Impact Aspiration in that its pressure dynamics are characterized by two rapid perturbations (pressure on and off) with virtually no static loading between them. DC Impact Aspiration, on the other hand, has a relatively long static loading period between its two perturbations. In this study it appeared that the prolonged static force actually decreased the efficacy of the technique, thus, we believe the mechanism of successful clot disruption lies in the perturbations applied to the clot, not in the static force.

Air vs. Water

Water as an aspiration medium proved to be significantly more effective at clearing clots compared to air. This could potentially be explained by the incompressibility of water (whereas air is compressible). Assuming a static environment, as the pressure is cycled on and off, the rise and fall in applied pressure at the catheter tip have a logical set of properties which likely affect performance; first, the cycle is initiated by closing the valve to the aspiration medium, thus initiating pressure – in the case of air this involves a change from a relatively non-compressed state (at atmospheric pressure) to a decompressed state as aspiration pressure is applied and the gas expands under vacuum. This decompression should be seen in a pronounced ramping of the pressure-time curve at the beginning of the cycle (effectively buffering the aspiration force) followed by a sharp increase in pressure as the air decompresses fully (see Figure 4 – Air Curve). When air is replaced with water this ramping property is eliminated because of water's incompressible nature. The pressure-time curve for water should skip the ramp and progress immediately to the sharp increase in pressure as soon as the cycle is initiated (i.e. there is no force buffer, see Figure 4 – Water Curve). Likewise, at the end of the cycle as the pressure is relieved, the initial ramp should be present in air and absent in water. These properties give air and water different "perturbation curves" with air having a "soft" perturbation curve (ramping on and off) and water having a "sharp" perturbation curve (immediately transitioning to a steeply-sloped on and off). We believe that these different perturbation curves are responsible for the differing efficacies of the aspiration mediums. While these pressure-time curve properties are theoretical, they do follow logical mechanics and should be detectable with moderately sensitive equipment in future studies. It is important to note that the system must be "primed" with each aspiration medium before experimentation.

Impact Aspiration as a departure from current techniques

A technique that bears some similarity to the topic of this study is ultrasound augmented fibrinolysis. The ultrasonic oscillations in this technique, delivered transcranially or via catheter, are designed to increase the penetration of fibrinolytic agents into the clot so that the clot breaks up and flows distally.[15-17] The benefits of ultrasound augmented fibrinolysis, however, may not outweigh the increased risk of hemorrhage.[15] Comparatively, Impact Aspiration employs much lower frequency and higher amplitude oscillations, produced by altering the aspiration pressure profile, aimed at mechanically dislodging and disrupting the clot so that it can be aspirated from the vessel.

Risks associated with Impact Aspiration

There may be concerns regarding increased risk of hemorrhage, especially in light of reports of increased hemorrhage after the application of ultrasound in stroke treatment.[15] While these risks are possible, we point out that the risks associated with ultrasound treatment appear to be frequency dependent, with kHz frequencies posing a much larger risk than MHz.[18] On the other end of the frequency spectrum, physiological frequencies of ~1-3 Hz are part of normal circulation where the natural elasticity of vessel walls allows them to safely expand and contract with the pressure fluctuations. We hypothesize that there is a range of unsafe frequencies where the risk of compromising vessel walls is increased, leading to increased rates of hemorrhage. This unsafe range (currently accepted as in the kHz range[18]) would be characterized by frequencies too high to allow the vessel walls to elastically accommodate the perturbations, rendering their deformation as plastic, and amplitudes large enough to cause significant

mechanical damage. Above this unsafe frequency range (e.g. MHz frequencies) the amplitudes are not large enough to cause significant wall damage, accounting for the decreased rate of hemorrhage, though these frequencies are associated with increased thermal tissue damage.[19] Impact Aspiration utilizes low frequency mechanical perturbations, likely well below 50 Hz, which should not exceed local elastic limits and therefore should not significantly increase the risk of hemorrhage. Alternately it is possible that high frequency vibrations may lie within the harmonic resonance frequencies of the surrounding blood vessels. This could result in unintentional amplification of the source signal[20] to magnitudes that are high enough to cause tissue damage. While testing would have to confirm that the perturbations associated with Impact Aspiration did not increase the risk of hemorrhage, low frequency perturbations should be similar enough to physiological circulation frequencies so as not to result in elevated rates of hemorrhage.

Next steps with this technology

In this study we have taken the first steps in exploring Impact Aspiration as a new thrombectomy technique. We've shown that cyclic loading outperforms static loading and that the frequency of loading, the dynamics of each pressure cycle, and the aspiration medium all affect clot clearance. In order to bring this technology closer to clinical translation, we believe there are several steps that still need to be taken. A mechanical pressure-modulating device needs to be constructed such that the frequency, amplitude, and pressure cycle dynamics can be precisely controlled. Ideally this device would be simple, cheap, and purely mechanical so that it could be easily and cost-effectively added to existing aspiration equipment. Concept pressure-modulating devices

are shown in Figure 5 and Supplementary Figures I-III (please see http://stroke.ahajournals.org for access to supplementary figures).

This study proves that our novel Impact Aspiration device significantly outperform static aspiration in the clearance of synthetic clots from our flow model. With plans for future testing in place we believe we can translate these results to physiological models of occlusive blood clots.

Conclusion

We demonstrate that cyclic loading with our Impact Aspiration technique significantly outperforms static loading with the Penumbra pump at clearing synthetic clots in an experimental model. Within our Impact Aspiration technique, aspirating at a higher frequency (~6.3 Hz vs. 2 Hz) and with water as the aspirating medium is the most effective way to clear synthetic clots from the flow model.

Acknowledgements

The authors would like to thank Paul Grey for discussions on harmonics.

References

1. Dávalos A, Pereira VM, Chapot R, Bonafé A, Andersson T, Gralla J. Retrospective multicenter study of solitaire FR for revascularization in the treatment of acute ischemic stroke. *Stroke*. 1210;43(10):2699.

2. Fiehler J, Söderman M, Turjman F, et al. Future trials of endovascular mechanical recanalisation therapy in acute ischemic stroke patients: A position paper endorsed by ESMINT and ESNR : Part I: Current situation and major research questions. *Neuroradiology*. 1212;54(12):1293.

3. Bösel J, Hacke W, Bendszus M, Rohde S. Treatment of acute ischemic stroke with clot retrieval devices. *Curr Treat Options Cardio Med*. 1206;14(3):260-272.

4. Kreusch AS, Psychogios M, Knauth M. Techniques and Results—Penumbra aspiration catheter. *Techniques in Vascular and Interventional Radiology*. 1203;15(1):53-59.

5. Kang D, Hwang Y, Kim Y, Park J, Kwon O, Jung C. Direct thrombus retrieval using the reperfusion catheter of the penumbra system: Forced-suction thrombectomy in acute ischemic stroke. *AJNR.American journal of neuroradiology*. 1102;32(2):283.

6. Simon SD, Grey CP. Hydrodynamic comparison of the penumbra system and commonly available syringes in forced-suction thrombectomy. *Journal of NeuroInterventional Surgery*. 2013.

7. The penumbra pivotal stroke trial: Safety and effectiveness of a new generation of mechanical devices for clot removal in intracranial large vessel occlusive disease. *Stroke*. 0908;40(8):2761.

8. Barreto AD, Alexandrov AV. Adjunctive and alternative approaches to current reperfusion therapy. *Stroke*. 1202;43(2):591.

9. Saver JL. Time is brain-- quantified. *Stroke*. 0601;37(1):263.

10. Khatri P, Abruzzo T, Yeatts SD, Nichols C, Broderick JP, Tomsick TA. Good clinical outcome after ischemic stroke with successful revascularization is time-dependent. *Neurology*. 0929;73(13):1066.

11. *Fatigue of materials and structures fundamentals.* London : Hoboken, NJ: London : ISTE ; Hoboken, NJ : John Wiley; 2010.

12. Withey PA. Fatigue failure of the de havilland comet I. *Eng Failure Anal*. 1997;4(2):147-154.

13. Brown AEX, Litvinov RI, Discher DE, Purohit PK, Weisel JW. Multiscale mechanics of fibrin polymer: Gel stretching with protein unfolding and loss of water. *Science*. 0807;325(5941):741-744.

14. Mršnik M, Slavič J, Boltežar M. Frequency-domain methods for a vibration-fatigue- life estimation – application to real data. *Int J Fatigue*. 1302;47:8-17.

15. Kelley RE, Martin-Schild S. Ischemic stroke: Emergencies and management. *Neurol Clin*. 1202;30(1):187.

16. Alexandrov AV. Ultrasound enhancement of fibrinolysis. *Stroke*. 0903;40(3):S107.

17. Saqqur M, Uchino K, Demchuk AM, et al. Site of arterial occlusion identified by transcranial doppler predicts the response to intravenous thrombolysis for stroke. *Stroke*. 0703;38(3):948.

18. Barlinn K, Barreto AD, Sisson A, et al. CLOTBUST-hands free: Initial safety testing of a novel operator-independent ultrasound device in stroke-free volunteers. *Stroke*. 1306;44(6):1641.

19. Monteith S, Sheehan J, Medel R, et al. Potential intracranial applications of magnetic resonance-guided focused ultrasound surgery. *J Neurosurg*. 1302;118(2):215.

20. Gao F, Zheng Y, Feng X, Claus-Dieter Ohl. Thermoacoustic resonance effect and circuit modelling of biological tissue. *Appl Phys Lett*. 0211;102:063702.

Figure Legend

Figure 1. Aspiration flow schematic. For static load aspiration the three-way valve was modified so that continuity existed only between the catheter and the aspiration source. For cyclic load aspiration the three-way valve was modified so that open continuity existed between the catheter, the aspiration medium, and the aspiration source. In this way it was possible to manually cycle the aspiration pressure at the catheter tip by repeatedly covering and uncovering the valve port open to the aspiration medium. For this study we simply did this with our finger.

Figure 2. Examples of the aspiration pressure profiles used in this study. A) Valve positions used to create dynamic pressure profiles. B) The Penumbra pump produced a static pressure profile where the aspiration pressure was attained rapidly and diminished only when the pump was turned off. C, D) The two dynamic pressure profiles representing the evolution of the Impact Aspiration technique. C) The first, called down-cycling (DC), involves brief pressure-relieving impulses. D) The second dynamic pressure profile, called up-cycling (UC), involves brief pressurizing impulses. While 1 Hz is used as an example here, it is worthwhile to note that the purpose of the graph is to highlight the differences between pressure waveforms, not to outline a preferred aspiration frequency.

Figure 3. UC Impact Aspiration clot clearance times with standard error bars. A one-way analysis of variance was used to determine the relationship between different UC Impact

Aspiration groups and their performance with regard to clot clearance time. Significant differences are marked on the figure with * and †.

Figure 4. Theoretical perturbation curves when using air or water as the aspiration medium. Like in Figure 2, "C" and "O" represent the points in a cycle where the valve is closed (initiating pressure) and opened (relieving pressure), respectively.

Figure 5. Concept Impact Aspiration device designs. The top device employs an electromagnetic pressure controlling mechanism while the bottom device employs a simple mechanical pressure controlling mechanism. For additional details please see http://stroke.ahajournals.org.

Figures

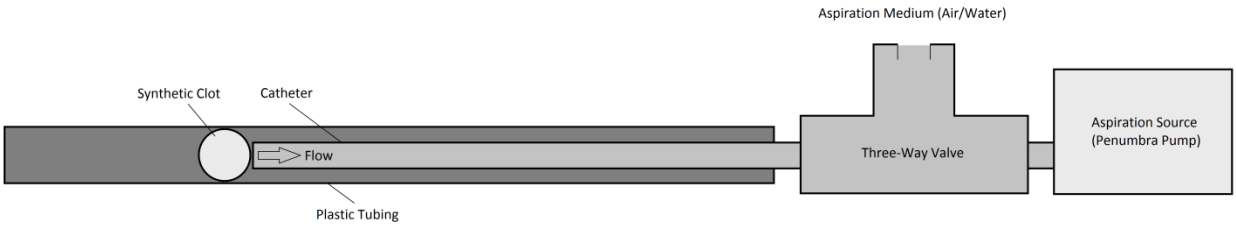

Figure 1

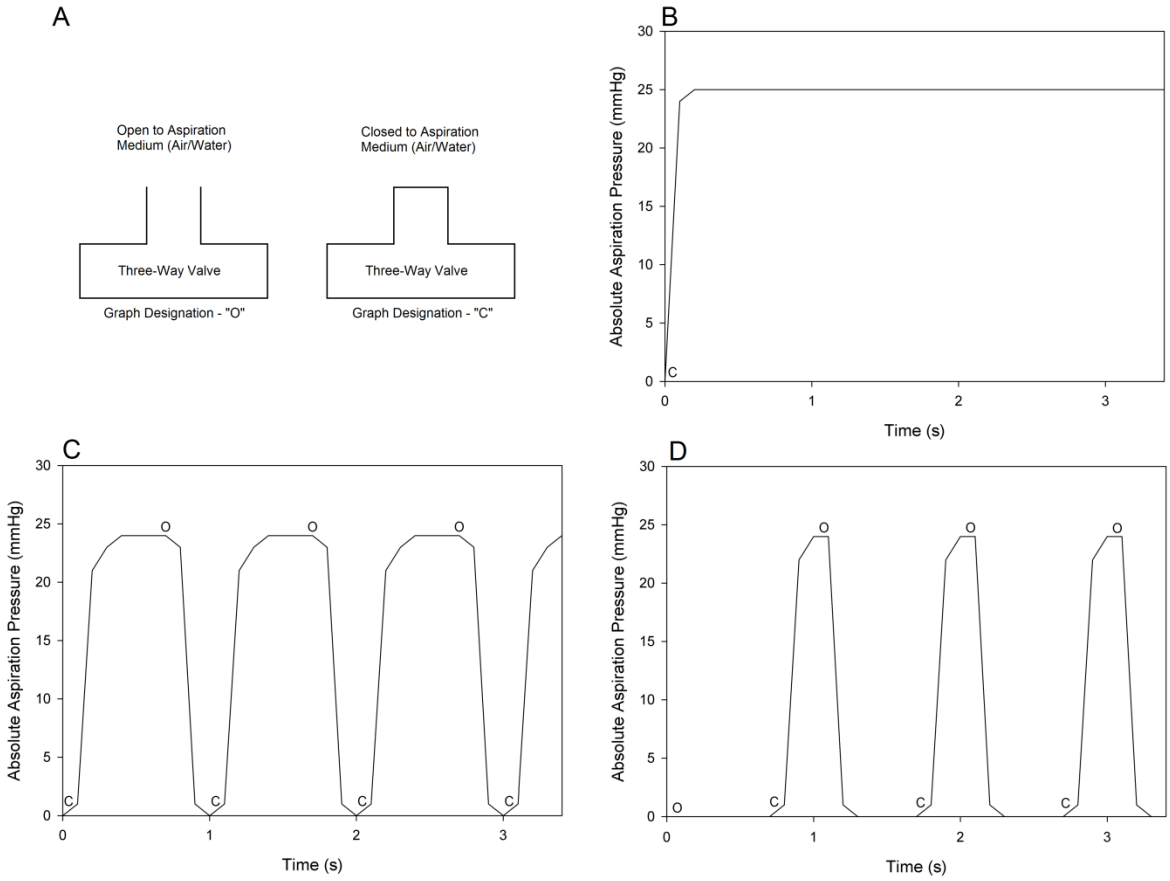

Figure 2

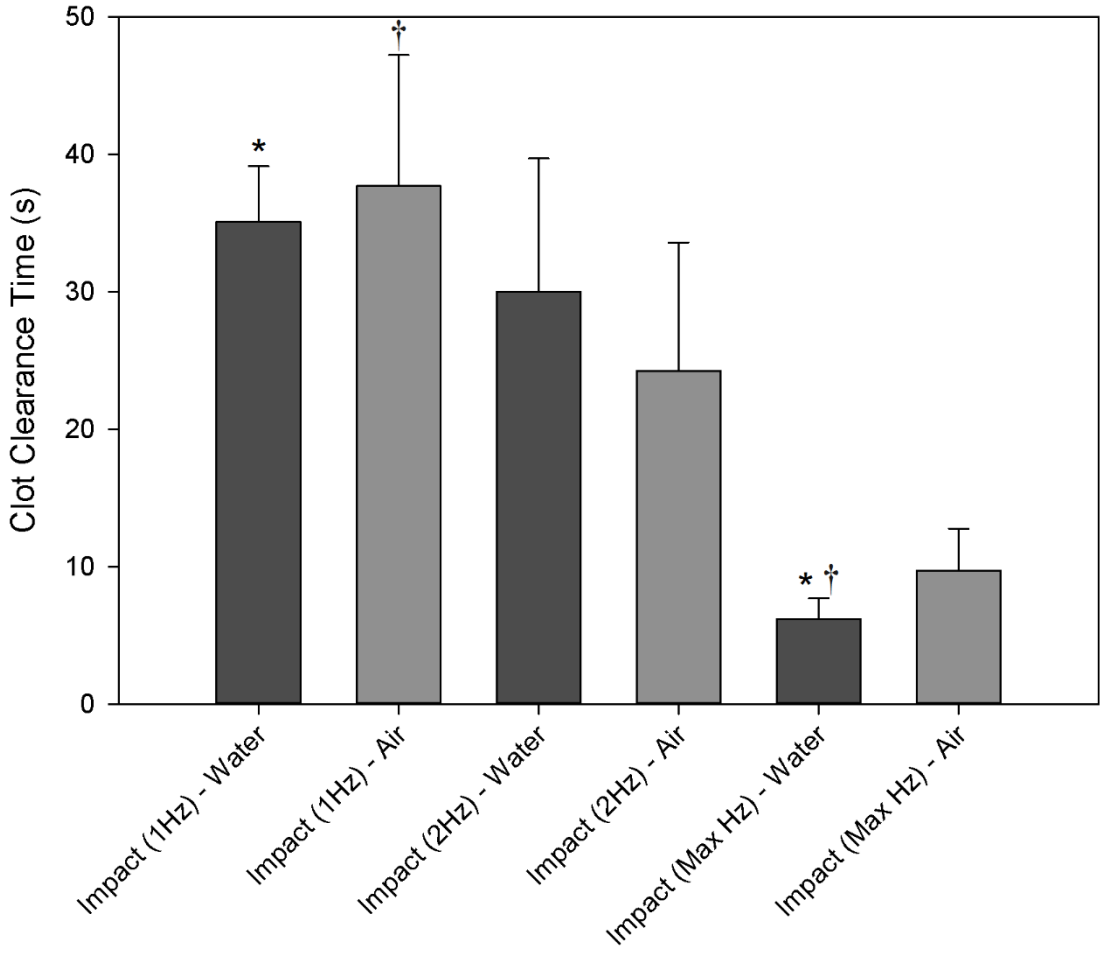

Figure 3

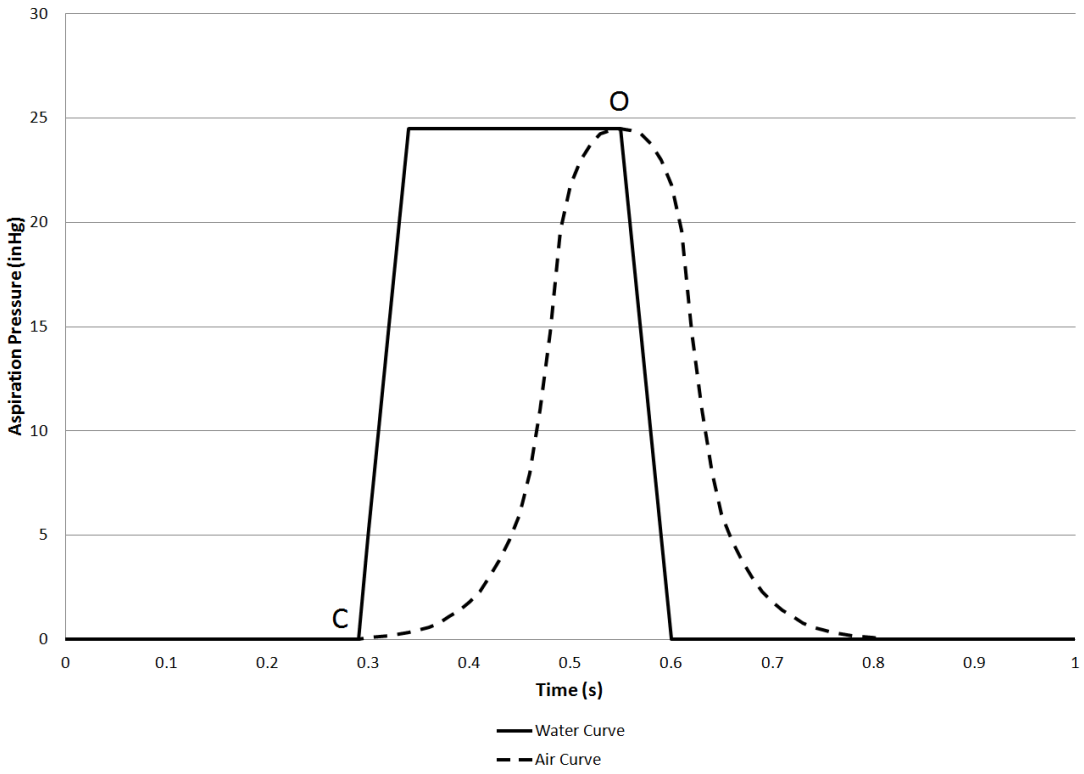

Figure 4

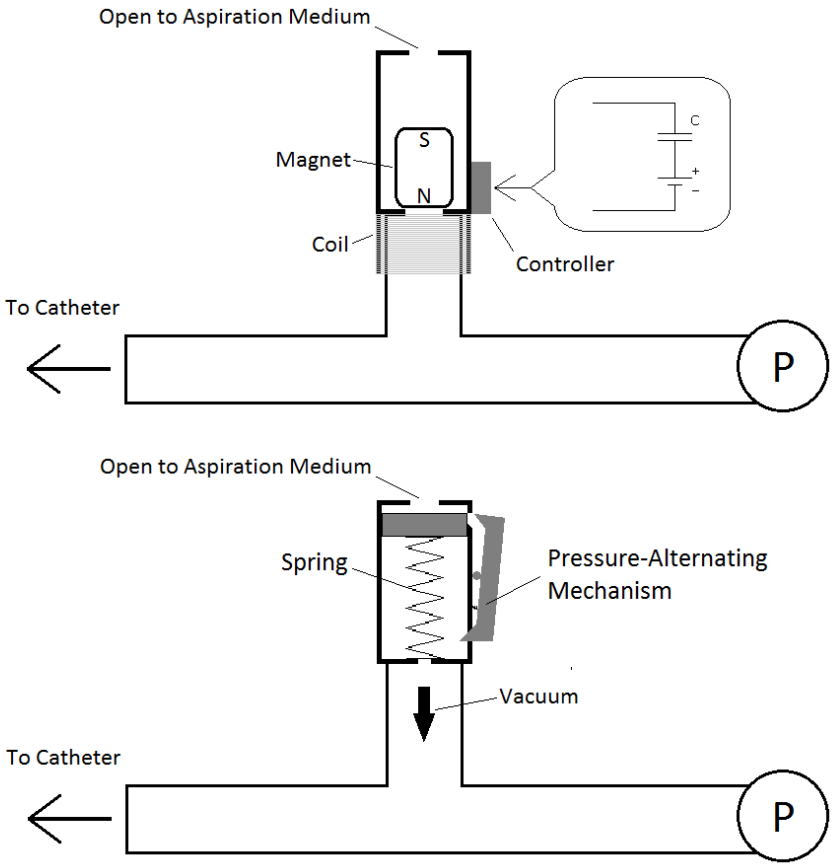

Figure 5

Hydrodynamic Comparison of the Penumbra System and Commonly Available Syringes in Forced-Suction Thrombectomy

Scott Simon, MD[1]

Casey Grey, M.S.[2]

[1] VCU Department of Neurosurgery, Richmond, VA (USA).

[2] VCU Biomedical Engineering Graduate School, Richmond, VA (USA).

Corresponding Author

Scott Simon, M.D.

417 North 11th Street, Sixth Floor, Richmond, Virginia 23298

ssimon3@mcvh-vcu.edu

Phone: (804) 828-9165

Fax: (804) 828-0374

This research was funded by an unrestricted educational grant by Covidien (Mansfield, MA) to the Virginia Commonwealth University Department of Neurosurgery.

Abstract

Background: The Penumbra System (PS) uses a coaxial separator and continuous extracorporeal suction to remove a clot from a cerebral artery. Forced-Suction Thrombectomy (FST) involves aspirating clots through the same reperfusion catheter using only a syringe, decreasing procedure time and supplies needed. Objective: Our goal is to evaluate multiple combinations of catheters and syringes to determine the optimal pairing for use in FST. Methods: Tests were performed using both the PS and syringes to aspirate water through Penumbra 0.041 inch (041), 4Max, 0.054 inch (054), and 5Max reperfusion catheters and a shuttle sheath. Dynamic pressure and flow at the catheter tip were calculated from the fill times for each system. Static pressure and force for each aspiration source were determined with a vacuum gauge. Results: All syringes provided significantly higher dynamic pressure at the catheter tip compared to the PS ($p < .001$). Increasing syringe volume significantly increased static pressure ($p < .001$). Both flow and aspiration force significantly increase with catheter size ($p < .001$). Cases are presented to demonstrate the clinical value of the laboratory principles.

Conclusion: Maximizing static and dynamic pressure when performing FST is achieved by aspirating with a syringe possessing both the largest volume and the largest inlet diameter available. Maximizing aspiration force and flow rate is achieved by using the largest catheter possible.

Introduction

Forced-Suction Thrombectomy is a modification to the Penumbra System and, like the Penumbra System, is used as a mechanical recanalization method for ischemic stroke and as a rescue therapy in embolization procedures.[1,2] In Forced-Suction Thrombectomy, a syringe is directly connected to the proximal hub of a reperfusion catheter with its distal end either on or near a vessel occlusion.[1] The syringe plunger is forcibly pulled to generate a negative pressure with the goal of restoring vessel patency by either sucking the occluding element into the catheter or by maintaining enough of a vacuum so as to wedge the occluding element onto the distal catheter tip which can then manually removed from the vessel.

While several recent studies have shown that both the Penumbra Aspiration System and Forced-Suction Thrombectomy are safe and efficacious in the treatment of ischemic stroke, they have also alluded to the fact that Forced-Suction Thrombectomy represents a quicker and more flexible treatment option.[1,3,4] Because of its minimalistic design, Forced-Suction Thrombectomy provides advantages in preparation time and time to revascularization. Additionally, if Forced-Suction Thrombectomy fails, it can quickly and easily be converted to the Penumbra System.[1,3]

The current logic in syringe selection for Forced-Suction Thrombectomy is that larger syringes are preferred over smaller ones due to their elevated “suction power”,[1] however, no mechanical analysis of the aspiration pressures developed with different syringes exists.

Furthermore, the listed aspiration pressure of the Penumbra System (>20 in Hg) does not fully represent the actual aspiration pressure developed at the catheter tip (see results).

This study was designed to analyze current aspiration techniques for the treatment of ischemic stroke with the goal of determining working pressures at the catheter tip in order to optimize syringe and catheter selection in Forced-Suction Thrombectomy. Through our ex vivo model we analyzed different aspiration sources paired with different reperfusion catheters and a shuttle sheath, determining fluid flow and then calculating maximum dynamic pressure, or pressure due to fluid velocity, achieved in each scenario. In contrast to dynamic pressure developed in full-flow scenarios, we also analyzed the static pressure, or pressure in zero velocity (no-flow) situations, developed with each aspiration source. From the static pressure data we determined the actual aspiration force applied to the occlusion. While the factors involved in the successful recanalization of occluded vasculature extend beyond applied aspiration pressure, a more-informed approach to suction thrombectomy is achieved by understanding the relationship between aspiration source, catheter size, and the subsequent pressure and force developed at the occlusion site. Therefore our goal in this study is to provide information about the working pressures and forces achieved through various aspiration techniques in an effort to highlight the importance of how these variables may affect treatment outcomes. This study also includes clinical examples that demonstrate the applicability and versatility of the principles in question.

Methods

Water was used as the fluid of choice because of its accessibility and similar fluid properties to blood. With a density of 1000 kg/m^3, water nearly matches the density of whole blood.[5] Additionally the specific flow rates in this study are high enough to ignore non-linear hemorheological fluid properties and the vessel diameters large enough to use the assumption of blood as a continuous fluid, further validating water as the fluid of choice.[6]

One experimental setup for this study involved aspirating water through commonly used catheters (041, 4Max, 054, 5Max, and a shuttle sheath) via different aspiration sources. The inner diameters of the distal catheter tips were experimentally measured and used as the diameter variable in the fluid velocity calculation. Inner diameter values were as follows: 041/4Max catheters – 1.04 mm, 054/5Max catheters – 1.37 mm, and shuttle sheath – 2.4 mm. As the experimental unknown in this study, the suction element was represented by either the Penumbra Aspiration System or common syringes ranging in volume from 1 mL to 60 mL. Experiments were performed in the following manner:

Dynamic Pressure Analysis - Penumbra Aspiration System

Each catheter was connected to the Penumbra Aspiration System (Penumbra, Inc., Alameda, CA) with the distal catheter placed in a volume of water. The Penumbra system was turned on and allowed to equilibrate to working pressure (26.5 inHg). Once equilibrium aspiration pressure

was achieved (approximately 2.5 minutes) the time to aspirate either 100 mL (041, 4Max, and 5Max catheters) or 250 mL (054 catheter and shuttle sheath) was measured and recorded (n=3).

Dynamic Pressure Analysis - Syringes

Before each test run the catheters were primed by filling the test syringe with water and dispensing it into the catheter so that no air remained in the system. 3, 5, 10, 20, 30, and 60 mL BD syringes (Becton, Dickinson and Company, Franklin Lakes, NJ) and 3, 6, 10, and 20 mL Medallion syringes (Merit Medical Systems, Inc., South Jordan, Utah) were tested by aspirating maximally (rapidly pulling the plunger to the highest volume marking) through the test catheter, the end of which was placed in a volume of water. The time to aspirate the full syringe volume was measured and recorded (n=10). Some syringes were not used because the fill time could not be accurately recorded, this occurred more frequently when aspirating with smaller syringes and larger catheters (e.g. BD 3 mL syringe and shuttle sheath which had a fill time well under 1 second). The main difference between the BD and Medallion syringes is their respective inlet diameter. Medallion syringes have inlet diameters measuring 2.34 mm while BD syringes have inlet diameters measuring 1.78 mm.

Flow rate (mL/s) was determined by dividing the flow volume by the aspiration time. The fluid velocity at the distal catheter (m/s) was determined by dividing the flow rate by the distal catheter cross-sectional area. In this study the dynamic pressure at the distal catheter (catheter tip) represents the kinetic energy introduced to the occluding element in a full-flow environment (catheter tip close to, but not pressed against the occlusion). The dynamic pressure of the system

was determined by simplifying Bernoulli's Principle to $q = ½ * pv^2$ where q is the dynamic pressure, p is the fluid density, and v is the fluid velocity at the catheter tip. Dynamic pressure, velocity, and flow results were recorded and graphed in Sigma Plot with 2x standard deviation bars.

Static Pressure Analysis

The static pressure of each device was measured directly with an Equus 3620 Innova Vacuum Gauge (Equus Products, Irvine, CA). Both the Penumbra System and each syringe were individually attached to the pressure gauge and, after maximal aspiration, the peak pressure and the test duration was recorded. The Penumbra System was later modified to allow it to pump down before testing the pressure development characteristics. This was accomplished by placing a closed valve in between the Penumbra Pump and the vacuum gauge, only opening it after the system had been turned on for over 2.5 minutes.

Force Analysis Between Catheters

The force applied to the occlusion at the catheter tip is applicable in static, or no-flow scenarios. This was determined by multiplying the maximum static pressure of each aspiration source by the area of the catheter exposed to the occlusion. The units for force were recorded in Newtons.

Statistics

All statistical analysis was performed in Sigma Plot based on a one-way analysis of variance, Holm-Sidak pair-wise multiple comparison procedure (alpha = .05). To emphasize statistical variance error bars are displayed as 2x standard deviation.

Results

Dynamic Pressure

For all test catheters, flow testing revealed that all syringes provided significantly higher mean dynamic pressures at the tip of the catheter compared to the canister (Figure 1). The mean dynamic pressures achieved in this study were: 041+syringe (0.52 inHg) vs. 041+canister (0.14 inHg) [$p < .001$], 4Max+syringe (1.54 inHg) vs. 4Max+canister (1.09 inHg) [$p < .001$], 054+syringe (1.48 inHg) vs. 054+canister (0.43 inHg) [$p < .001$], 5Max+syringe (1.32 inHg) vs. 5Max+canister (0.49 inHg) [$p < .001$], and SS+syringe (1.16 inHg) vs. SS+canister (0.10) [$p < .001$] (Table 1). When using the shuttle sheath, the 20 mL Medallion syringe provided a significantly higher dynamic pressure (1.3425 inHg) compared to all of the BD syringes (max 1.1027 inHg) [$p < .001$].

Catheter	**041**	**4Max**	**054**	**5Max**	**SS**
Mean Dynamic Pressure With Syringes (inHg)	0.52 (SD 0.05046)	1.54 (SD 0.10991)	1.48 (SD 0.05202)	1.32 (SD 0.14376)	1.16 (SD 0.10617)
Mean Dynamic Pressure With Suction Canister	0.14 (SD	1.09 (SD	0.43 (SD	0.49 (SD	0.10 (SD

(inHg)	0.00421)	0.01638)	0.02429)	0.01000)	0.00456)
P-Value	< .001	<.001	< .001	<.001	< .001

Table 1: Mean dynamic pressure comparison of aspiration sources.

Flow Rate

Flow rate results confirmed that larger catheters produced higher flow rates given the same aspiration source (Figure 2). As an example, aspirating with a 60mL BD syringe produced average flow rates of 1.71 mL/s (041), 2.89 mL/s (4Max), 4.58 mL/s (054), 4.67 mL/s (5Max), and 12.36 mL/s (SS). With exception to the 054 catheter compared to the 5Max catheter, different catheter combinations produced significantly different flow rates, including comparing the 041 catheter to the newer 4Max catheter ($p < .001$). In general, as the catheter outlet increased in diameter, the flow rate significantly increased ($p < .001$).

Static Pressure

All static pressures are displayed in Figure 3. The maximum static pressures of the syringes ranged from 1.5 in Hg, for 1mL BD syringes, to 23 in Hg, for 60mL BD syringes, and were achieved nearly immediately. The Penumbra System developed a maximum static pressure of 24.5 in Hg after 125 seconds of aspiration. When allowed to pump down for 2.5 minutes, the

Penumbra System developed a maximum static pressure of 24.75 inHg nearly immediately. All max static pressures are significantly different from each other ($p < .001$).

Force Analysis Between Catheters

The force analysis between catheters is described using the 60mL BD syringe as this was the syringe possessing the highest maximum static pressure, though the comparison is valid for all aspiration sources as it is dependent only on catheter outlet areas. With the 60mL BD syringe, forces attained in static scenarios are as follows: 60mL BD + 041/4Max catheter (0.066N), 60mL BD + 054/5Max catheter (0.115N), and 60mL BD + SS (0.352N) (Figure 4). All forces in Figure 4 are significantly different ($p < .001$).

Case Reports

A patient presented acute onset left-sided weakness three hours after symptom onset. A non-contrasted head CT revealed a hyperdense MCA sign on the right. A CT angiogram revealed an abrupt truncation of the right MCA. A CT perfusion suggested a likely infarction in the basal ganglia and likely penumbra, defined as low flow, high volume, prolonged time to drain, in the surrounding tissue (Figure 5).

The patient was taken for cerebral angiography which revealed that the occlusion had progressed to the internal carotid artery (TIMI 0.) Taking into consideration the results described above, a shuttle sheath was placed at the proximal border of the occlusion and Forced-Suction

Thrombectomy was performed using a 20 cc Medallion syringe. This opened the artery to the petrous internal carotid artery. Next, a 054 Penumbra reperfusion catheter was placed at the proximal border of the occlusion and a Forced-Suction Thrombectomy was performed with the same syringe. This cleared the clot up to the M1, so the 054 was advanced into the M1 and a final suction thrombectomy was performed, completely clearing the clot (TIMI 3.) Total time of the procedure from access to closure was 30 minutes and total time from first aspiration to last was 9 minutes.

The patient awoke from surgery with a hemiparesis. MRI revealed an isolated right basal ganglia stroke. At 9 month follow-up, the patient could ambulate without assistance but experienced persistent left upper extremity weakness.

Another patient presented with a Hunt-Hess grade 4, Fisher grade 4 subarachnoid hemorrhage from a ruptured anterior communicating artery aneurysm. During coil embolization of the aneurysm via the right internal carotid artery the right middle cerebral artery became occluded. A penumbra 054 reperfusion catheter was advanced to the proximal border of the clot and a Forced-Suction Thrombectomy was first attempted with a 30 cc BD syringe and then, when this was unsuccessful, a 60 cc BD syringe which was also unsuccessful. The 054 was then attached to the Penumbra System (with a separator wire) and the clot was successfully removed (Figure 6). Follow-up imaging revealed a small stroke in the MCA territory. At the six month follow-up, the patient was able to ambulate and look after their own affairs with minimal help.

Discussion

Dynamic Conditions (Full-Flow)

The differences in dynamic pressure between the test groups can be explained by analyzing the limitation to flow in each system. The 041 catheter has a distal cross-sectional area that is 34.2% as large as the inlet cross-section of BD syringes and 19.8% as large as the inlet cross-section of Medallion syringes. In the 041 system the limitation to flow is the relatively small cross-sectional area of the catheter tip compared to the syringe inlet (i.e. fluid velocity saturation - max fluid velocity is observed at the catheter tip).

In contrast to the 041 catheter the shuttle sheath has a distal cross-sectional area that is 181.8% as large as the inlet cross-section of BD syringes and 105.2% as large as the inlet cross-section of Medallion syringes. Because, especially compared to BD syringes, the distal catheter cross-sectional area is larger than the syringe inlet, it is no longer the location of flow velocity saturation and therefore not a major limitation to flow. The major limitation to flow when using the shuttle sheath is the syringe inlet cross-sectional area and is obvious when comparing BD syringes to Medallion syringes when aspirating with the shuttle sheath. Aspirating through a shuttle sheath with a Medallion syringe yields a higher dynamic pressure because the flow-limiting factor is now the syringe inlet diameter, which in Medallion syringes (ID = 2.34 mm) is larger than in BD syringes (ID = 1.78 mm).

The 054 syringe lies somewhere in between the 041 and the shuttle sheath in terms of limitations to flow. In the 054 the distal catheter cross-sectional area is 59.4% as large as the inlet cross-section of BD syringes and 34.4% as large as the inlet cross-section of Medallion syringes. While this syringe-catheter combination produces the highest dynamic pressures recorded in this study, there is still a noticeable, if not statistical, difference between the BD and Medallion syringes suggesting that the syringe inlet is becoming more of a factor in flow limitation.

The newer 4Max and 5Max catheters represent a completely different catheter design. They possess identical outlet diameters as the 041 and 054 catheters, respectively, however, that diameter is only maintained at the tips of the catheter (the last 10cm for 4Max and 20cm for 5Max) where the remainder of the catheters both increase in diameter to 0.064 in. This increase in bulk catheter diameter reduces the fluid resistance of the catheter as a whole and allows for greater flow through the catheter, thus increasing both the velocity and dynamic pressure at the catheter tip. While both the 4Max and 5Max catheters provided higher flow rates and dynamic pressures when compared to the 041 (for the 4Max) and 054 (for the 5Max) catheters, only the difference between the 4Max and 041 catheters was found to be significant. This is noticeable when viewing the relative increases in flow rate (Figure 2) and dynamic pressure (Figure 1) which are much more prominent in the 4Max catheter. These advantages are seen only in full-flow scenarios.

It is noted that, generally, the dynamic pressure increases slightly as the syringe volume increases, however, this is not likely a true increase in the maximum achievable dynamic

pressure in the system. Realistically, in each test the pressure ramps upward and plateaus when the flow limitations of the system are reached and, toward the end of the test, as the syringe body fills with water, the pressure ramps down. Because the aspiration pressure is applied both maximally and instantly in all experiments, the ramps up to the plateau and down from the plateau should be similar for the different syringes, however, the relative ramp time compared to the plateau time diminishes as the syringe volume increase (i.e. larger syringes spend a larger percentage of aspiration time at the plateau as compared to smaller syringes). The diminishing relative ramp time as syringe volume increases manifests itself as increased mean dynamic pressure, despite the maximal pressure (the plateau) likely remaining at the same level. With this in mind, the main advantage of larger syringes is their ability to apply maximum dynamic pressure for longer periods of time in full-flow scenarios, simply because their volume is not diminished as quickly as smaller syringes.

In the interest of removing occlusions from vasculature the logical assumption is to choose an aspiration source and catheter combination that provides both maximum dynamic and static pressure so as to introduce as much aspiration force as possible to the occluding element to facilitate its removal. The ideal syringe is not obvious until determining the physiological parameters of the vasculature of interest. In the case of extremely small vasculature where only an 041 catheter can be used, any syringe will offer similar dynamic pressure. In situations where the 054 catheter is feasible, using Medallion syringes seem to offer a slight dynamic pressure advantage over the BD syringes (though no statistical difference was determined). In the case where a shuttle sheath is used, Medallion syringes offer a significant advantage in dynamic

pressure compared to BD syringes and their use would introduce the largest aspiration force to the occluding element.

Our data suggests that, in full-flow conditions, maximizing dynamic pressure and the length of time that maximum dynamic pressure is applied is best achieved by aspirating with a syringe possessing both the largest volume and the largest inlet diameter available. Maximizing flow rate is achieved by aspirating with the largest catheter possible and preferentially using the newer 4Max and 5Max in lieu of the 041 and 054 catheters, respectively.

Static Conditions (No-Flow)

Static pressure data is applicable only in no-flow situations and represents the force applied in the worst-case scenario during an aspiration thrombectomy procedure (e.g. the catheter is engaged directly with the occlusion and no flow occurs after maximal aspiration). Devices capable of producing higher static pressure have the ability to exert more force on an occlusive element. In context, this means that a 60mL BD syringe, capable of producing 23 inHg static pressure, might be more successful at removing occlusions compared to a 10mL BD syringe, which produces only 11.5 inHg static pressure. The data confirmed that larger syringes are capable of producing higher static pressures compared to smaller syringes (back to the original argument; larger syringes have more "suction power"), however, no syringe tested matched the static pressure produced with the Penumbra System. Additionally, larger catheters will apply more force to the occlusion simply through an increase in the area in which pressure is applied,

so using the largest catheter possible increases the aspiration force applied to the occlusion which should facilitate its removal (Figure 4).

It's also important to consider not only the maximum attainable static pressure of a device, but also the dynamics of how that pressure develops (Figure 3). The syringes, while they achieve lower static pressures, reach their maximum values almost immediately (less than 0.5 seconds) whereas the Penumbra System (as used clinically, that is, no pump down) took 125 seconds to reach its maximum static pressure. The dynamics of loading in these two situations are completely different, with the syringes approximating a step-jump in force and the Penumbra System producing a plateauing exponential ramp in force. Modifying the Penumbra System with the addition of a valve so that it could pump down produced a pressure curve with nearly instantaneous loading characteristics, virtually identical to syringes. With regards to no-flow scenarios, using the largest syringe available will provide the highest static pressure and using the largest catheter possible will provide the largest aspiration force onto the occlusion.

Case Studies

The experiments and analyses above describe the mechanical characteristics of the aspiration techniques and how to maximize the effectiveness of Forced-Suction Thrombectomy. The cases presented demonstrate the benefits of employing Forced-Suction Thrombectomy as the initial treatment method for ischemic stroke. Case 1 demonstrates that, when successful, Forced-Suction Thrombectomy quickly recanalizes occluded vasculature. Case 2 illustrates a scenario where Forced-Suction Thrombectomy is unsuccessful and demonstrates that transitioning to

alternative treatment methods can quickly and easily be done. In this case, the 054 reperfusion catheter was perfectly placed to begin a traditional Penumbra System thrombectomy with a separator wire and the suction canister. It is also possible to perform a stent-retrieval through the 054 reperfusion catheter using the suction canister in place of a balloon guide catheter for flow arrest. A Forced-Suction Thrombectomy can be performed unsuccessfully but not delay the transition to another therapy for any longer than it takes to aspirate with a large syringe and perform a follow-up run.[7] In this way, Forced-Suction Thrombectomy does not compete with the latest generation of stent-retrievers, but complements them.

It might be reasonably asked if Case 2 demonstrates that the traditional Penumbra set-up is the superior system because it removed the clot and Forced-Suction Thrombectomy did not. On the contrary, we believe that the rationale for utilizing Forced-Suction Thrombectomy is that the length of the procedure is only as long as access and the time needed to aspirate on a syringe, which is especially attractive given the fact that time is a key component in the treatment of acute stroke.# Case 2 demonstrates that if Forced-Suction Thrombectomy is unsuccessful, transition to a slower method does not require removal and replacement of guiding or micro-catheters and requires only the amount of time necessary to thread a separator wire or stent-retriever through the Forced-Suction Thrombectomy catheter already immediately adjacent to the lesion.[8]

The issue of patient safety is unaddressed by the presented experiments and analysis. While the published series as well as our own experience have yet to yield a complication from aspiration,

this by no means is proof that it is impossible. One could imagine that a powerful enough aspiration against a vessel wall could cause endothelial damage. That being said, the literature would seem to support the idea that the pressures generated by the range of syringes available today is safe. Furthermore, the surgeon must be vigilant to ensure that the catheter is engaged with the thrombus. If a thrombus is at a vessel bifurcation, for example, the M1-M2 junction, and it is difficult to determine if the catheter has engaged the thrombus or the endothelium, it would be prudent to choose another thrombectomy method.

Conclusion

This biomechanical examination suggests that, when aspirating through the 041, 4Max, 054, or 5Max reperfusion catheters, Forced-Suction Thrombectomy is best performed with the largest available BD or Medallion syringe. When aspirating through a shuttle sheath, it is best performed with the largest available Medallion syringe. In general, maximizing the static pressure, dynamic pressure, and flow developed in FST is achieved by aspirating with a syringe possessing both the largest volume and the largest inlet diameter available. Maximizing the force applied to the occlusion is achieved by aspirating through the largest catheter possible.

References

1. Kang, D.H., Hwang, Y.H., Kim, Y.S., Park, J., Kwon, O., & Jung, C. Direct thrombus retrieval using the reperfusion catheter of the penumbra system: Forced-Suction thrombectomy in acute ischemic stroke. *American Journal of Neuroradiology*. 2011; 32 (2):283-287.

2. Kang, D.H. Rescue forced-suction thrombectomy using the reperfusion catheter of the penumbra system for thromboembolism during coil embolization of ruptured cerebral aneurysms. *Neurosurgery.* 2012; 70:89-94.

3. Kreusch AS, Psychogios M, Knauth M. Techniques and Results—Penumbra Aspiration Catheter. *Techniques in Vascular and Interventional Radiology*. 2012;15:53-59.

4. The Penumbra Pivotal Stroke Trial Investigators. *The Penumbra Pivotal Stroke Trial.* Stroke 2009 August 01;40(8):2761-2768.

5. Baskurt OK. *Handbook of Hemorheology and Hemodynamics.* Vol 69. 1st ed. Amsterdam: IOS Press; 2007:21-72.

6. Bodnár T, Sequeira A, Prosi M. On the shear-thinning and viscoelastic effects of blood flow under various flow rates. *Applied Mathematics and Computation*. 2011;217:5055-5067.

7. Hwang YH, Kang DH, Kim YW, Kim YS, Park SP, Suh CK. Outcome of forced-suction thrombectomy in acute intracranial internal carotid occlusion. Journal of NeuroInterventional Surgery. 2012 Apr;Available from:http://dx.doi.org/10.1136/neurintsurg-2012-010277.

8. Goyal M, Menon BK, Coutts SB, Hill MD, Demchuk AM. Effect of Baseline CT Scan Appearance and Time to Recanalization on Clinical Outcomes in Endovascular Thrombectomy

of Acute Ischemic Strokes. *Stroke*. 2011 Jan;42(1):93–97. Available from: http://dx.doi.org/10.1161/STROKEAHA.110.594481.

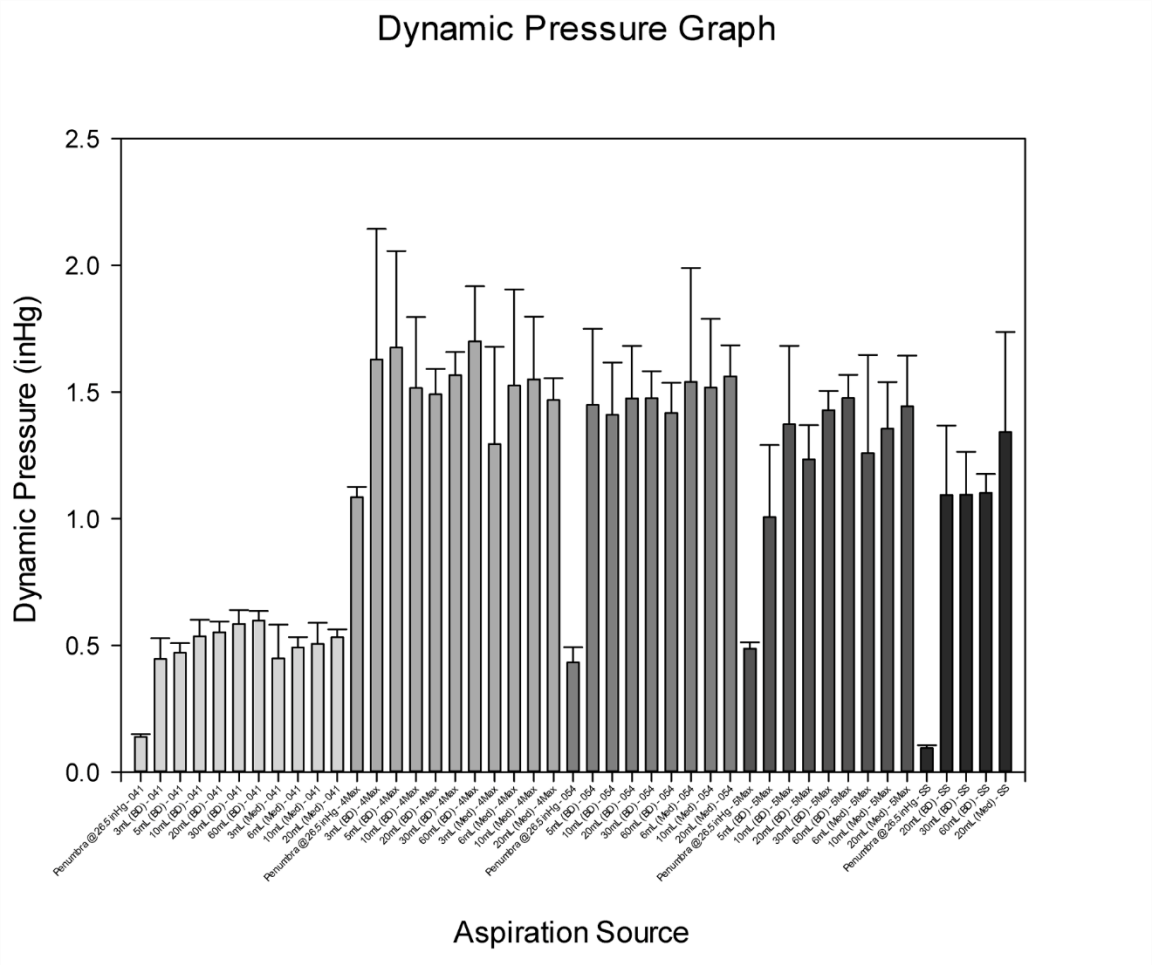

Figure 1.

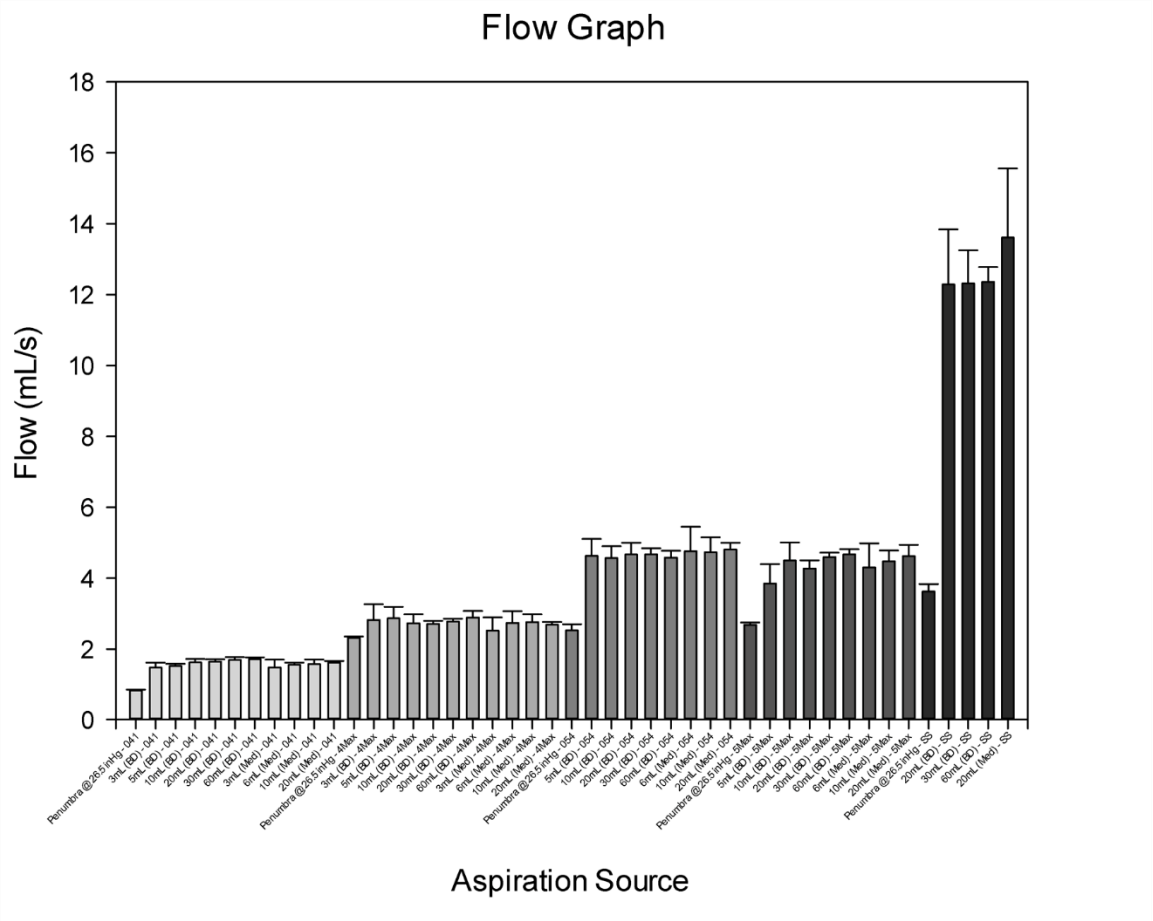

Figure 2.

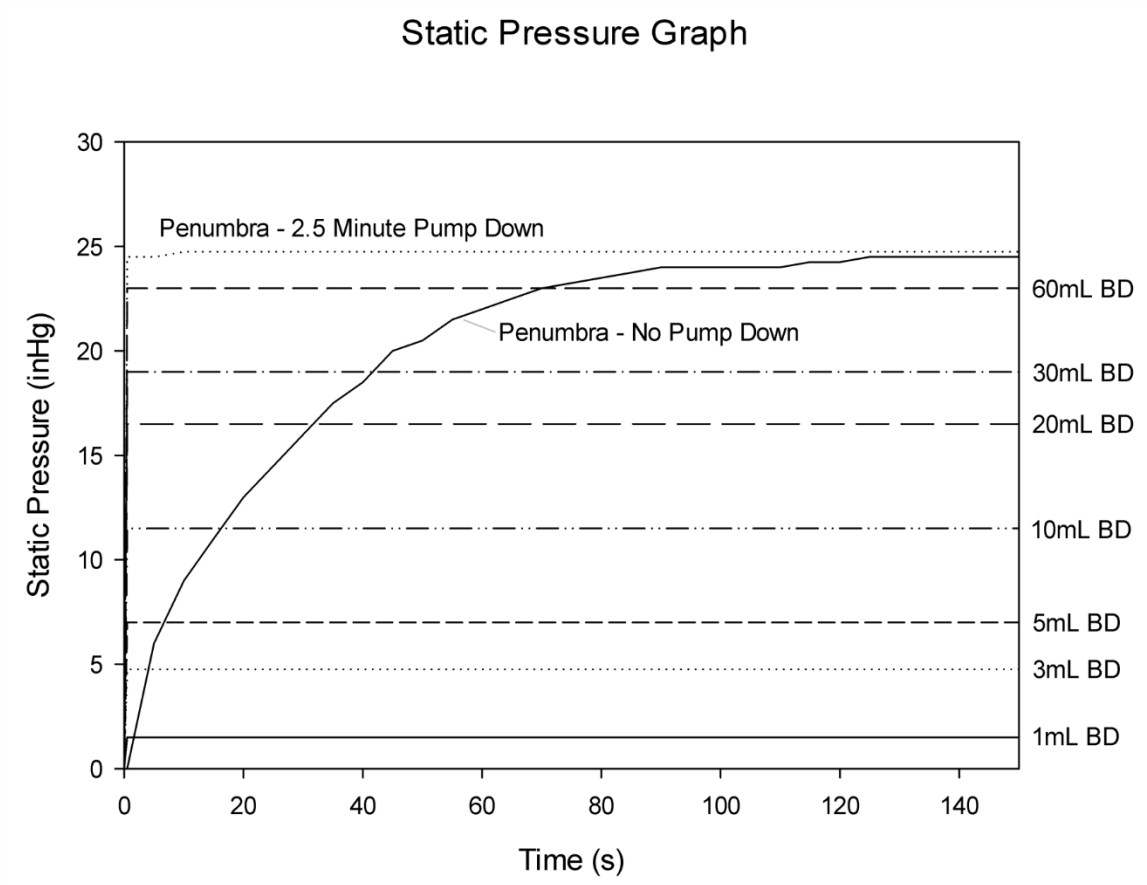

Figure 3.

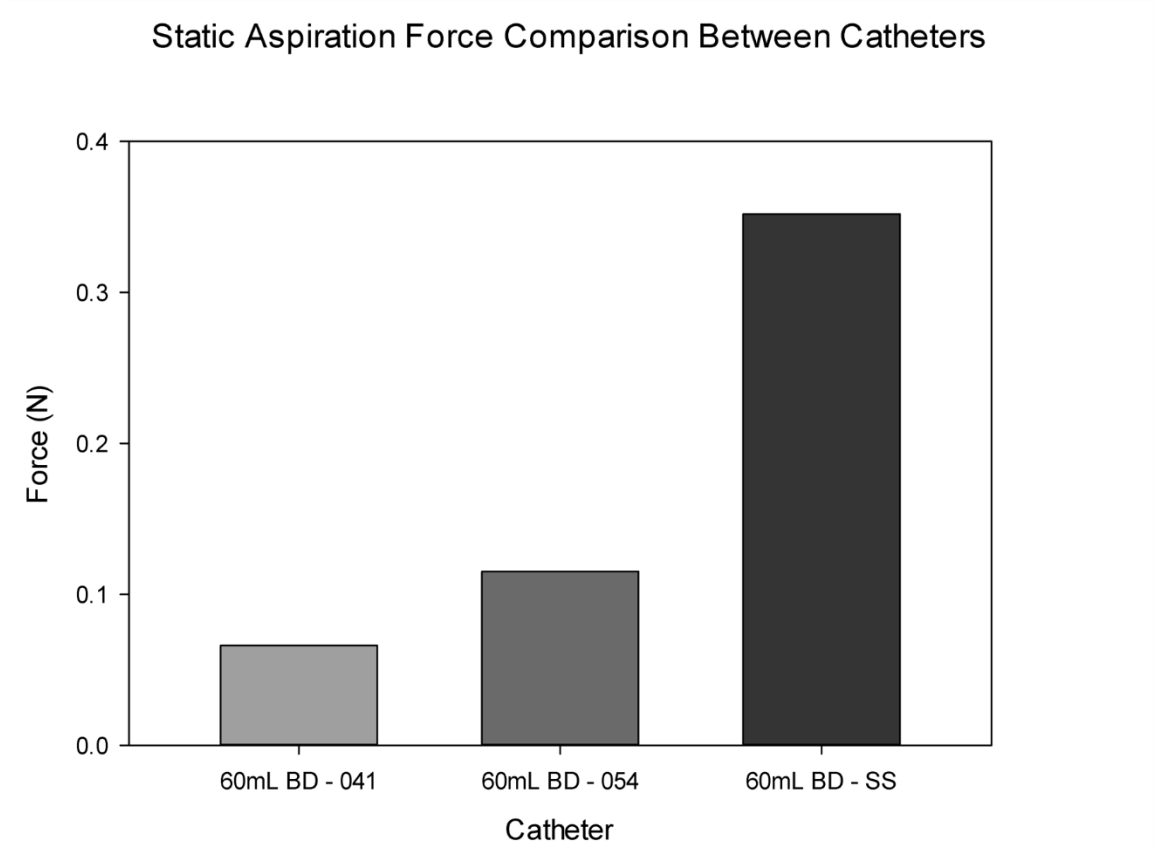

Figure 4.

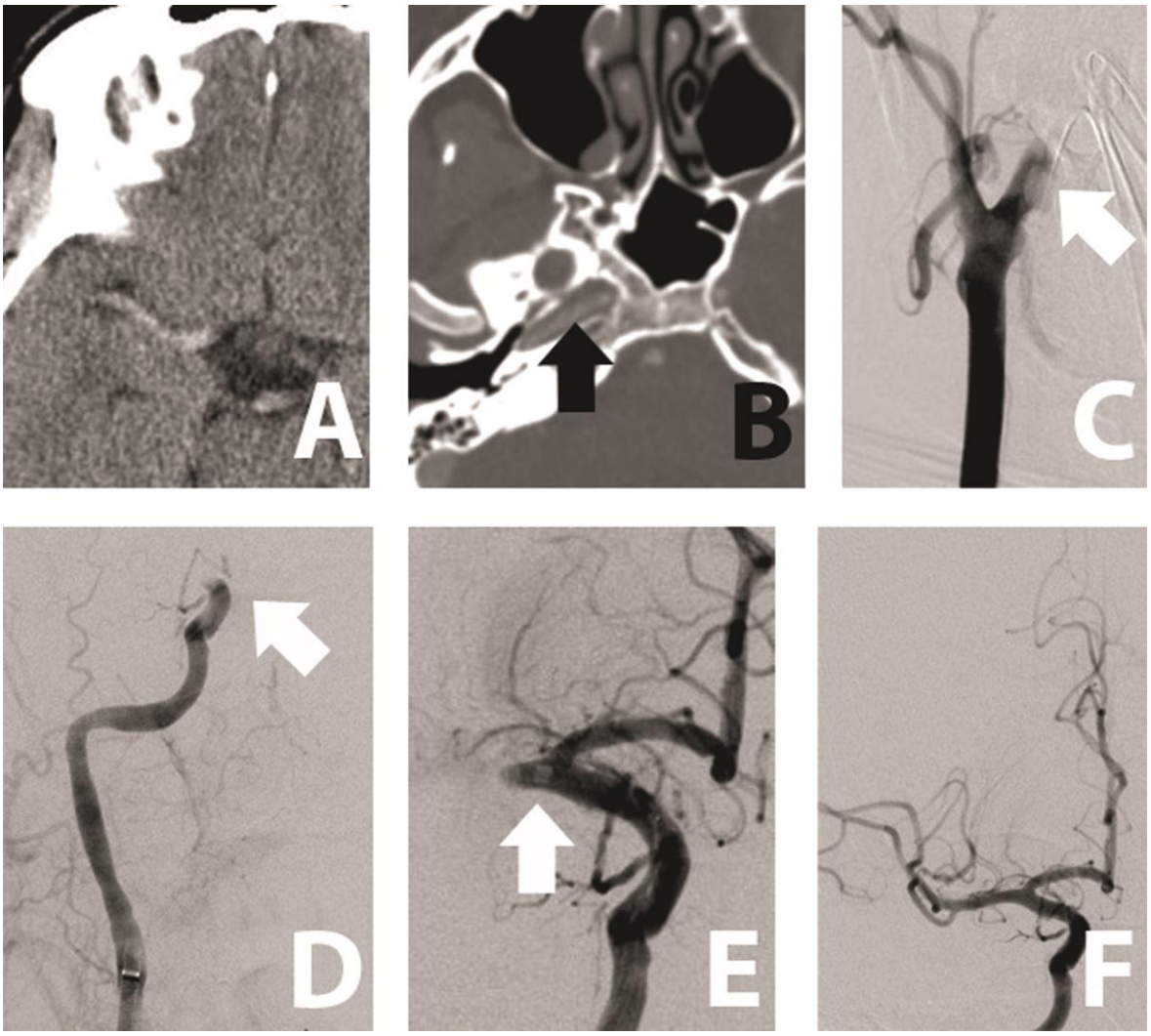

Figure 5.

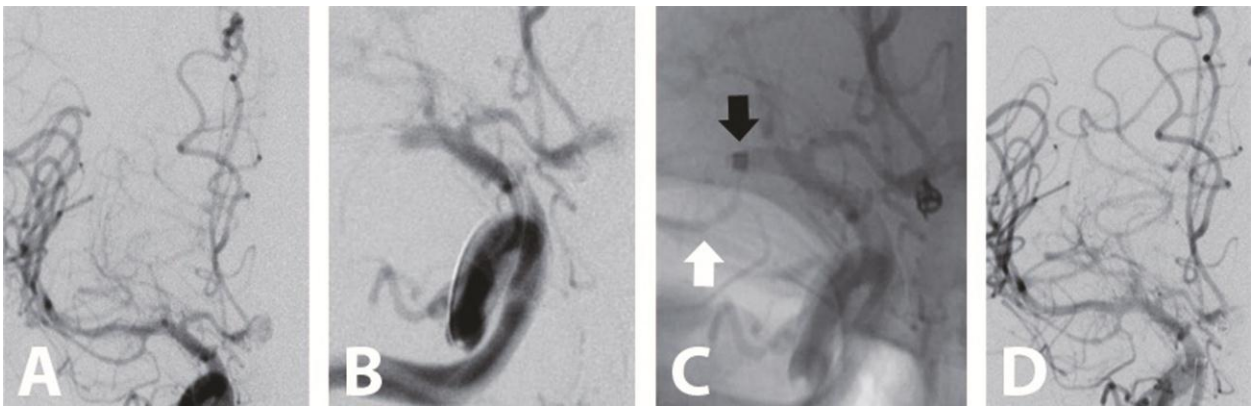

Figure 6.

Figure Legend

Figure 1: Experimental mean dynamic pressure results. Dynamic pressure, which is directly proportional to fluid velocity at the catheter tip, represents the kinetic energy applied to the occlusion in a full-flow scenario. Generally, dynamic pressure increased as the aspirating syringe volume increased.

Figure 2: Experimental flow rate results. Note the 4Max catheter produced significantly higher flows compared to the 041 catheter ($p < .001$) and that flow rate increased as catheter outlet diameter increased.

Figure 3: Dynamics of static pressure development for aspiration sources. All maximum static pressures recorded in Figure 3 were significantly different ($p < .001$). All syringes developed maximum static pressure almost instantly. As used clinically, the Penumbra System required over 2 minutes to develop its maximum static pressure. When given a 2.5 minute pump down, the dynamics of static pressure development for the Penumbra System were nearly identical to that of syringes.

Figure 4: Force comparison between catheters using a 60mL BD syringe as the aspiration source. Because each aspiration source develops a maximum static pressure independent of catheter size,

maximizing the area over which the aspiration pressure is applied maximizes the aspiration force on the occlusion. This is accomplished by aspirating with the largest catheter available.

Figure 5: Patient 1

Caption: A. Non-contrasted CT of head reveals hyperdence middle cerebral artery (MCA). B. CT angiogram in the axial plane. Black arrow: filling of the petrous carotid. C. Digital subtraction angiogram (DSA) of right common carotid artery. White arrow: no filling of right internal carotid artery (ICA). D. DSA of right ICA. White arrow: artery has been recanalized to the clinoidal segment. E. DSA of right ICA. Clot removed up until origin of MCA. White arrow: tip of 054 reperfusion catheter. F. DSA of right ICA after all clot removed.

Figure 6: Patient 2

Caption: A. DSA of right ICA illustrating partially coiled ACOM aneurysm and mild vasospasm. B. Abrupt filling defect of the right MCA consistent with intra-procedural clot. C. Unsubracted angiogram immediately after Forced-Suction Thrombectomy. White arrow: opened anterior temporal branch. Black arrow: Tip of 054 reperfusion catheter. D. Post-thrombectomy performed with 054 and 041 reperfusion catheters as well as separators and suction canister demonstrates recanalized vessel.